**TRANSONIC AEROELASTIC ANALYSIS OF SYSTEMS WITH STRUCTURAL NONLINEARITIES**

by

I Wayan Tjatra

Dissertation submitted to the Faculty of the

Virginia Polytechnic Institute and State University

in partial fulfillment of the requirements for the degree of

Doctor of Philosophy

in

Aerospace and Ocean Engineering

APPROVED:

Dr. Rakesh K. Kapania, Chairman

Dr. B. Grossman

Dr. R. T. Haftka

Dr. R. W. Walters

Dr. E. R. Johnson

April 1991

Blacksburg, Virginia

# TRANSONIC AEROELASTIC ANALYSIS OF SYSTEMS WITH STRUCTURAL NONLINEARITIES

by

I Wayan Tjatra

Dr. Rakesh K. Kapania , Chairman

Aerospace and Ocean Engineering

(ABSTRACT)

Wing structures often contain nonlinearities which affect their aeroelastic behavior and performance characteristics. Aerodynamic flows at transonic Mach numbers generate nonlinear aerodynamic forces on the wing affecting the aeroelastic response of the wing. Analysis techniques accounting for these structural and aerodynamic nonlinearities, and an understanding of their potential influence on the flutter mechanism of two-dimensional and three-dimensional wing-structures model are the main objective of this study.

Two different catagories of structural nonlinearities, i.e. (i) distributed nonlinerity and (ii) concentrated nonlinearity , are considered. The concentrated nonlinearities are mathematically modeled using Asymptotic Expansion method which based on on the Krylov - Bogoliubov - Mitropolski technique. The effective stiffness coefficient of a nonlinear element is defined as the ratio of the amplitude of the Fourier series expansion of the load and the amplitude of the displacement of that element. The effects of distributed nonlinearities on the aeroelastic characteristic of three-dimensional wing model are also investigated. The influences of this type of nonlinearity is treated in a quasi-nonlinear approach , which allows the variation of

the the natural frequencies and damping factor of the structure model with respect to the amplitude of the motion.

The transonic aerodynamic pressure distributions have been obtained by solving the unsteady Transonic Small Disturbance ( TSD ) flow equation using finite-difference techniques. An Alternating Direction Implicit ( ADI ) algorithm was used for two-dimensional flow model, and an Approximate Factorization ( AF ) algorithm was used for three-dimensional flow model. The finite-state generalized aerodynamic forces used in the aeroelastic analysis have been calculated by employing the Method of Harmonic Oscillation and the Pulse Transfer Function analysis.

The solution of the aeroelastic equation in frequency domain is obtained by representing the equation in a finite-state form through the modal approach using Lagrange's equation . The flutter boundary is obtained by solving this equation using the classical U-g method and root locus analysis.

Flutter analysis of a two degree-of-freedom , two-dimensional typical wing sections with nonlinear torsional springs are studied. The aeroelastic responses of the system are obtained by integrating the nonlinear structural terms and aerodynamic terms simultaneously using Newmark - $\beta$ and Wilson - $\theta$ methods. Flutter results obtained from both time integration and eigenvalue solutions are compared. These two results, in general, are in agreement. Flutter behavior of a simple three-dimensional swept wing model is also investigated. Comparison of the flutter boundary obtained by using the eigenvalue solution with flutter data from wind-tunnel experiments are made.

# Acknowledgements

I would like to thank the members of my committee for their support, encouragement and criticism. I especially thank Dr. R. K. Kapania and Dr. B. Grossman for patiently providing guidance and allowing me the freedom to pursue my own postulates and make and correct my own mistakes.

A very special thanks to Ken, Josh and Michael, without whose moral support I would have been unable to finish my engineering study. A special note of thanks to my colleagues, who shared their knowledge, time and humor to aid me.

I dedicate this small work to my dear father, for his friendship and dreams, ***tat tad evavágaccha tvaṃ mama tejoṃśasaṃbhavam*** (surely it reflects a small portion of my glory ) .

# Table of Contents

# List of Illustrations

# Chapter 1

# Introduction

Under certain conditions, parts of an aircraft structure such as the wing or the horizontal tail surface can experience an excessive unstable oscillation. This so-called 'flutter' phenomenon, is an aeroelastic problem which is governed by the mutual interaction of elastic and inertial forces of the structure and the unsteady aerodynamic forces induced by the oscillation of the part of the aircraft structure itself, Refs. 1-4 . As is the case in many other forced vibration phenomena of elastic systems, several vibration modes may be involved ( for instance the first bending and first torsion modes of the wing ). These modes interact with each other under the influence of the oscillating aerodynamic forces. In such a case, the vibrating structure begins to extract energy from the surrounding airstream which leads to a progressive increase in the oscillation amplitude. This generally results in structural damage and failure.

Since aerodynamic forces increase as the free-stream velocity increases, whereas the elastic and inertial forces for a given structure configuration remain almost constant during the oscillation, usually there exists a minimum flight speed above which the flutter phenomenon occurs. The ability to predict this minimum value, termed as 'flutter speed' and the stability boundary of the structure, termed as 'flutter boundary' , are of great importance in aircraft structural design. Conventional design practice required that this flutter boundary of the structure be outside the flight envelope by a margin of at least 15 percent in equivalent airspeed. Therefore, a correct understanding of the flutter ( aeroelastic ) characteristics of the structure is important for safety reasons as well as for the overall performance of the aircraft.

For many years, flutter analysis has been performed based on linearized aerodynamic and structural theories, which assume that both the structure and aerodynamics properties of the system are independent of the amplitude of the structural response, Refs. 5-9 . This assumption allows the use of linear structural and aerodynamic models and the utilization of the superposition principle. In many cases, this linear approximation has been validated by comparison with the experimental data and is found to give results that are sufficiently accurate for some design purposes, as shown in Ref. 9 . For example, in flutter analysis of elastic wing structures in subsonic and supersonic free-stream Mach numbers, the linear lifting-surface theories such as the Doublet-Lattice method, Kernel function methods or Theodorsen theory will give an adequate prediction of the unsteady aerodynamic loads, Refs. 10-12 . The nearly linear behavior of the aerodynamic flows over thin wings at small angles of incidence in subsonic and supersonic flight regime make it possible for the prediction of the unsteady aerodynamic loads by linear theory or theoretical means which are well developed for this flight speed regime.

For transonic flight regimes, however, because of the mixed subsonic-supersonic pattern of the flows, the theoretical means for unsteady aerodynamic load prediction are less developed. The airloads calculation for aeroelastic analysis are mainly based on the expensive numerical solution or the wind-tunnel experiments, Refs. 13-15 . This is unfortunate since experience has shown that transonic flow conditions are the most critical region for aeroelastic analysis . The main reason for this is the rather unique behavior of the unsteady aerodynamic forces at transonic flow regime, especially in the case of transonic flow with strong embedded shocks. This is reflected by an interesting behavior called 'flutter dip' , a region in which the flutter speed gradually drops to a minimum in the transonic speed range followed by a rapid upward rise.

An explanation for this behavior is that the airloads on the oscillating structure change drastically when the flight Mach number increases through the transonic range. The linearized aerodynamic theory could not predict this drastic change. In this transonic flow regime, the physics of the flow must be described by a nonlinear or system of nonlinear equations in which several parameter that are not included in the linearized transonic theory, such as : the wing thickness, wing camber, angle of incidence and the amplitude of the oscillation, have to be taken into account.

Ashley, in Ref. 16 , concluded that the dominant factor in the generation of this peculiar behavior of the aerodynamic load is the involvement of the shock waves which are moving along the wing surface and their interaction with the boundary layer. This shock-wave boundary-layer interaction phenomenon occurs because a very small decrease in the boundary layer displacement, causes a reduced shock pressure rise across the shock and hence an upstream movement of the shock. This

shock-wave movement creates an important phase-lag between the wing oscillation and the aerodynamic response to this oscillation leading to changes in the pressure distribution over the wing surface.

This explanation was supported by the wind-tunnel investigation done by Farmer and Hanson, Ref. 17 , on two swept wing models with identical dynamic properties but different thickness distribution properties ( one being a conventional wing and the other being a supercritical wing ), in which a pronounced transonic dip was observed on both of the wings at the transonic free stream velocities. This experiment also shows that the aeroelastic behavior of wing structures is highly dependent on the wing profile ( shapes and thickness distribution ), with a supercritical wing having a minimum flutter dynamic pressure as much as 30 % below that of the conventional wing. This result is in contrast to the results obtained from the calculation using linearized aerodynamic theories, in which the flutter of both wing models is independent of the thickness distribution. During the experiments, it was shown that this difference can be attributed to shock waves observed on the surface of the conventional wing configuration.

Interest in the transonic flight regime began from the need for a new military aircraft design. It was started with the development of modern high-performance military aircrafts for supersonic operations for which the transonic speed range was the transition phase that has to be passed safely without excessive drag rise and without being aeroelastically unstable. Then came the new generation of the 'air-combat fighter' aircraft, such as F-14, F-15, F-16, and F-17 fighter planes, which have optimal maneuverability under transonic flow conditions. In relation to the commercial aircraft design, the interest arose from the need to find a concept which makes

it possible to cruise at transonic speeds without having the drag penalty induced by the shock wave movements.

Inspired by this renewed interest in transonic flight, a large number of efforts are being made to solve the unsteady transonic flow equations along with its use in the transonic aeroelastic analysis. In the last 15 years , there has been a remarkable improvement in computational transonic aerodynamic capability. This has resulted from the continuing availability of larger, faster computers and from the rapid advances made in the development of numerical methods.

The Navier-Stokes equations are accepted as the governing equation for most of fluid dynamic phenomena of interest. These equations are capable of presenting mathematically the physical phenomena encountered in transonic flows, including mixed subsonic-supersonic pattern, shock waves, boundary layers and separation. They also apply to turbulence, a random, dissipative, three - dimensional phenomenon that involves many characteristic scales. For practical reasons, in the numerical solution of these equations, not all of the resolution of these scales are permitted, and some type of averaging must be used. The most commonly used is the Reynolds time - averaging procedure in which the equations are averaged over a time interval that is long compare with turbulent eddy fluctuations, but small compared with microscopic change in the flow field. This process introduces new terms, called 'Reynold-stresses' , which represent the time-average transport of turbulent momentum and energy.

The Euler equations, that are the exact equation for an inviscid flow , result from neglecting all viscous and heat-conduction terms in the Navier-Stokes equations. The

Euler equations are used when the inviscid effects dominate the viscous effects and the flows are highly rotational, for example flows with strong shock waves.

The full potential equation is obtained from the Euler equation under the assumptions of irrotational, isentropic flow. The main advantage of this assumption is that it allows the introduction of a single velocity potential, $\Phi$ , instead of three velocity components. The governing equation for an unsteady potential flow are usually developed from the mass conservation equation, with the density obtained through the Bernoulli's equation and the velocity potential definition. The full potential equation is a non-linear, second-order partial differential equation in space and time, and similar to the Euler and Navier - Stokes solutions, its numerical solution requires the implementation of the tangency boundary condition on the body surface. Thus , for unsteady flows, the finite-difference solution requires the use of a time dependent, body conforming grid system, which adds to the overall complexity and computational efforts of the problem. Consequently a simpler form of the full potential equation, the transonic small disturbance equation, is often utilized.

The transonic small disturbance equation is derived by assuming that the perturbation of the flow from the free stream values are small and that the free stream Mach number is close to unity. With these assumptions the velocity components of the flow can be expressed in term of a perturbation velocity potential, $\phi$. The resulting governing equation is also a non-linear, second - order partial differential equation in space and time, Ref. 18 . However, consistent with the small disturbance approximation, the surface boundary conditions are applied on the mean body surface, so that a steady grid can be used, even for oscillating surfaces. This formulation is useful for thin wings at small angles of incidence.

By the mid 1970's unsteady transonic flow solutions became available. The computational aerodynamics for unsteady transonic flows can be classified based on the type of equations used and complexity of the configuration considered. These solutions, in general, follow two distinct approaches, Ref. 19 ,

1. Methods in which the nonlinear mean steady flow solution and the imposed linearized unsteady ( consisting of a time-dependent perturbation of small amplitude ) solution are obtained separately. The solution by Ehlers, Ref. 20 , Traci, Albano, and Farr, Ref. 21 , and Cunningham, Ref. 22 , are examples of this kind of approach. These approaches are only valid when the amplitude of the motion is very small and all shock waves are very weak. This engineering-type approach can give solutions for a very limited application in transonic flows.

2. Methods in which the steady and unsteady flow field are treated simultaneously, where nonlinear unsteady flow equations are solved. Finite-difference or finite-volume methods are generally used. Almost all the well known unsteady transonic analyses, such as the pioneering works by Isogai, Ref. 23 , Magnus and Yoshihara, Ref. 24 , Ballhaus and Goorjian, Ref. 25 , and many others, follow this approach.

The second approach needs much more computational resources ( time and storage ) since a large number of parameters, such as : reduced frequency, Mach number, amplitude of the motion, etc. , must be taken into account in the solution. But, it can be applied for more general problems, such as for flows with strong shock waves.

Early research in computational transonic aerodynamic and aeroelastic analysis has been highly focused on the development of finite difference algorithms for the solution of the transonic small disturbance, Refs. 25-32 , and full potential, Refs. 23,33-36 , equations, although some work are already begun for the higher level equations, Refs. 24,37,38 . Pioneering steady transonic flow algorithms were developed by Murman and Cole, Ref. 32 , for the small disturbance equation and by Jameson , Ref. 33 , for full potential equation. In the same period, methods were developed for Euler equation solution with shock fitting by Grossman and Moretti, Ref. 39 , and for Euler solution with captured shock using artificial viscosity method by Magnus and Yoshihara, Ref. 24 .

The computational methods of Ballhaus and Lomax, Ref. 26 , and Ballhaus and Goorjian, Ref. 25 , which made use of the small disturbance flow equation, had an important impact on this field. They incorporated a low - frequency approximation, which, along with the introduction of implicit finite difference methods, enabled economical two-dimensional unsteady transonic flow solutions to be obtained. This approximation is valid for the reduced frequency of the oscillation less than 0.2 which is too restrictive for aeroelastic application ( flutter can be found at reduced frequency as high as 0.5 ) . However, the low - frequency method was considerably more efficient than the Euler equation solutions of Magnus and Yoshihara, and Lerat and Sides, Refs. 24 and 38 , respectively. Along with the numerical development there was an important wind tunnel experimental investigation by Tijdeman, Ref. 40 . This work investigated airfoil behavior including shock wave motion and pressure distribution for a pitching airfoil in transonic flow regimes which gave a better understanding of the effect of shock wave movement in unsteady transonic flows.

Since then, unsteady transonic aerodynamics has undergone a rapid growth. Numerous researchers have studied unsteady transonic flows around airfoils using a number of numerical techniques that are based on inviscid and viscous equations which model the physics of the flows at various levels of complexity. Some investigations also had been conducted on the effects of airfoil thickness, shock-wave boundary-layer interaction, angle of attack, and mode shapes and frequencies of the structure on the transonic load.

At present, some of the most advanced codes used for aeroelastic analysis , such as ATRAN3S ( the NASA Ames version of XTRAN3S - the Airforce/ NASA code for transonic aeroelastic analysis of aircraft ) , Ref. 41 , and CAP-TSD ( code developed at NASA Langley ) , Ref. 42 , use the transonic small disturbance equation. Both of these codes, currently, are being used for generic research in unsteady transonic aerodynamic and aeroelasticity of almost complete aircraft configurations. The XTRAN3S code is based on the Alternating Direction Implicit ( ADI ) algorithm, whereas the CAP-TSD code uses the Approximate Factorization ( AF ) algorithm. Several terms of the ADI algorithm are treated explicitly in XTRAN3S, which leads to a time step restriction based on numerical stability considerations. Meanwhile the AF formulation in CAP-TSD code has no term that has to be treated explicitly. It was pointed out in Ref. 42 that the unsteady and steady results using these two algorithms were nearly identical, but the AF algorithm significantly decreases the computational time and cost.

One of the first numerical solutions of the full potential equation in unsteady transonic flow was done by Isogai, Ref. 23 , which solved the equation in a stretched cartesian coordinate system using a time marching semi-implicit finite difference

scheme. This scheme is similar to that being used by Ballhaus and Lomax, Ref. 26 , for low frequency small disturbance flow equation. From the comparison of the numerical results with the experimental results obtained by Tijdeman, it was concluded that the use of the full potential or transonic small disturbance equation must be restricted to the cases in which the embedded shock is weak. When the shock become strong, the entropy production through the shock can not be neglected. Some advances in potential flow solutions can be found in the work of Sankar, et.al., Ref. 43 , Whitlow, et. al., Ref. 44 , and Shankar, Ref. 45 . The solution algorithm presented by Sankar, et.al., used a strongly implicit procedure ( proposed by Stone, Ref. 46 , and referred as SIP ) that may be applied either as a relaxation procedure for steady flow problems, or as an accurate non-iterative time-marching procedure for unsteady flows. In Whitlow's solution, the nonisentropic effects caused by shock waves are included in order to avoid the multiple flow solutions, Ref. 47 . They showed that by modifying the isentropic density to include the effects of entropy jumps across the shocks, potential solutions closer to Euler solutions are obtained. Shankar imposed an internal Newton iteration at each time level of the approximate factorization procedure to achieve time accuracy and computational afficiency. A similar approximate factorization, later on , was used by Batina, Ref. 42 , in developing CAP-TSD code. It is still too expensive to use code based on full potential flow equations for generic calculations of complete aircraft configurations.

A code based on the Euler/Navier-Stokes equation, called ENSAERO, has also been developed and applied for aeroalastic analysis of a wing configuration, Ref. 48 . ENSAERO is a general-purpose aeroelastic code based on Euler/Navier-Stokes equations and the modal equation of motion with time accurate aeroelastic configuration adaptive grids that was developed at NASA Ames. Batina, Ref. 49 , at NASA

Langley has also developed an Euler equation based code for aeroelastic analysis of aircrafts using unstructured grid.

As mentioned earlier, viscous effects have a significant role in transonic flows. The presence of the shocks and their interaction with boundary layer makes the flow structure more complex and changes the pressure distribution over the body. Rizzetta, Ref. 50 , employed two methods to include these viscous effects into the flow calculation that are based on the inviscid flow equation, these are : a viscous ramp method and a lag entrainment method. This viscous corrections are implemented by modifying the inviscid surface tangency condition as well as the downstream wake condition.

The assumption of structural linearity, as previously mentioned, is frequently made in aeroelastic analysis. However, aircraft structures often exhibit nonlinear behavior that affects not only the flutter speed but also the characteristic of the flutter motion, Refs. 51-60 . With the assumption of linear theory, for almost every structural configuration, the flutter dynamic pressure and flutter speed values, above which the structure is unstable and motion grows exponentially with time, can always be defined. As the amplitude of oscillation begins to grow, however, the extent to which this increase continues, depends upon the nature of the stiffness characteristic of the structure. If the structure exhibits nonlinear properties, where the stiffness coefficients change with amplitude of the motion, the oscillation may increase to some amplitude where the structure may experience a stable limit-cycle oscillation.

The study on the structural nonlinearity effects on the aeroelastic characteristic of a system goes back to the mid-fifties. Woolston, Ref. 51 , made an analog computer calculation for a two degree-of-freedom model and a three degree-of-freedom

model of wing structure having a concentrated nonlinearity and made a comparison with a wind-tunnel investigation. It was found that the existence of a preload on the nonlinear system has a very marked effect on the flutter speed, and the flutter speed could be a function of the amount of control surface deflection. It was also found that the flutter speed was reduced by a factor of two when freeplay was introduced into the system. Then Shen, Refs. 52,53 , introduced the concept of 'equivalent linear system' to approximate the actual nonlinear system by applying the simplified version of the method of Kryloff and Bogoliubov ( known as the method of harmonic balance ). The basic idea of this method is based on the assumption that a nonlinear element can be approximately replaced by a linear element with equivalent internal energy when the element is activated at equivalent amplitude level. With this assumption, the stiffness coefficient of the nonlinear element is replaced by its effective value. Application of the method to a two degree-of-freedom airfoil system with control surface was studied.

A similar method was used by Laurenson, Ref. 55 , in the investigation of missile control surface structure containing structural freeplay type nonlinearities exposed to subsonic flow. Definition of the loads acting on the control surface used a linearized aerodynamic representation in which it was assumed that the lift force is proportional to and in phase with the torsional or pitch, motion. The method was expanded by Breitbach, Ref. 57 , for a structural system with multiple sets of strongly interacting, concentrated nonlinearities such as in the rudder and aileron control system. Recently, Kousen and Bendiksen, Ref. 59 , investigated the nonlinear aeroelastic behavior of a two degree-of-freedom typical section airfoil having a torsional freeplay nonlinearity using an unsteady Euler equation solver.

In an attempt to improve the understanding of the nature of nonlinear transonic aerodynamic loads and of structural nonlinearities, an investigation is performed to study the aeroelastic characteristics of wing structures using both typical section model and three-dimensional wing models and considering both aerodynamic and structural nonlinearities. For the transonic aerodynamic calculations, the analysis is limited to attached flows over thin wings at small incidence angles resulting in weak shock waves and negligible boundary layer interactions. Under such circumtances the Transonic Small Disturbance ( TSD ) equation is indeed adequate to represent the physics of the flows. The transonic calculations are also limited for the flows with free stream Mach number less than one.

Two types of structural nonlinearities, i.e. the concentrated one and another one which is distributed over the structure, are considered. The concentrated nonlinearities are treated using a mathematical model of the equivalent stiffness of the elements, while the distributed nonlinear effects are taken into account in a quasi-nonlinear fashion by allowing the natural frequencies and the damping coefficients of the wing to vary with respect to the amplitude level. These variations were obtained from the experiments.

An outline of the contents of this thesis is next presented. Chapter 2 starts with a general derivation of the aeroelastic equation of motion for a two degree of freedom typical section model , which is followed by the transformation of the equation into a matrix form that is suitable for eigenvalue solutions in frequency domain. The three-dimensional wing structure is approximated using finite-state modeling. The aeroelastic equations of motion of the system are formulated through a modal approach using Lagrange's equation of motion. Because the finite-state unsteady

aerodynamic loads model has complex values, for the purpose of compatibility with the structure model, the equation of motion will be expressed in term of real matrices by applying Laplace transforms. The inclusion of the nonlinear spring attachment at the wing root will also be described.

Chapter 3 describes the transonic small-disturbance equation that is being used to calculate the unsteady aerodynamic loads. It will also be shown that several alternatives exist in defining the coefficients in the governing equation. Two different time-integration algorithms to solve the flow equation are discussed. The first one is the Alternating Direction Implicit ( ADI ) algorithm. This algorithm was used for the two-dimensional flow solution. The second method is the Approximate Factorization ( AF ) algorithm which was used for the three-dimensional problems. The assessment of the accuracy, efficiency and limitations of these two finite difference schemes will be presented through a comparison of the results for several test cases with the experimental results and/or the results from other computations. A brief review of the models that have been developed and commonly used to roughly approximate viscous effects in the inviscid flow solver are described with the emphasis being given to two models : (i) lag - entrainment model and (ii) viscous ramp model. This is followed by the description of the method used to calculate the generalized aerodynamic forces for use in the aeroelastic solutions, i.e. the harmonic oscillation method and pulse transfer function method. It will be shown that the pulse transfer function approach is more efficient as compared to the harmonic oscillation approach.

The derivation of the mathematical model of the structural spring nonlinearities are presented in Chapter 4. Two different categories of structural nonlinearities are

considered, i.e., (i) concentrated and (ii) distributed. Also two types of concentrated nonlinearities model are used in this investigation which are closely related to the nonlinearities that exist in some real structures. A survey of the kind of nonlinearities that exist in the aircraft structures is illustrated at the beginning of Chapter 4.

In Chapter 5, the solution of the aeroelastic equation of motion will be explained. For two-dimensional problems both time integration method and eigenvalue type of solution techniques are used, whereas the three-dimensional problems are solved only using an eigenvalue type of solution. Whenever possible, numerical results are compared with the results obtained from the wind-tunnel experiments.

Finally, Chapter 6 summarizes the results from previous chapters and draws some conclusions from this investigation. Recommendations for possible future work related to this study are also be given in Chapter 6.

# Chapter 2

# Aeroelastic Equations of Motion

In this chapter, the derivation of the aeroelastic equations of motion to be used for flutter analysis of wing structure in transonic flow will be covered. This chapter starts with the derivation of the aeroelastic equations using a two-dimensional typical section wing model, followed by finite-state approximation for three-dimensional wing model. Several assumptions that are being used in the derivation of the equation will be clearly stated. The effects of including the nonlinear behavior of the structure in the governing equation will be discussed. Details about the derivation of mathematical models for the structure and aerodynamics will be presented in the next two chapters.

## 2.1 Airfoil section

The governing equation for a two-dimensional airfoil follows from a typical wing model, shown in Fig. 2.1.1 . This model was devised by aeroelastic pioneers Theodorsen and Garrick, Ref. 61 , and is still being used by many researchers, seeking a system model suitable for preliminary examination of flutter and other dynamic response problems. Theodorsen suggested that the dynamics of an actual wing structure might be simulated by choosing the properties of the typical section to match those at station 70 - 75 % of the semispan. Experience shows that this is true in the situations where the wing aspect ratio is large, the sweep angle is small and the sectional characteristics vary smoothly across the wing span. Of course, some essential features are lost, such as the effects of three-dimensional flow and the effect of rigid body degrees-of-freedom. Throughout this study we will consider only plunging and pitching motion. The definitions of various variables and sign convention are described in Fig. 2.1.1 .

In the following analysis, it is assumed that the airfoil section is rigid and the amplitude of the oscillation is small. The mean angle of attack is assumed zero in all cases, and there is no coupling in mechanical damping of the plunging and pitching motion.

Let $\alpha$ be the pitching displacement and $h$ the plunging displacement of the airfoil section, in which $h/c$ , with $c$ being the airfoil chord, is assumed to be small. The kinetic energy of the airfoil can be written as

$$T = \frac{1}{2}\int_{chord} (\dot{h} + x\dot{\alpha})^2 \, dm$$
$$= \frac{1}{2} m\dot{h}^2 + S_\alpha \dot{h}\dot{\alpha} + \frac{1}{2} I_\alpha \dot{\alpha}^2 \qquad [2.1.1]$$

where m is the total mass, $S_\alpha$ is the static unbalance of the wing about elastic axis and $I_\alpha$ is the mass moment of inertia of wing about its elastic axis. The dot represents the derivatives with respect to time. If the bending and torsional spring have total stiffnesses $K_h$ and $K_\alpha$, respectively, the strain energy is given as

$$V = \frac{1}{2} K_h h^2 + \frac{1}{2} K_\alpha \alpha^2 \qquad [2.1.2]$$

The damping force is considered as an unconservative force which depends upon the velocities of the motion and is assumed to be derivable from the Rayleigh's dissipation function,

$$F = \frac{1}{2} c_h \dot{h}^2 + \frac{1}{2} c_\alpha \dot{\alpha}^2 \qquad [2.1.3]$$

where $c_h$ and $c_\alpha$ are the damping coefficients of the bending and torsion spring, respectively.

The aerodynamic lifting force, which is distributed along the airfoil surface, may be regarded as an unconservative force which is capable of doing positive or negative work on the oscillating airfoil. By assuming two-dimensional flow characteristics, one obtains for the virtual work

$$\begin{aligned}\delta w &= -c\,\delta h \int_{chord} \Delta p\, dx - c\,\delta\alpha \int_{chord} \Delta p x\, dx \\ &= -L\,\delta h - M_y\,\delta\alpha\end{aligned} \qquad [2.1.4]$$

where L is the total lift ( positive upward ) , $M_y$ is pitching moment ( positive leading-edge-up ), and $\Delta p$ is the lifting force per unit area.

In Chapter 3 , the relationships are discussed between the aerodynamic lift force and moment, and the motion which causes them. Here we consider that for transonic flows, L and $M_y$ are nonlinear function of the displacements $\alpha$ , h and their time derivatives.

When Eqs. [2.1.1], [2.1.2], [2.1.3] and [2.1.4] are gathered together into Lagrange's equation, Ref. 62 ,

$$\frac{d}{dt}\left(\frac{\partial T}{\partial \dot{q}_i}\right) - \frac{\partial T}{\partial q_i} + \frac{\partial V}{\partial q_i} + \frac{\partial F}{\partial \dot{q}_i} = Q_i \qquad [2.1.5]$$

the motion of the airfoil system is found to be governed by

$$m\ddot{h} + S_\alpha \ddot{\alpha} + c_h \dot{h} + K_h h = -L$$

$$S_\alpha \ddot{h} + I_\alpha \ddot{\alpha} + c_\alpha \dot{\alpha} + K_\alpha \alpha = M_y \qquad [2.1.6]$$

Introducing the following variables :

$$\xi = \frac{h}{c} \qquad \bar{t} = kt$$

$$\omega_h = \sqrt{\frac{K_h}{m}} \qquad \omega_\alpha = \sqrt{\frac{K_\alpha}{I_\alpha}}$$

$$x_\alpha = S_\alpha / mc \qquad r_\alpha = \sqrt{2I_\alpha / mc^2}$$

$$\zeta_h = c_h / m \qquad \zeta_\alpha = c_\alpha / m c^2$$

where $k = \omega c / U$ is the reduced frequency, $\omega$ is the frequency of the motion , U is the free-stream velocity and c is the chord length, c = 2b .

The non-dimensional form of Eq. [2.1.6] can be written as

$$\xi'' + x_\alpha \alpha'' + \zeta_h / k \, \xi' + (\omega_h / k)^2 \xi = -L/mck^2$$

$$x_\alpha \xi'' + r_\alpha^2 \alpha'' + \zeta_\alpha / k \, \alpha' + (\omega_\alpha r_\alpha / k)^2 \alpha = M_y / mc^2 k^2$$

where the prime represents the derivative with respect to $kt$ , the non-dimensional time.

The aerodynamic forces L and $M_y$ may be expressed in term of aerodynamic coefficients as

$$L = \bar{q} c C_l$$

$$M_y = \bar{q} c^2 C_m$$

with $\bar{q} = \frac{1}{2} \rho U^2$ is the dynamic pressure , $U$ is the free-stream velocity , $\rho$ is the mass density of the air and $C_l, C_m$ are the aerodynamic lift and moment coefficients, respectively.

Substituting these expressions and rearranging, the final matrix equation of motion of the airfoil is

$$[M]\begin{Bmatrix}\xi''\\ \alpha''\end{Bmatrix} + [C]\begin{Bmatrix}\xi'\\ \alpha'\end{Bmatrix} + \left(\frac{1}{k^2}\right)[K]\begin{Bmatrix}\xi\\ \alpha\end{Bmatrix} = \left(\frac{4}{\pi\mu k^2}\right)\begin{Bmatrix}-C_l\\ 2C_m\end{Bmatrix} \qquad [2.1.7]$$

where $[M]$ , $[C]$ and $[K]$ are the mass, damping and stiffness matrices, respectively, and they are defined as

$$[M] = \begin{bmatrix}1 & x_\alpha\\ x_\alpha & r_\alpha^2\end{bmatrix}, \quad [C] = \left(\frac{1}{k}\right)\begin{bmatrix}\zeta_h & 0\\ 0 & \zeta_\alpha\end{bmatrix}$$

$$[K] = \begin{bmatrix}(\omega_h/\omega_\alpha)^2 & 0\\ 0 & r_\alpha^2\end{bmatrix}$$

in which $\mu$ is the airfoil - air mass ratio, $m/\pi\rho b^2$ .

The quantities $C_l$ and $C_m$ are function of time. Eq. [2.1.7] is in the form suited for time domain solution ( aeroelastic response ) where the structure terms and the aerodynamic terms are integrated simultaneously.

In cases where the transonic flow has a very weak shock strength, the flow will not be highly nonlinear and the load superposition principle may be assumed to be valid. Then it is more efficient to transform Eq. [2.1.7] into a frequency domain form and solve it as an eigenvalue problem.

To perform such a transformation, it is assumed that the oscillation of the airfoil is harmonic with frequency $\omega$ and can be expressed as

$$\xi(t) = \xi_0 e^{i\omega t}$$

$$\alpha(t) = \alpha_0 e^{i\omega t}$$

and using the principle of load superposition, the total lift and moment coefficients at any time t are given by the summation

$$C_l = \xi_0 e^{i\omega t} C_{l\xi} + \alpha_0 e^{i\omega t} C_{l\alpha} + C_{l0}$$

$$C_m = \xi_0 e^{i\omega t} C_{m\xi} + \alpha_0 e^{i\omega t} C_{m\alpha} + C_{m0}$$

where $C_{l\xi}$ and $C_{l\alpha}$ are the lift coefficients due to unit changes in displacement $\xi$ and $\alpha$ , respectively. Similarly, $C_{m\xi}$ and $C_{m\alpha}$ are the moment coefficients due to unit change in displacement $\xi$ and $\alpha$ , respectively. $C_{l0}$ and $C_{m0}$ are, respectively, the steady lifting and moment coefficients .

Substituting all these expression into Eq. [2.1.7], yields the matrix eigenvalue form of the equation :

$$([M] + [C] - [A])\begin{Bmatrix}\xi_0\\ \alpha_0\end{Bmatrix} = \lambda[K]\begin{Bmatrix}\xi_0\\ \alpha_0\end{Bmatrix} \qquad [2.1.8]$$

where $\lambda = -\left(\frac{1}{k}\right)^2$ and

$$[A] = \left(\frac{4}{\pi\mu k^2}\right)\begin{bmatrix} C_{l\xi} & C_{l\alpha} \\ C_{m\xi} & C_{m\alpha} \end{bmatrix}$$

The solutions of both Eqs. [2.1.7] and [2.1.8] will be described in chapter 5.

## 2.2 Three-dimensional wing

In this section we formulate the aeroelastic equation for a three-dimensional wing. Although the mathematical theory of distributed parameter systems has made rapid advances, the solution of dynamic problem of non-uniform structures system are still very complex. It seems more expedient, from a practical point of view, to approximate aeroelastic systems of aircraft structures by finite-state model, Refs. 64,65 . In this approach, the continuous system ( with infinite degree of freedom ) are represented with a model having a finite number of degrees of freedom. For aeroelastic systems it includes both the structural and aerodynamic modeling.

The theory of finite-state modeling of structures for dynamic analysis is widely used. The various methods of weighted residuals, finite-element techniques and variational techniques have all proven extremely useful for analytical modeling purposes.
In Ref. 63 , Flannelly formulated system-identification techniques for approximating structures by finite-state models from experimental data.

Meanwhile, the same progress has been made in the theory of finite-state modeling to approximate unsteady aerodynamic loads on aircraft structures undergoing arbitrary motion. These methods often utilize oscillatory unsteady aerodynamics or transient aerodynamic response to construct approximate solutions for generalized aerodynamic forces. For example, Pade approximants were used in Refs. 5,66 , and a minimum state method was used in Ref. 67 to describe the unsteady aerodynamic loads in the complex s-plane ( Laplace plane ).

The addition of the resulting expression for the unsteady aerodynamic loads to the structural equations of motion produced a state-space matrix equations which is well suited for the aeroelastic analysis. The solution of this type of equation, which is represented by a finite number of the generalized coordinates, are much simpler and easier to obtain rather than the solution of the continuous model.

In this study, the dynamic characteristic of the flexible wing structure is represented using a modal approach. In this approach, the physical deformation of the elastic structure is expressed by a set of generalized coordinates and modal vector of the structure. The contribution of each mode to the total deformation is described by the Lagrange's equation, Eq. [2.1.5]. Furthermore, it is assumed that the deformation of the wing structure can be represented by deflections at a set of discrete points. This assumption facilitates the used of discrete structural data, i.e. the finite state model of the structure, such as the orthogonal modal vector, the generalized modal stiffness matrix and generalized modal mass matrix. All these quantities can be generated from a finite- element analysis of the structure.

It is assumed that the deformed shape of the wing can be represented by a set of discrete displacements at selected points. From the modal analysis, the total deformation of the wing at any time is given by a finite modal series

$$z(x,y,t) = \sum_{i=1}^{n} q_i(t)\, h_i(x,y)$$

where $h_i(x,y)$ is the displacement of structure in the *i-th* mode. The generalized displacement, $q_i$ (t), specifies the amount of the *i-th* mode participating in the total

displacements and $n$ is the number of structural modes used in the analysis. Using this displacement expression, the kinetic energy can be written as

$$T = \frac{1}{2}\int_S \left(\frac{dm(x,y)}{dS}\right)\left[\sum_{i=1}^{n}\dot{q}_i(t)\,h_i(x,y)\right]^2 dS$$

where S is the planform area and dm(x,y)/dS is the area distribution of wing mass. If it is assumed that the non-conservative damping force is proportional to the velocity at the wing motion, then the non-conservative energy due to damping may be presented using Rayleigh's dissipation function as

$$F = \frac{1}{2}\int_S \zeta\left[\sum_{i=1}^{n}\dot{q}_i(t)\,h_i(x,y)\right]^2 dS$$

where $\zeta$ is the damping coefficient.

The generalized aerodynamic forces, $Q_i$ , associated with mode $h_i(x,y)$ , is obtained from the virtual work due to external aerodynamic forces. The virtual work, $\delta W$ , done by the lifting pressure,$\Delta p$, acting over the virtual displacements $h_i(x,y)\delta q_i(t)$ is

$$\delta W = \sum_{i=1}^{n}\{\bar{q}c^2\int_S\left[\frac{\Delta p(x,y,t)}{\bar{q}}\right]h_i(x,y)\,\frac{dS}{c^2}\}\,\delta q_i(t)$$

from which the generalized aerodynamic forces is obtained to be equal to

$$Q_i = \bar{q}c^2\int_S\left[\frac{\Delta p(x,y,t)}{\bar{q}}\right]h_i(x,y)\,\frac{dS}{c^2}$$

Application of Lagrange's equation with all these expressions and use the structure natural vibration modes as the structure modes, $h_i(x,y)$ gives the equation of motion which can be written in matrix form as

$$[M]\{\ddot{q}\} + [C]\{\dot{q}\} + [K]\{q\} = \{Q\} \qquad [2.2.1]$$

where [ M ], [ C ] and [ K ] are the generalized mass, generalized damping and generalized stiffness matrices, respectively, and are defined

$$\begin{aligned}
M_{i,j} &= \int_S (dm/dS)\,[h_i(x,y)]^2\, dS && \text{for } i = j \\
&= 0 && \text{for } i \neq j \\
C_{i,j} &= 2\,\zeta_i\, M_{i,j}\, \omega_{n,i} && \text{for } i = j \\
&= 0 && \text{for } i \neq j \\
K_{i,j} &= \omega_{n,i}^2 M_{i,j} && \text{for } i = j \\
&= 0 && \text{for } i \neq j
\end{aligned}$$

In this equation $\zeta_i$ is the damping coefficient at mode i , and $\omega_{n,i}$ is the wing i-th natural frequency. $\{Q\}$ is the generalized aerodynamic forces vector.

The total lifting pressure, $\Delta p$ (x,y,t) , can be expressed , assuming that the load superposition principle is valid , as the sum of the contribution due to each mode shapes, $q_j(t)$ . Therefore, the finite state representation of the lifting pressure is written as

$$\Delta p(x,y,t) = \sum_{j=1}^{n} \Delta p_j(x,y,k)\, q_j(t)$$

where $\Delta p_j(x,y)$ is the lifting pressure at discrete point (x,y) due to the wing displacement in the *j-th* mode. Using this relation, the generalized aerodynamic forces for mode j can be written

$$Q_j = -\bar{q}c^2 \sum_{j=1}^{n} q_j(t) \left\{ \int_S \frac{\Delta p_j(x,y)}{\bar{q}} h_i(x,y) \frac{dS}{c^2} \right\}$$

The generalized forces, then, are given by

$$\{Q\} = [A]\{q\}$$

$$A_{i,j} = -\bar{q}c^2 \int_s \frac{\Delta p_j(x,y)}{\bar{q}} h_i(x,y) \frac{dS}{c^2} \qquad [2.2.2]$$

where $A_{i,j}$ may be considered to be the generalized force coefficients from the pressure induced by mode j acting through the displacement of mode i.

This aerodynamic force coefficient is a function of reduced frequency , k , and usually has complex values. For the purpose of easier computation, it would be better to represent the equation of motion, Eq. [2.2.1], in terms of real matrices. This is done by taking the Laplace transform of this equation which yields a matrix equation in s-plane as ,

$$\left([M]s^2 + [C]s + (qc^2)[\tilde{A}] + [K]\right)\{q\} = 0 \qquad [2.2.3]$$

in which $[\tilde{A}]$ is the Laplace transform of the aerodynamic force matrix , [ A ] , and s is the Laplace variable, $\sigma + i\omega$ .

The elements of the generalized aerodynamic force matrix, [ A ] , are usually computed at finite number of values of reduced frequency. In order to be able to apply Laplace transformation to this matrix, each element of the matrix should be represented by a continuous function. Such continuous functions can be obtained by making an approximation to each of the element of the matrix. Pade approximation method , was introduced by Baker in Ref. 68, is used for this investigation. In this method, the aerodynamic forces coefficients at finite number of values of reduced frequency are approximated in s-plane by an interpolating function of the form ( see Appendix A ),

$$[\tilde{A}] = [A_0] + [A_1]\bar{s} + [A_2]\bar{s}^2 + \sum_{m=3}^{6} \frac{[A_m]\bar{s}}{(\bar{s} + \beta_{m-2})} \qquad [2.2.4]$$

where $\bar{s}$ = (b/U)s and $\beta_{m-2}$ is the phase-lag parameters. As described in Ref. 68 , the form of above equation permits an approximation of the time delays between the motion of the wing and the aerodynamic response that is inherent in unsteady aerodynamics subject to the following requirements : complex conjugate symmetry, denominator roots in the left hand plane, and a good approximation of the complex aerodynamic terms at s - plane.

The approximating function coefficients ( $A_0, A_1, ..., A_6$ ) are evaluated by a least-square curve fitting ( described in Appendix A ) through the values of complex aerodynamic coefficients at discrete values of reduced frequencies. Some results of this approximation will be presented in Section 3.6 when we discussing the calculation of the elements of the generalized aerodynamic forces matrix, $A_{i,j}$.

By substituting Eq. [2.2.4] into Eq. [2.2.3] and following the procedures outlined in Appendix B, the finite-state form of the equation of motion of the wing are reduced

into a system of 6n - first order equations, where n is the number of structural modes used in the computation, which may be expressed as

$$\bar{s}\{Z\} = [H]\{Z\} \qquad [2.2.5]$$

in which $\{Z\}$ represents the state variables that contains the displacements, velocities and augmented states ; and $[H]$ is a 6n x 6n real matrix of constant elements for a fixed value of Mach number, dynamic pressure and free-stream velocity. This is the form of equation of motion, which is suited for an eigenvalue solution, that will be used to study the wing aeroelastic problems.

In cases where the structural nonlinearities exist in the wing structure, Eqs. [2.1.8] and [2.2.5] change slightly. This change and other effects on the mathematical modeling of the aeroelastic wing system will be throughly presented in discussion of the structure model in Section 4.4 of Chapter 4 .

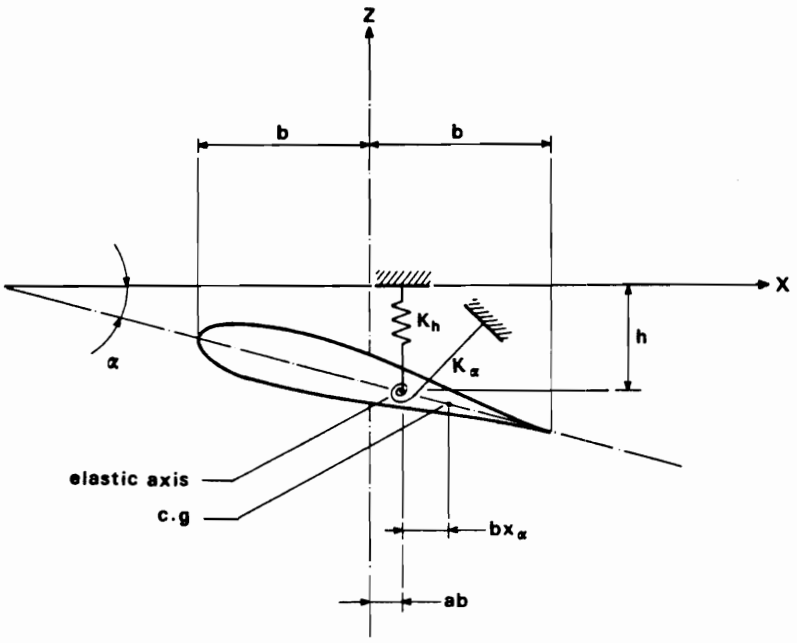


Figure 2.1.1 Two-dimensional airfoil section wing model with pitching, α and plunging, h , degree-of-freedom.

# Chapter 3

# Aerodynamic Model

The objective of this chapter is to describe the transonic aerodynamic loads calculations that are used for the aeroelastic analyses. This chapter includes a brief review of the structure and the nonlinear behavior of the transonic flows, a description of transonic small disturbance ( TSD ) equations that are used in this study, and two solution procedures employed to solve these equations, i.e. the Alternating Direction Implicit ( ADI ) algorithm and the Approximate Factorization ( AF ) algorithm. The Lag-entrainment and Viscous Ramp methods to include the viscous effects into the flow solution are also described. Two techniques used to calculate the finite state generalized aerodynamic forces are also presented. The first technique is the Harmonic Oscillation method and the second technique is the Pulse Transfer-Function Method. Numerical calculations are performed on typical airfoil sections, for two-

dimensional problems, and two wing configurations, namely the F5 wing and a 45° swept wing, which have available experimental wind-tunnel data for comparison.

## 3.1 Overview

The main difficulty in transonic flow computations is that the flow structure is complex and is inherently nonlinear, typified by the appearance of the shock waves in the flow. A typical structure of a transonic flow with subsonic free-stream Mach number and containing supersonic region with a sonic line and shock wave, is given in Fig. 3.1.1 . The complexity of this flow structure becomes more pronounced because of the fact that ( as indicated by in the wind tunnel experiments ) the shock waves are moving. The shocks oscillate forward and backward following the aeroelastic movement of the body surface. Tijdeman, Ref. 40 , divided these shock waves motion into three - categories.

(i) Sinusoidal shock-wave motion ( type A motion ) At a high Mach number, the shock moves sinusoidally with a phase shift with respect to the sinusoidal motion of the body surface. It reaches its maximum strength during its upstream motion and its minimum strength during the downstream motion.

(ii) Interupted shock-wave motion ( type B motion ). This motion, occuring at a slightly lower free-stream Mach number, is characterized by the disappearance of the shock during a part of its downstream motion. As in type A , the shock wave reaches its maximum strength during its upstream motion.

(iii) Upstream - propagated shock-wave motion ( type C motion ). The shock leaves the body surface from the leading edge during its upstream motion, and propagates upstream into the incoming flow as a weak, free shock wave. This type of shock motion can be expected when the body surface has a high frequency and large amplitude oscillation.

The shock-wave movement, which affects the surface boundary layer, changes the pressure distribution over the surface as well as changes the overall aerodynamic coefficients. This can be seen in the results given in Ref. 40 of the local pressure coefficients at constant chordwise station which were plotted as a function of incidence angle. In subsonic flow, the local pressure coefficient varies almost linearly with the incidence angle, implying that the variation is constant and independent of the actual value of the incidence angle. But in the transonic flow region, the pressure coefficients shows a sudden jump at an instant the shock passes that position. The curve show a nonlinear relation between the pressure coefficients and the incidence angle.

In general, transonic flows should be mathematically described by nonlinear equations of mixed elliptic/hyperbolic type, since the subsonic flow is described by an elliptic equation and the supersonic flow by a hyperbolic one. The boundary between the hyperbolic and elliptic solution must be found as part of the solution. The difficulty is that analytic solutions for these mixed equations are generally not available. The early work in this area usually linearized the mixed equations into a simple equation, such as Tricomi's equation, and attempted to solved it, e.g., Ref. 69 . The most common technique used to solve this simplified equation was the hodograph method, in which the role of the dependent and independent variables are inter-

changed. This technique significantly simplifies the equation, but at the cost of considerably complicating the formulation and implementation of the boundary condition. This makes it extremely difficult to apply the hodograph method to the problems with complex body shape.

The nonlinear transonic flow equations are generally solved numerically. There are many methods available for predicting steady and unsteady transonic flows. For aeroelasticity problems the motion of the shock is very important. The complexity of the equations that need to be solved depends on the characteristics of the flow and the coupling mechanism between the aerodynamic and structural model that is used in the aeroelastic analysis. Perhaps the most complex flow is the one induced by wing structure oscillating at large amplitude with strong shock-wave motion, such that the flow is separated. To incorporate the whole complexity of the flow structure, there is little alternative other than to use and solve the Navier - Stoke's equations. On the other hand, if the wing is undergoing only a slight oscillation, with a relatively weak shock-wave, such that the flow is still attached, the flow can be predicted by solving the transonic small-disturbance equation, which is, as mentioned previously, the simplest equation that can describe a typical transonic flow. In between these two extremes, there is a range of flow phenomena that are described by equations of varying complexity.

The second point mentioned above, namely the coupling mechanism that is to be used in the aeroelastic analysis between the structure and aerodynamic model, is important, because the assumptions that are used in deriving the flow model must be compatible with those used in the structural modeling. The choice of the coupling procedure employed in the aeroelastic solution is also dependent on these assump-

tions. In a simple flow pattern, such as in the subsonic flow, with linear structural dynamics, for instance, both the structure and aerodynamic terms can be estimated separately and then combined using superposition principle. This coupling generally is not be valid for cases involving highly nonlinear flow conditions.

Another consideration that must be examined is the amount of resources ( CPU time and storage ) available to solve the problem. This consideration is important in the transonic aeroelastic analysis, since in transonic flow, due to the nonlinearity of the governing equations, these flow calculation have to be performed for several different values of reduced frequency ( defined as $\omega c/U$ , where $\omega$ being the oscillation frequency, c is the chord length and U is the free-stream velocity ) which needs a very large amount of cpu time. Hence, it is desirable that the simplest possible equation is solved for a particular requirement.

In this study, several assumptions are made regarding the structural and aerodynamic modeling and the coupling procedure used in the aeroelastic analysis. These are :

1. There is no separation in the flow field and the viscous effects are weak
2. The oscillation amplitude is small. Even with the introduction of spring stiffness nonlinearity in the structural modeling, the structure motion does not exhibit a limit cycle behavior
3. In the solution of aeroelastic equation in frequency domain, the superposition principle is assumed valid.

With the first two assumptions noted above, the prediction of the aerodynamic force for the problem is carried out using transonic small disturbance equation. The

superposition principle is used in calculating the generalized aerodynamic forces used in the frequency domain and root locus solutions. Since the flow calculation is performed based on the inviscid flow equation, the viscous effect in the flow has to be imposed explicitly during the solution of the flow field. This is carried out using two different techniques, (i) by employing the viscous ramp model in the flow solution to roughly account for shock/boundary layer interaction and (ii) by the application of the lag - entrainment method. In the two-dimensional calculation we use the more detailed lag - entrainment method. As will be discussed in this section, the simpler viscous ramp model will be used for three-dimensional calculation. There are several other methods that have been used to take into account the viscous effect in the flow, but the application of these methods into inviscid unsteady flow calculation ( either based on the full potential equation or the small disturbance equation ) require a significant additional computer time. Hence, their applications are limited, mostly for steady flow calculations.

## 3.2 Transonic Small Disturbance ( TSD ) equation

The transonic small disturbance ( TSD ) equations are derived based on the assumption that the perturbation of the flow to be everywhere small as compared to the unperturbed free-stream values. So, it is permissible, within a certain order of approximation, to assume the existence of a perturbation velocity potential $\phi(x,y,z)$ . Then the velocity components of the flow U, V, and W in x, y, and z direction, respectively, can be written as

$$U = U_o(1 + \phi_{,x})$$

$$V = U_o \phi_{,y}$$

$$W = U_o \phi_{,z} \qquad [3.2.1]$$

where $U_o$ is the free-stream velocity and a comma in the subscript indicates a partial derivative . Consider the continuity equation, which by using the velocity relation given above may be expressed as

$$\rho_{,t} + [\rho(1 + \phi_{,x})]_{,x} + (\rho \phi_{,y})_{,y} + (\rho \phi_{,z})_{,z} = 0$$

and the Bernoulli equation for a perfect gas

$$\phi_{,t} + \phi_{,x} + \frac{1}{2}(\phi_{,x}^2 + \phi_{,y}^2 + \phi_{,z}^2) + \frac{a^2}{(\gamma - 1)} = \frac{1}{M^2(\gamma - 1)}$$

together with the isentropic flow relation

$$d\left(\frac{a^2}{(\gamma - 1)}\right) = a^2 \frac{d\rho}{\rho}$$

where $\rho$ is the mass density of the air, $a$ is the speed of sound and $\gamma$ is the ratio of specific heats. The small disturbance equation is found by combining these three equations and the potential velocity relations, Eq. [3.2.1] , and neglecting the higher order derivatives and the cross terms except the one in x - direction. The most commonly used form of this equation is the one written in the conservation form as

$$\frac{\partial f_0}{\partial t} + \frac{\partial f_1}{\partial x} + \frac{\partial f_2}{\partial y} + \frac{\partial f_3}{\partial z} = 0 \qquad [3.2.2]$$

where $f_0 = -B\phi_{,x} + A\phi_{,t}$

$f_1 = E\,\phi_{,x} + F\,\phi_{,x}^2 + G\,\phi_{,y}^2$

$f_2 = \phi_{,y} + H\,\phi_{,x}\,\phi_{,y}$

$f_3 = \phi_{,z}$

t is the non-dimensional time $= k\bar{t}$

k is the reduced frequency

The coefficients A, B and E are defined as

$$A = M^2k^2 \qquad B = 2M^2k \qquad E = 1 - M^2$$

Several choices are used for the definitions of coefficient F, G and H depending upon the assumptions used in the derivation of the equation, Ref. 70 . The 'classical' definition of this coefficients are given by,

$$F = -\frac{1}{2}(\gamma + 1)M^2$$
$$G = H = 0$$

The values that were introduced by the NLR group ( Amsterdam ), are defined as

$$F = -\frac{1}{2}[3 - (2 - \gamma)M^2]M^2$$
$$G = -\frac{1}{2}M^2$$
$$H = -M^2$$

and the coefficients that are referred to as 'NASA Ames' coefficients are defined as

$$F = -\frac{1}{2}(\gamma + 1)M^2$$
$$G = \frac{1}{2}(\gamma - 3)M^2$$

$$H = -(\gamma - 1) M^2$$

In low frequency approximation, it was assumed that the time scale of the motion is in the same order as the time scale associated with upstream disturbance propagation and that these scales are much larger then the time scales associated with downstream propagation and convection, that is

$$k \equiv \frac{\omega c}{U} \sim (1 - M^2) << 1$$

Hence, in the low frequency approximation, the higher order derivative in time, $\phi_{tt}$ which has coefficient of $M^2k^2$ , can be neglected. As will be shown later in this section, the flow solutions using the general frequency flow equation, in general, give better shock predictions. Therefore, for the aeroelastic calculations in the present study, the general frequency flow equation were used.

Further modification to the TSD equation is sometimes made in which the exponent on M in the expression of coefficient F is replace by an arbitrary constant m . The value of m to be selected in a particular application, referred to as 'transonic scaling' , depends on the solutions and it varies from 1.583 to 2.0 , Ref. 71 . If only weak shocks are expected, then m should be chosen such that the average pressure coefficient , $C_p$ , across the shock is close to the sonic pressure coefficient, $C_p^*$ . In case of stronger shocks, m = 2 should be used. In this study the value of m = 2 is used.

The pressure coefficient on the lifting surface is defined by

$$C_p = \frac{p - p_\infty}{\frac{1}{2} \rho U^2}$$

which can be expressed in terms of perturbation velocity potential as

$$C_p = \frac{2}{\gamma M^2}\left\{\left[1 - \frac{M^2(\gamma-1)}{2}\left(2\phi_{,x} + 2\phi_{,t} + \phi_{,x}^2 + \phi_{,y}^2 + \phi_{,z}^2\right)\right]^{\frac{\gamma}{\gamma-1}} - 1\right\}$$

For small perturbations, the expression inside the square brackets may be expanded in series by using the binomial expansion to obtain the $C_p$ expression as

$$C_p = -2\phi_{,x} - 2\phi_{,t} - (1-M^2)\phi_{,x}^2 - \phi_{,y}^2$$

in which cubic and higher powers of the perturbation velocity are neglected.

### *3.2.1 The boundary conditions*

The conditions that are imposed on the far-field ( outer ) boundary are similar to the nonreflecting boundary conditions introduced by Kwak in Ref. 72 , and Whitlow in Ref. 73 . These boundary conditions are defined as follows :

| | | |
|---|---|---|
| - far upstream | $\phi = 0$ | |
| - far downstream | $\frac{1}{2}\left(\frac{-B}{C} + \frac{D}{\sqrt{C}}\right)\phi_{,t} + \phi_{,x} = 0$ | |
| - far spanwise | $\frac{D}{2}\phi_{,t} + \phi_{,y} = 0$ | |
| - symmetry plane | $\phi_{,y} = 0$ | |
| - far above | $\frac{D}{2}\phi_{,t} + \phi_{,z} = 0$ | |
| - far below | $\frac{D}{2}\phi_{,t} - \phi_{,z} = 0$ | [3.2.3] |

where $C = E + 2F\,\phi_{,x}$ , and $D = \sqrt{4A + B^2/C}$ .

In steady flow solution, the time derivatives $\phi_{,t}$ vanish, resulting in Neumann boundary conditions.

For clean wing configurations, the linearized unsteady flow - tangency condition on the surface, defined by $z = f(x,y,t)$ , is given by

$$\phi_z^{\pm} = f_x^{\pm} + f_t^{\pm} \qquad [3.2.3]$$

where the plus sign indicates the upper surface of the wing and the minus sign indicates the lower surface. The $f_x^{\pm}$ and $f_x$ terms are the slope of the upper and lower surface of the wing, respectively , and the $f_t^{\pm}$ account for the instantaneous displacement of the body. These boundary are applied on the mean surface of the wing which is located along the axis parallel to the streamwise direction, $z = 0$ , equidistantly between two horizontal gridlines.

At the trailing wake, the following boundary conditions are imposed in order to satisfy Kutta condition,

$$[\,\phi_{,z}\,] = 0.$$
$$[\,\phi_{,x} + \phi_{,t}\,] = 0. \qquad [3.2.5]$$

where [ ] indicates the jump across the wake. As for the flow - tangency condition, the wake conditions are applied along the mean surface from the trailing edge of the wing to the far-downstream boundary.

### *3.2.2 The coordinate transformation*

The TSD equation above will be solved using finite - difference methods. To apply this solution procedure, a grid system in the flow domain is required. Such grid system are generated following some general requirements which are associated with the flow structure and the accuracy of the calculation, such as :

- The grid-lines/points close to the body surface should be more dense than the grid-lines/points in the region far from the body surface. This is because of the fact that the variations of the flow parameters are greater in the region close to the body surface.
- In order to be able to capture the local phenomena in the flow field, more lines/points are located at the leading and trailing edge region and also in the region where the shock wave exists.
- The far field boundary have to be located far enough from the surface such that it will not reflect the error back into the computational domain which can contaminate the solution.

For unsteady flow calculations based on TSD equation, the surface boundary conditions need not to be applied on the actual body surface, so that a body-fitted grid system is not required. The surface boundary condition, instead, is applied on the mean surface of the body. This means that its only require a simple grid system that is not moving during the calculation process.

In order to fulfill the requirements that are stated above and to avoid the complexity of the wing planform, flow calculations are not performed directly on the

physical flow domain. Instead, they are performed in a calculation which is obtained by a coordinate transformation of the physical domain.

In two-dimensional flow calculations, the finite-difference grid system in both the physical and computational domains are contained within rectangular regions. The physical grid system in x,z plane is transformed in to some $\xi, \zeta$ plane so that the mesh spacing in both directions can be kept uniform in the computational plane, using transformation function defined as follows, see Fig. 3.2.1 ,

1. z - direction

$$(\frac{z}{c}) = A_1 \tan(\frac{\pi \zeta}{2})$$

2. x - direction

In this direction, the computational plane is divided into three region :

- In region 1 and 3

$$(\frac{x}{c}) = x_0 + A_2 \tan\{ \frac{\pi}{2} (\xi - \xi_0) \} + A_3 \tan\{ \frac{\pi}{2} (\xi - \xi_0)^3 \}$$

- In region 2

$$(\frac{x}{c}) = \xi (a + b\xi^2)$$

where the constants a and b are determined by requiring

$$x = x_0 \text{ and } \frac{dx}{d\xi} = \frac{\pi A_2}{2} \quad at \quad \xi = \xi_0$$

The constant $A_1$ controls the grid spacing near the airfoil surface, $A_2$ controls the grid spacing at the leading edge , and $A_3$ determines the physical location of the grid line adjacent to the far-field boundary.

The grid distribution in the physical plane resulting from this transformation is shown in Fig. 3.2.2 for the value of $x_0 = 0.495$ and $\xi_0 = 0.5$ . The airfoil is placed at the middle plane, between two gridlines in order to simplify the formulation of the surface and wake boundary conditions. The leading edge is also positioned between two vertical lines to avoid the singular point. The grid spacing between these two lines can be adjusted by changing the value of coefficient $A_2$ . This transformation gives finer grid spacing at the leading edge and close to the surface which are needed for improved stability and accuracy in the flow field calculation. The values of $A_1 = 0.001$ , $A_2 = -0.497$ , and $A_3 = 0.5$ were found to be suitable for the stable solutions of all calculations performed in this study.

For the three-dimensional flow problems, a simple shearing transformation was used to map a trapezoidal wing planform into a rectangle in the computation plane, as shown in Fig. 3.2.3 . In Ref. 74 , Guruswamy gave several criteria that a good transformation must satisfy. The important ones are :

1. Far field boundaries are independent of wing planform and must be aligned with the free-stream direction
2. Smooth first and second derivatives should occur for values of the metric quantities , $\xi_x$ , $\xi_y$ , particularly near the boundary, and
3. Grid-lines are clustered near the leading and trailing edge.

Considering these three criteria, a transformation function was chosen in this study as :

$$\xi(x,y) = \frac{[x - x_{le}(y)]}{p(x,y)} \quad , \quad \eta(y) = y \quad , \quad \zeta(z) = z \qquad [3.2.6]$$

where $x_{\leq}(y)$ is the x-ordinate of the leading edge and $p(x,y)$ is the stretching function. The leading edge and trailing edge lie on the coordinate lines $\xi = 0$ and $\xi = 1$ , respectively. Each span station ( $\eta$ = constant ) has the same number of chordwise gridpoints, so there are no discontinuities in the gridlines. The transformation is done in the following way :

- The number of gridpoints in x,y and z directions are specified along with the location of the far field boundaries.
- The physical grid on the wing surface are obtained by the transformation Eq. [3.2.6] in which p (x,y) = $x_{te}(y) - x_{le}(y)$ and $x_{le}(y)$ defining the leading edge position and $x_{te}(y)$ defining the trailing edge position.
- An exponential distribution of grid is constructed at the wing root and based on this distribution and Eq. [3.2.6] in which p (x,y) = $x_{farfield} - x_{le/te}(y)$ , grid distribution in the upstream and downstream region are computed for every section along the wing span.
- In order to ensure a smooth first and second derivatives of the metric quantities, this grid distribution is smoothed by requiring that

$$\xi_y = (\xi_y)_{le/te}\ H(x)$$

where H(x) , shown in Fig. 3.2.4 , is given by

$$H(x) = \frac{a}{4}\bar{x}^4 - \frac{b}{3}\bar{x}^3 - \bar{x}$$

in which $\bar{x}$ is equal to ( x - $x_{le}$ ) or ( x - $x_{te}$ ) , a = 600 and b = -0.225 a .

For wings with high aspect ratios, small sweeps and large taper ratios, the smoothing procedure ( step 4 ) is not necessary. However, for unsteady calculation on wings with low aspect ratios, high sweeps and small taper ratios ( such as the F5 delta wing ), the transformation using step 2 and step 3 only yields highly skewed flow regions which produced a large discontinuous values for the metric $\xi_y$ near the upstream and downstream boundaries. And also the far field grid boundaries are not aligned with the flow direction. These factors can combined to make the unsteady flow computation unstable and time step restriction, as reported in Ref. 75 . Thus, the smoothing step is necessary in order to avoid such instabilities and time step restriction. A grid line distribution for a 45° swept wing configuration generated using this transformation is shown in Figs. 3.2.5a and 3.2.5b .

On the wing surface, from the wing root until the far-spanwise boundary, the grid-lines are equally spaced. From the leading edge to the upstream boundary and from the trailing edge to the downstream boundary, the grid distribution is smoothed to avoid a large skewness of the gridlines which causes large gradients for the metric $\xi_y$ near the far-flow boundaries. It was shown that in the flow calculation using this grid-lines distribution, the numerical instability and time step restriction are not found.

With coordinate transformation, the TSD equation, Eq. [3.2.1] , may then be expressed in computational coordinates $\xi$ , $\eta$ , $\zeta$ as

$$-\frac{\partial}{\partial t}\left[\frac{A\phi_{,t}}{\xi_x}+B\phi_{,\xi}\right]+\frac{\partial}{\partial \xi}\left[E\xi_x\phi_{,\xi}+F\xi_x^2\phi_{,\xi}^2+G(\xi_y\phi_{,\xi}+\phi_{,\eta})^2\right.$$

$$\left.+\frac{\xi_y}{\xi_x}(\xi_y\phi_{,\xi}+\phi_{,\eta})+H\xi_y\phi_{,\xi}(\xi_y\phi_{,\xi}+\phi_{,\eta})\right] \qquad [3.2.7]$$

$$+\frac{\partial}{\partial \eta}\left[\frac{1}{\xi_x}(\xi_y\phi_{,\xi}+\phi_{,\eta})+H\phi_{,\xi}(\xi_y\phi_{,\xi}+\phi_{,\eta})\right]+\frac{\partial}{\partial \zeta}\left[\frac{1}{\xi_x}\phi_{,\zeta}\right]=0$$

## 3.3 Viscous effects

As already mentioned at the beginning that the influence of viscosity on steady and unsteady pressure distribution is not negligible for transonic flows. The primary effects of viscosity in transonic flow over lifting surfaces are ,

1. The shock boundary layer interaction which weakens the shock relative to the inviscid case usually causes a significant upstream displacement of the shock.
2. The difference of the viscous displacement thickness along the aft upper and lower surfaces of the lifting surface changes the load distribution over the entire surface as well as displaces the shocks.
3. The shock boundary layer interaction causes a camber and displacement effects of the near wake.
4. The viscous interaction at the trailing edge can modifies the Kutta condition used in the inviscid flows to establish the local circulation.

In the case where the shock wave is strong enough, a vortex separation or bubble type separation may occur on some portion of the lifting surface or could extend

significantly downstream. In this study, only the interaction in non-separating flows will be considered.

The most important type of shock boundary layer interaction encountered on lifting body in transonic flows involves a normal shock on the upper surface. Because of its effects, this interaction should be included in the transonic flow calculations based on the inviscid flow equations. Some important progress towards the development of two and three-dimensional analyses of this interaction have been made during the past several years.

The approach that has been used most commonly is that of implementing viscous - inviscid coupling, in which a boundary layer solution is coupled with the inviscid flow solutions through the displacement surface. This approach, call interacting boundary-layer theory ( IBLT ) is discussed by Melnik, Ref. 79 and LeBalleur, Peyret and Viviand , Ref. 99 .

For the interaction of the shock wave with a turbulent boundary layer the, the situation becomes more complex. A procedure to account for this interaction was introduced by Lighthill, Ref. 76 , and implemented by Inger and Mason, Ref. 77 . This approach was based upon a two layer description of the asymptotic structure of turbulent boundary layers have been introduced by Melnik and Grossman, Ref. 100 , and Adamson and Messiter, Ref. 101 . These approaches are too complicated be included in the unsteady transonic flow calculations required in the present work. Instead, quasi-steady coupling methods as presented by Rizzetta in Ref. 50 were used. These methods, which will be described in the next section, avoid the iterative procedure required in the interacting boundary-layer theory.

### *3.3.1 The lag - entrainment method*

The lag - entrainment method is applied to account for the viscous effects in two-dimensional flow calculations. This method is developed based on the boundary layer assumption that the normal extent of the viscous region is small when compared with the lifting surface and wake thicknesses. The effect of a viscous boundary layer for attached turbulent flow is modeled in a quasi - steady manner by means of Green's lag - entrainment equations, Ref. 78 . These equations are comprised of three first order ordinary differential equations. Two of them are obtained by integrating the continuity and the streamwise momentum equations in the normal direction, while the third is derived from Bradshaw - Ferriss - Atwell turbulent kinetic energy equation, in a form proposed by Head.

Using these three equations, a relation between the boundary layer thickness and the inviscid upstream properties is found in the form

$$\frac{dU_e}{dx} = (F_2)^{-1} \left(\frac{d\delta_e}{dx} - F_1\right)$$

where $U_e$ is the inviscid outer flow velocity, $\delta_e$ is the displacement thickness, and $F_1, F_2$ are parameters that depend on Mach number, M , shape factor, H , entrainment coefficient, $C_E$ , skin friction coefficient , $C_t$ , and other variables given in detail in Ref. 50 .

Melnik, Ref. 79 , used this equation along with the full potential flow solver and treated it as an equivalent source distribution on the base of the lifting surface.

Rizzetta transformed this equation into the form that is compatible with the transonic small disturbance equation, which can be written as

$$\frac{d\delta_e}{dx} = F_1 + F_2 \phi_{,xx}$$

The term $\phi_{,xx}$ is calculated from the inviscid disturbance equation as explained in the previous section. Downstream of the trailing edge, the same equation is applied on each side of the wake surface independently, with the skin friction coefficient set equal to zero.

Coupling between the boundary layer and inviscid analysis is through the boundary condition on the surface of the lifting body and wake. The boundary conditions given by Eq. [3.2.3] are modified, respectively, as follows

$$\begin{aligned} \phi_{,z}^{\pm} &= f_{,x}^{\pm} + f_{,t}^{\pm} + \frac{d\delta_e}{dx} && \text{on the body surface} \\ \Delta\phi_{,z}^{\pm} &= \Delta\left(\frac{d\delta_e}{dx}\right) && \text{on the wake} \end{aligned} \qquad [3.3.1]$$

In three-dimensional configurations, these boundary conditions are applied at every span sections in the spanwise direction.

### *3.3.2 The Viscous ramp method*

The viscous ramp method is simpler and easier to implement as compared to lag - entrainment method described in the previous section. This method is used to account for viscous effects in the three-dimensional flow calculations. The basis for the

development of the viscous ramp model is the observation in many steady - experiment measurements that the post shock pressure for turbulent flow over an airfoil corresponds approximately to that of the oblique shock produced by flow over a ramp with a wedge slope equal to the detachment angle, Ref. 80 . From this observation, a ramp model was constructed as shown in Fig. 3.3.1 . It consists of a short precursor, of length $x_p$ , over which the surface slope varies from zero to the given wedge angle. This is followed by the main ramp body, of length $x_r$ , along which the slope varies quadratically. The viscous coupling is modeled by placing this ramp structure with respect to the local instantaneous sonic point location on the the surface.

Augmenting the surface geometry by the ramp structure results in the modification to the surface boundary condition, Eq. [3.2.3] , in the manner as it was done in the lag - entrainment method, that is

$$\phi_{,z}^{\pm} = f_{,x}^{\pm} + f_{,t}^{\pm} + f_r \qquad [3.3.2]$$

If $x_s$ is the sonic point location ( from the leading edge ) and $\theta$ is the wedge angle, then $f_r$ is defined as follows, Ref. 80 :

$$\begin{aligned}
f_r &= 0 && \text{for } x < x_1 \\
f_r &= \left(\frac{\theta}{\delta}\right)\left[1 + \frac{(x - x_s + x_o)}{x_p}\right] && \text{for } x_1 \le x \le x_2 \\
f_r &= \left(\frac{\theta}{\delta}\right)\left[1 - \frac{(x - x_s + x_o)}{x_r}\right] && \text{for } x_2 \le x \le x_3 \\
f_r &= 0 && \text{for } x_3 \le x
\end{aligned}$$

$$\left(\frac{\theta}{\delta}\right) = \pm\left[\frac{4}{(1+\gamma)M^2}\right]\left[\frac{1}{3}\left\{(1+\gamma)M^2\phi_{,x} - \frac{(1-M^2)}{\delta^{2/3}}\right\}\right]^{3/2}$$

where $\delta$ is the lifting body thickness

$x_o$ is the off set distance

$$x_1 = x_s - x_o - x_p$$

$$x_2 = x_s - x_o$$

$$x_3 = x_s - x_o + x_r$$

The values for $x_o$ , $x_p$ , and $x_r$ are chosen to be equal to 0.02 , 0.02 and 0.10 , respectively.

## 3.4 Alternating direction implicit algorithm

An alternating direction implicit ( ADI ) algorithm, Ref. 25 , is used to solve the TSD equation in two-dimensional cases. This algorithm is conservative in time and space and, therefore, will correctly simulate unsteady transonic flow.

From the complete TSD equation given in the previous section, Eq. [3.2.7] , the two-dimensional TSD equation in $\xi, \zeta$ plane can be written as

$$k^2 M^2 \phi_{,tt} + 2k^2 M^2 \xi_x \phi_{,\xi} - \{(1 - M^2)\xi_x \phi_\xi - \frac{1}{2}(1 + \gamma) M^m (\xi_x \phi_{,\xi})^2\}_{,\xi} + \zeta_z (\zeta_z \phi_{,\zeta})_{,\zeta} = 0 \qquad [3.4.1]$$

where t is the non-dimensional time, $t = k\bar{t}$. The solution of this equation, in term of the disturbance velocity potential at each grid point (x,z) in the flow field, is advanced from time level n to level (n+1) by the following two - step procedure :

1. $\xi$ - sweep

$$\alpha\,\partial_\xi(\bar{\phi}_{i,k} - \phi^n{}_{i,k}) = D_\xi \bar{f}_{i,k} + \left(\frac{\zeta_z}{\xi_x}\right)[\,\zeta_z\,\partial_\zeta\,\phi^n{}_{i,k}\,] \qquad [3.4.2]$$

2. $\zeta$ - sweep

$$\beta(\phi^{n+1}{}_{i,k} - 2\phi^n{}_{i,k} + \phi^{n-1}{}_{i,k}) + \alpha\,\partial_\xi(\phi^{n+1}{}_{i,k} - \bar{\phi}_{i,k}) = \left(\frac{\zeta_z}{2\xi_x}\right)\partial_\zeta[\,\zeta_z\,\partial_\zeta(\phi^{n+1}{}_{i,k} - \phi^n{}_{i,k})] \qquad [3.4.3]$$

where $\alpha = \dfrac{2\,k\,M^2}{\Delta t}$ $\qquad \beta = \dfrac{k^2 M^2}{(\Delta t)^2}$

In the first sweep, Eq. [3.4.2] is solved for the intermediate value $\bar{\phi}_{i,k}$ at the grid points along the grid-lines in the streamwise - direction. After the computation is completed for the whole computation domain, from k = 1 until k = kmax , the second sweep is performed for the solution of $\phi_{i,k}$ . The calculation is carried out along the grid-lines perpendicular to the streamwise - direction, starting from the upstream boundary ( i = 1 ) until the downstream boundary ( i = imax) .

The $D_\xi \bar{f}_{i,j}$ term is defined by

$$D_\xi \bar{f}_{i,k} = \frac{2}{\xi_{i+1} - \xi_{i-1}}\left\{(\hat{f}_{i+\frac{1}{2},k} - \hat{f}_{i-\frac{1}{2},k}) - (\tilde{f}_{i-\frac{1}{2},k} - \tilde{f}_{i-\frac{3}{2},k})\right\}$$

$$\hat{f}_{i+\frac{1}{2},k} = \frac{1}{2}\left\{c_i\,\hat{u}_{i+\frac{1}{2},k} + (\xi_x)_{i+\frac{1}{2}}(c_1 + 2\,c_2\,\hat{u}_{i+\frac{1}{2},k})\,\partial_\zeta\,\tilde{\phi}_{i+1,k}\right\}$$

$$\hat{f}_{i-\frac{1}{2},k} = \frac{1}{2}\left\{c_i\,\hat{u}_{i-\frac{1}{2},k} + (\xi_x)_{i-\frac{1}{2}}(c_1 + 2\,c_2\,\hat{u}_{i-\frac{1}{2},k})\,\partial_\zeta\,\tilde{\phi}_{i-1,k}\right\}$$

$$\tilde{f}_{i-\frac{1}{2},k} = \frac{1}{2}\left\{c_i\,\tilde{u}_{i-\frac{1}{2},k} + (\xi_x)_{i-\frac{1}{2}}(c_1 + 2\,c_2\,\tilde{u}_{i-\frac{1}{2},k})\,\partial_\zeta\,\tilde{\phi}_{i,k}\right\}$$

$$\tilde{f}_{i-\frac{3}{2},k} = \frac{1}{2}\left\{ c_i \tilde{u}_{i-\frac{3}{2},k} + (\xi_x)_{i-\frac{3}{2}} (c_1 + 2 c_2 \tilde{u}_{i-\frac{3}{2},k}) \partial_\zeta \tilde{\phi}_{i-1,k} \right\}$$

$$\hat{u}_{i+\frac{1}{2},k} = \bar{u} + (1 + \varepsilon_{i,k})(1 + \varepsilon_{i+\frac{1}{2},k}) [\, u^n{}_{i+\frac{1}{2},k} - \bar{u} \,]$$

$$\tilde{u}_{i-\frac{1}{2},k} = \bar{u} + \varepsilon_{i,k}\varepsilon_{i-\frac{1}{2},k} [\, u^n{}_{i-\frac{1}{2},k} - \bar{u} \,]$$

$$\bar{u} = -\frac{c_1}{2 c_2}$$

$$u^n{}_{i+\frac{1}{2},k} = (\xi_x)_{i+\frac{1}{2}} (\xi_{i+1} - \xi_i)^{-1} (\phi^n{}_{i+1,k} - \phi^n{}_{i,k})$$

$$u^n{}_{i-\frac{1}{2},k} = (\xi_x)_{i-\frac{1}{2}} (\xi_i - \xi_{i-1})^{-1} (\phi^n{}_{i,k} - \phi^n{}_{i-1,k})$$

$$c_1 = (1 - M^2) \quad \text{and} \quad c_2 = -\frac{1}{2}(1 + \gamma) M^m$$

$$\varepsilon_i = 0 \quad \text{if } u^n{}_{i,k} \le 0 \qquad\qquad \varepsilon_{i+\frac{1}{2}} = 0 \quad \text{if } u^n{}_{i+\frac{1}{2},k} \le 0$$

$$= 1 \quad \text{if } u^n{}_{i,k} > 0 \qquad\qquad = 1 \quad \text{if } u^n{}_{i+\frac{1}{2},k} > 0$$

$$u^n{}_{i,k} = \frac{1}{2} (u^n{}_{i+\frac{1}{2},k} + u^n{}_{i-\frac{1}{2},k})$$

The matrix equation of the $\xi$ - sweep can be obtained by substituting all these expression into Eq. [3.4.1] , and used second - order accurate expression for $\partial_\xi$ and $\partial_\zeta$ operators,

$$A_1 \tilde{\phi}_{i-2,k} + A_2 \tilde{\phi}_{i-1,k} + A_3 \tilde{\phi}_{i,k} + A_4 \tilde{\phi}_{i+1,k} = R_{i,k} \qquad [3.4.4]$$

$$A_1 = \tilde{b}_4 \qquad A_2 = -2\alpha\Delta\xi - \tilde{a}_4 - \tilde{b}_2 - \tilde{b}_4$$

$$A_4 = -\tilde{a}_2 \qquad A_3 = 2\alpha\Delta\xi + \tilde{a}_2 + \tilde{a}_4 + \tilde{b}_2$$

$$R_{i,k} = 2\alpha\Delta\xi\,(\phi^n_{i,k} - \phi^n_{i-1,k}) + \Delta\xi\,(\tilde{a}_1 - \tilde{a}_3 - \tilde{b}_1 + \tilde{b}_3) + \left(\frac{2\xi_x}{\zeta_z}\right)$$
$$\left(\frac{\Delta\xi}{\Delta\zeta}\right)^2 \{(\zeta_z)_{k+\frac{1}{2}}(\phi^n_{i,k+1} - \phi^n_{i,k}) - (\zeta_z)_{k-\frac{1}{2}}(\phi^n_{i,k} - \phi^n_{i,k-1})\}$$

$$\tilde{a}_1 = c_1\,\hat{u}_{i+\frac{1}{2},k} \qquad \tilde{a}_2 = (\xi_x)_{i+\frac{1}{2}}(c_1 + c_2\,\hat{u}_{i+\frac{1}{2},k})$$
$$\tilde{a}_3 = c_1\,\hat{u}_{i-\frac{1}{2},k} \qquad \tilde{a}_4 = (\xi_x)_{i-\frac{1}{2}}(c_1 + c_2\,\hat{u}_{i-\frac{1}{2},k})$$

$$\tilde{b}_1 = c_1\,\tilde{u}_{i-\frac{1}{2},k} \qquad \tilde{b}_2 = (\xi_x)_{i-\frac{1}{2}}(c_1 + c_2\,\tilde{u}_{i-\frac{1}{2},k})$$
$$\tilde{b}_3 = c_1\,\tilde{u}_{i-\frac{3}{2},k} \qquad \tilde{b}_4 = (\xi_x)_{i-\frac{3}{2}}(c_1 + c_2\,\tilde{u}_{i-\frac{3}{2},k})$$
$$\Delta\xi = \frac{1}{2}(\xi_{i+1} - \xi_{i-1}) \qquad \Delta\zeta = \frac{1}{2}(\zeta_{k+1} - \zeta_{k-1})$$

In a similar way, the matrix equation for the $\zeta$ - sweep can be written as

$$B_1\,\phi^{n+1}_{i,k-1} + B_2\,\phi^{n+1}_{i,k} + B_3\,\phi^{n+1}_{i,k+1} = \bar{R}_{i,k} \qquad [3.4.5]$$

This is a tridiagonal matrix whose elements are defined by

$$B_1 = -\{(\zeta_z)_k\,(\zeta_z)_{k-\frac{1}{2}}\} / \{(\xi_x)_i\,(\Delta\zeta)^2\}$$
$$B_2 = \{(\zeta_z)_k / (\xi_x)_i\,(\Delta\zeta)^2\}\{(\zeta_z)_{k+\frac{1}{2}} + (\zeta_z)_{k-\frac{1}{2}}\} + (2\alpha / \Delta\xi) + 2\beta$$
$$B_3 = -\{(\zeta_z)_k\,(\zeta_z)_{k+\frac{1}{2}}\} / \{(\xi_x)_i\,(\Delta\zeta)^2\}$$

$$\bar{R}_{i,k} = \left(\frac{2\alpha}{\Delta\zeta}\right)(\phi^{n+1}_{i-1,k} + \tilde{\phi}_{i,k} - \tilde{\phi}_{i-1,k}) - 2\beta\,(\phi^n_{i,k+1} - 2\phi^n_{i,k}) -$$
$$\left\{\frac{(\zeta_z)_k}{zi_{xi}\,(\Delta\zeta)^2}\right\}\{(\zeta_z)_{k+1}(\phi^n_{i,k+1} - \phi^n_{i,k}) - (\zeta_z)_{k-\frac{1}{2}}(\phi^n_{i,k} - \phi^n_{i,k-1})\}$$

Since the $D_\zeta\,\bar{f}_{i,k}$ is differenced by a first - order accurate backward difference, even if a second - order accurate operator is used for $\partial_{\zeta\zeta}$ , the spatial derivatives in Eq.

[3.4.3] are only first order accurate. It follows that the combination of Eqs. [3.4.4] and [3.4.5] will also have first - order accuracy. Hence, the overall spatial derivatives of the difference scheme for Eq. [3.4.1] are only first order accurate.

This solution algorithm is non - iterative. That is, the solution for time level $n+1$ is obtained directly after two - sweeps through the grid system. On the $\xi$ - sweep , the generated matrix is a lower tridiagonal matrix for supersonic points ( $\varepsilon_{k-1} = \varepsilon_k = 1$ ) , and a tridiagonal matrix for subsonic points ( $\varepsilon_{k-1} = \varepsilon_k = 0$ ) . A banded matrix solver from the IMSL routines is used to solve the matrix equation for the values of $\tilde{\phi}_{i,k}$ . On the $\zeta$ - sweep , only $\xi$ - differences are in the $\partial_\xi$ operator, which is backward differenced. Hence, the scheme is marched from the upstream to downstream by solving a tridiagonal matrix equation for each $\xi$ = constant line.

This ADI scheme has no time - step restriction based on a linear stability analysis. However, an instability can be generated by the motion of the shocks across which the differencing switches from backward to central difference. To keep the stability of the calculation, $\Delta t$ must be chosen small enough that the shock wave does not move more than one spatial grid point per time step. So, at every time step the new position of the shock is computed. If the shock position move more than one spatial grid from the previous position, then the value of $\Delta t$ is reduced by 10% of its current value.

The boundary conditions applied in the computational plane are defined in Section 3.2.1. These conditions are numerically imposed by redefining the matrix equations , Eqs. [3.4.4] and [3.4.5] at the appropriate grid points.

The farfield boundary conditions ( upstream, downstream, far above and below ) , Eq. [3.2.3] , are applied by writing the finite - difference approximation for these boundary equations, casting them in the matrix form similar to Eq. [3.4.4] or [3.4.5] , and including them with the matrix equations for the solution.

The downstream boundary, for instance, at the boundary points i = imax may be expressed as

$$(\tilde{\phi}_{,t})^{n+\frac{1}{2}} - b_{i-\frac{1}{2},k}(\tilde{\phi}_{,\xi})^{n+\frac{1}{2}} = 0$$

where $$(b_{i-\frac{1}{2},k})^{-1} = \frac{1}{2}\left(-B/C + D/\sqrt{C}\right)$$

$$\tilde{\phi}^{n+\frac{1}{2}} = (\tilde{\phi} + \phi^n)/2$$

The difference equation of this boundary equation become

$$\tilde{\phi}_{i,k} = -\bar{A}_2\,\tilde{\phi}_{i-1,k} + \bar{A}_2\,\phi^n{}_{i,k} + \phi^n{}_{i-1,k}$$

$$\bar{A}_2 = (1 - A_1\Delta t)/(1 + A_1\Delta t)$$

$$A_1 = b_{i-\frac{1}{2},k}(\xi_x)_{i-\frac{1}{2}}/\Delta\xi$$

This equation is used to replaced equation [3.4.4] in $\xi$ - sweep at point i = imax and $\zeta$ = constant. The other far-field boundary conditions are treated in a similar fashion as described above. The wing flow tangency used is defined by Eq. [3.3.1] in which the viscous effects are modeled using the lag - entrainment method. This boundary is imposed in both of the sweeps through the $\partial_{\zeta\zeta}$ terms. This term is approximated by

$$\partial_{\zeta\zeta}\,\phi^{n+1}_{i,k} = \frac{1}{\Delta\zeta}\left[(\phi_{,\zeta})^{n+1}_{i,k+\frac{1}{2}} - (\phi_{,\zeta})^{n+1}_{i,k-\frac{1}{2}}\right]$$

where the derivative at the right hand - side are written at half node points. As mentioned earlier, the airfoil is located equidistantly between two horizontal gridlines. For points along the line directly above the airfoil surface, the $(\phi_{,\zeta})^{n+1}_{i,k-\frac{1}{2}}$ in the equation above is replaced by

$$(\phi_{,\zeta})^{n+1}_{i,k-\frac{1}{2}} = \left(f^{+}_{,x} + f_{,t} + \frac{d\delta_e}{dx}\right)^{n+1}$$

And for the points along the line below the airfoil surface, this term is replaced by

$$(\phi_{,\zeta})^{n+1}_{i,k+\frac{1}{2}} = \left(f^{-}_{,x} + f_{,t} + \frac{d\delta_e}{dx}\right)^{n+1}$$

Since these terms are known quantities, they can be kept at the right hand - side of Eq. [3.4.5] , resulting in a bi-diagonal matrix in $\xi$ - sweep.

The wake boundary conditions, Eq. [3.2.5] , are imposed at the downstream region, in a similar manner as for the wing flow tangency. It is incorporated into the solution by requiring that the perturbation velocity in the vertical direction, $\zeta$ - direction, be continuous across the wake , $[\,\phi_{,\zeta}\,] = 0$ . This implies that the perturbation velocity must be redefined such that

- for points along the line above the airfoil surface

$$(\phi_{,\zeta})^{n+1}_{i,k-\frac{1}{2}} = \frac{1}{\Delta\zeta}\left(\phi_{i,k} - \phi_{i,k-1} - \Gamma\right)^{n+1}$$

- for points along the line below the airfoil surface

$$(\phi_{,\zeta})^{n+1}_{i,k+\frac{1}{2}} = \frac{1}{\Delta\zeta}\left(\phi_{i,k+1} - \phi_{i,k} - \Gamma\right)^{n+1}$$

The circulation, $\Gamma$ , at new time level $n+1$ , has to be computed before the flow field downstream of the airfoil can be updated. It can be obtained from the second wake condition , $[\ \phi_{,\zeta} + \phi_{,t}\ ] = 0$ , which is equivalent to

$$\Gamma_{,\xi} + \Gamma_{,t} = 0 \qquad [3.4.6]$$

Since the $\zeta$ - sweep is marched in increasing k, the new circulation $\Gamma^{n+1}$ is obtained starting from the values at the trailing edge,

$$\Gamma^{n+1} = \phi^{+}_{te} - \phi^{-}_{te}$$

and this values is applied in the Eq. [3.4.6] to find the values of $\Gamma^{n+1}$ for the points downstream the airfoil.

To asses the accuracy of this solution procedure, calculation was performed on NACA64A006 airfoil section with an oscillating trailling - edge flap, as shown in Fig. 3.4.1 The flap has a length of 0.25 chord. The calculation was carried out for the free-stream Mach number = 0.875 , reduced frequency of the flap motion k = 0.1170 and the oscillation amplitude of 0.5 degree. The grid system in the computational domain has 99x80 grid points in the $\xi$ , $\zeta$ directions. Since the nonreflecting boundary conditions are imposed in this solution procedure, the farfield boundary does not need to be located 1000 chord lengths away from the airfoil such as in LTRAN2 solution, Ref. 25 . The upstream and downstream boundary are located 20 chord lengths away from the leading and trailing edge, respectively, and the upper and lower boundaries about 10 chord lengths away from the mean surface. The integration time step were chosen $\Delta t = 3°$ , which is corresponding to 120 time steps per cycle of oscillatory motion. The unsteady computations were initiated by using the steady - state relaxation solutions. The unsteady equations were then integrated in time for

several cycles until the solution become periodic ( usually about 2 to 4 cycles; in this particular problem 2 cycles were found to be adequate ).

Figure 3.4.2 compares computed results of the upper surface pressure distribution at $t = 0°$ and $t = 180°$ , obtained using the code that has been developed in this study with the one obtained by Ballhaus and Goorjian using LTRAN2 , Ref. 25 . These two results, in general, are comparable with the results from the present study giving a stronger shock wave strength at an approximately equal shock position. The difference in the prediction of the shock strength can mainly be attributed to the fact that LTRAN2 solution used the low frequency approximation, while the result from this study was obtained using the general frequency equation ( $\phi_{,tt}$ term included ) . Another important difference that may be a contributing factors is the difference in the finite-difference switching across the shock between the two solutions ( LTRAN2 solution use Murman - Cole switching and the present procedure employed differencing switching roughly based on the approach of Gudonov, Ref. 81, for Euler equation and implemented for the TSD equation by Goorjian, Ref. 34 ) , also the difference in the boundary conditions and grid system used in the calculations. In Ref. 25 it was stated that the LTRAN2 results are qualitatively similar to the wind - tunnel experiment data by Tijdeman, with weaker shock strengths.

The time history of the upper surface pressure coefficient is shown in Fig. 3.4.3 . A type A shock motion ( according to Tijdeman classification ) is observed in this result. The shock wave is moving almost sinusoidally following the sinusoidal motion of the flap. Note the phase shift between the shock wave location and the flap motion. The maximum downstream excursion of the shock does not occur when the flap reaches its maximum downward position. And also it shows that the shock strength is not in

phase with the shock motion. The shock obtained its maximum strength slightly after passing its maximum downstream position. Similar results from the calculation using the low frequency approximation is presented in Fig. 3.4.4 . As expected, this low frequency solution, in general, predicts weaker shock wave strength and smaller shock wave motion amplitude. The difference between this result and the result from the general frequency solution becomes more significant as the amplitude of the flap motion is increased.

The comparison of these numerical results shows that the solution procedure developed in this investigation gives good predictions of unsteady aerodynamic flows at transonic regime. This procedure is unconditionally stable without time step restriction. The use of the general frequency equation instead of the low frequency approximation equation avoids the restriction on the value of reduced frequency, which can be consider as an advantage for general aeroelastic analyses.

## 3.5 Approximate factorization algorithm

ADI algorithm becomes very expensive for application to the three-dimensional flow calculations because not all sweep in the algorithm can be written in the vectorized form, Ref. 74. An approximate factorization developed by Batina, Ref. 82, for TSD equation was proven more efficient for three-dimensional flow calculations. This approximate factorization ( AF ) algorithm is used in this study which consists of a time linearization procedure coupled with a Newton iteration technique. For un-

steady flow calculation, the solution procedure involves two - steps, as shown in Fig. 3.5.1 ,

1. a time linearization step to determine an estimate values of the perturbation potential

2. a Newton iteration is carried out, with the estimate values of the perturbation velocity from the linearization step as the starting values, to provide time accuracy in the solution.

Newton iteration is not needed in the steady flow calculation since time accuracy is not required when marching to steady state solution. So, the steady flow calculations involve only the time linearization step. The Newton iteration in unsteady flow calculations taking typically 2-3 iterations. The flow equation, Eq. [3.2.7] , is written in the form

$$R(\phi^{n+1}) = 0$$

where $\phi^{n+1}$ represent the perturbation potential at time level $n+1$ . Applying Newton iteration to this equation with estimate value, $\phi^*$ , gives

$$R(\phi^*) + \left(\frac{\partial R}{\partial \phi}\right)_{\phi=\phi^*} \Delta\phi = 0$$

At the convergence of the the iteration, the error in the potential , $\Delta\phi$ , approaches zero, so that the solution is given by

$$\phi^{n+1} = \phi^* + \Delta\phi \equiv \phi^* \qquad [3.5.1]$$

The mathematical formulation of this AF algorithm is derived by first approximating the time derivative terms, $\phi_{,\xi\xi}$ and $\phi_{,\eta\eta}$, using second - order accurate finite difference fomulae,

$$\frac{\partial \phi_{,\xi}}{\partial t} = [\,(3\phi^{n+1}_{,\xi} - 4\phi^{n}_{,\xi} + \phi^{n-1}_{,\xi})/2\Delta t\,] + O(\Delta t^3)$$

$$\frac{\partial^2 \phi}{\partial t^2} = [\,(2\phi^{n+1} - 5\phi^{n} + 4\phi^{n-1} - \phi^{n-2})/(\Delta t^2)\,] + O(\Delta t^3)$$

By substituting $\phi^{n+1} = \phi^{*} + \Delta\phi$ into each terms in Eq. [3.2.7], and combining with the time derivative terms, gives

$$\begin{aligned}
&-(\frac{2A}{\xi_x}\Delta t^2)\Delta\phi - (\frac{3B}{2\Delta t})\Delta\phi_{,\xi} + \frac{\partial}{\partial\xi}\{(\xi_x E + 2F\xi_x^2\phi^{*}_{,\xi})\Delta\phi_{,\xi} + \\
&G(\xi_y\Delta\phi_{,\xi} + \Delta\phi_{,\eta})^2 + (\frac{\xi_y}{\xi_x})(\xi_y\Delta\phi_{,\xi} + \Delta\phi_{,\eta}) + H\xi_y\phi^{*}_{,\xi}(\xi_y\Delta\phi_{,\xi} + \Delta\phi_{,\eta})\} + \\
&\frac{\partial}{\partial\eta}\{\frac{1}{\xi_x}(\xi_y\Delta\phi_{,\xi} + \Delta\phi_{,\eta})\} + \frac{\partial}{\partial\zeta}\{\frac{\Delta\phi_{,\zeta}}{\xi_x}\} = \\
&-(\frac{A}{\xi_x})[\,\frac{(2\phi^{*} - 5\phi^{n} + 4\phi^{n-1} - \phi^{n-2})}{(\Delta t^2)}\,] - \\
&B[\,\frac{(3\phi^{*}_{,\xi} - 4\phi^{n}_{,\xi} + 5\phi^{n+1}_{,\xi})}{2\Delta t}\,] + \frac{\partial}{\partial\xi}\{(\xi_x E + F\xi_x^2\phi^{*2}_{,\xi}) - \\
&G(\xi_y\phi^{*}_{,\xi} + \phi^{*}_{,\eta})^2 + (\frac{\xi_y}{\xi_x})(\xi_y\phi^{*}_{,\xi} + \phi^{*}_{,\eta}) + H\xi_y\phi^{*}_{,\xi}(\xi_y\phi^{*}_{,\xi} + \phi^{*}_{,\eta})\} + \\
&\frac{\partial}{\partial\eta}\{\frac{1}{\xi_x}(\xi_y\phi^{*}_{,\xi} + \phi^{*}_{,\eta}) + H\phi^{*}_{,\xi}(\xi_y\phi^{*}_{,\xi} + \phi^{*}_{,\eta})\} + \frac{\partial}{\partial\zeta}\{\frac{\phi^{*}_{,\zeta}}{\xi_x}\}
\end{aligned} \qquad [3.5.2]$$

which can be written symbolically as

$$N\Delta\phi = R(\phi^{*}, \phi^{n}, \phi^{n-1}, \phi^{n-2}) \qquad [3.5.3]$$

The right hand - side of Eq. [3.5.2] is simply the original TSD equation in term of $\phi^*$ , meanwhile the left hand - side is made up of terms containing $\Delta\phi$ and its derivatives. By approximating the left hand - side of this equation using a triple product of operators and rearranging the results, the AF scheme may be presented as

$$L_\xi L_\eta L_\zeta \Delta\phi = R(\phi^*, \phi^n, \phi^{n-1}, \phi^{n-2}) \qquad [3.5.4]$$

$$L_\xi = 1 + (\frac{3B}{4A})\xi_x \Delta t \frac{\partial}{\partial\xi} - \xi_x(\frac{\Delta t^2}{2A})\frac{\partial}{\partial\xi} F_1 \frac{\partial}{\partial\xi}$$

$$L_\eta = 1 - (\frac{\Delta t^2}{2A})\frac{\partial}{\partial\eta} F_2 \frac{\partial}{\partial\eta}$$

$$L_\zeta = 1 - (\frac{\Delta t^2}{2A})\frac{\partial}{\partial\zeta} F_3 \frac{\partial}{\partial\zeta}$$

$$F_1 = \xi_x E + 2F\xi_x^2 \phi^*_{,\xi} + 2G\xi_y(\xi_y \phi^*_{,\xi} + \phi^*_{,\eta}) + (\frac{\xi_y^2}{\xi_x})(1 + H\xi_x \phi^*_{,\xi}) + H\xi_y(\xi_y \phi^*_{,\xi} + \phi^*_{,\eta})$$

$$F_2 = \frac{1}{\xi_x}(1 + H\xi_x \phi^*_{,\xi})$$

$$F_3 = \frac{1}{\xi_x}$$

and R is equal to the right hand - side of Eq. [3.5.2] .

Equation [3.5.3] is solved through three - sweeps in the computational domain by sequentially applying the differential operators $L_{,\xi}, L_{,\eta}, L_{,\zeta}$ as

$$\xi - \text{sweep} \qquad L_\xi \Delta\tilde{\phi} = -R$$

$$\eta - \text{sweep} \qquad L_\eta \Delta\bar{\phi} = \Delta\tilde{\phi}$$

$$\zeta - \text{sweep} \qquad L_\zeta \Delta\phi = \Delta\bar{\phi} \qquad [3.5.5]$$

In the first sweep, the calculation is carried out along the grid-lines in the streamwise direction ( $\eta, \zeta$ = constant ). Using the intermediate value $\Delta\tilde{\phi}$ from the first sweep, the second sweep is performed along the grid-lines in the spanwise direction ( $\xi, \zeta$ = constant ) for the values of $\Delta\bar{\phi}$ . Once this sweep is completed, the updated values for $\Delta\phi$ are computed by applying the last sweep along the vertical grid-lines ( $\xi, \eta$ = constant ). With the updated values of $\Delta\phi$ , the new values of the perturbation potential are obtained from Eq. [3.5.1].

The computation is started with the estimate values $\phi^*$ and is carried out until a convergence solution for $\phi^{n+1}$ is obtained ( until the perturbation error $\Delta\phi$ reaches the value of $10^{-6}$ ). In most of the computation that had been performed in this study, a maximum of 3 Newton iterations are needed to obtained converged solution.

Using the $\phi^{n+1}$ values, the time linearization step is carried through to obtained the new estimate values $\phi^*$ for the next time step. In this step, the wing surface is put at their new position ( so an updated surface boundary condition is applied ). The unsteady solution are initiated using the steady - state solution as the first estimate values.

Since the solution at each sweep depended entirely on the values that have been computed at the previous sweep, all of these sweeps can be coded in vectorized form. This is in contrast to the ADI scheme in which only one sweep, i.e., the sweep in streamwise direction , is fully vectorizable. In steady flow calculations, the convergence to the steady state solution can be accelerated by adding a relaxation parameter , $\sigma$ , into the right hand - side of the first sweep. This parameter can have a value of $> 1$ , and a value of 2.0 has proven suitable for all cases studied.

A central difference formula is used for all of the derivatives in the computation plane except for the region across the shocks. An Engquist - Osher ( E-O ) type - dependent mixed difference operator, Ref. 83 , is used to treat the switch between the subsonic and supersonic regions of the flow. This difference operator is a modification of the scheme introduced by Murman and Cole, Ref. 32 , and is design such that the non - physical expansion shocks do not occur. As in the scheme of Murman and Cole, the E-O scheme is based on sonic reference conditions and is applied on both sides of the equation in the $\xi$ - sweep.

The term in the streamwise direction of the residual, R , for instance, is written as

$$\frac{\partial}{\partial \xi}\left(E\,\xi_x + F\,\xi_x^2\,\phi^*_{,\xi^2}\right) = \frac{1}{\Delta\xi}\left\{\left(\tilde{f}_{i+\frac{1}{2}} - \tilde{f}_{i-\frac{1}{2}}\right) + \left(\hat{f}_{i-\frac{1}{2}} - \hat{f}_{i-\frac{3}{2}}\right)\right\}$$

$$\tilde{f}_{i-\frac{1}{2}} = E\,\tilde{u}_{i-\frac{1}{2}} + F\,\tilde{u}^2_{i-\frac{1}{2}}$$

$$\hat{f}_{i-\frac{1}{2}} = E\,\hat{u}_{i-\frac{1}{2}} + F\,\hat{u}^2_{i-\frac{1}{2}}$$

$$\tilde{u}_{i-\frac{1}{2}} = \bar{u} + \left(1 - \varepsilon_{i-\frac{1}{2}}\right)\left(u^*_{i-\frac{1}{2}} - \bar{u}\right)$$

$$\hat{u}_{i-\frac{1}{2}} = \bar{u} + \varepsilon_{i-\frac{1}{2}}\left(u^*_{i-\frac{1}{2}} - \bar{u}\right)$$

$$u^*_{i-\frac{1}{2}} = \bar{\delta}_\xi\,\phi_i = \left(\frac{\xi_x}{\Delta\xi}\right)_{i-\frac{1}{2}}\left(\phi^*_i - \phi^*_{n-1}\right)$$

$\bar{u}$ is the sonic value of the perturbation potential

$$\varepsilon_{i-\frac{1}{2}} = 1 \quad \text{if } u^*_{i-\frac{1}{2}} > \bar{u}$$
$$= 0 \quad \text{if } u^*_{i-\frac{1}{2}} \leq \bar{u}$$

The same switch formula is used for the first and second terms in $F_1$ . Applying the difference formula to each terms in all three sweeps, resulting in a system of matrix

equations. The $\xi$ - sweep is presented by a quadri - diagonal matrix, while both the $\eta$ , and $\zeta$ - sweeps formed a tridiagonal matrix equations.

$\xi$ - sweep

$$a_1 \Delta\tilde{\phi}_{i-2} + a_2 \Delta\tilde{\phi}_{i-1} + a_3 \Delta\tilde{\phi}_i + a_4 \Delta\tilde{\phi}_{i+1} = -\sigma R$$

$$a_1 = -\alpha_2 \hat{f}_{i-\frac{3}{2}}$$

$$a_2 = -\alpha_1 - \alpha_2 (\tilde{f}_{i-\frac{1}{2}} - \hat{f}_{i-\frac{1}{2}} - \hat{f}_{i-\frac{3}{2}} - g_{i-\frac{1}{2}})$$

$$a_3 = 1 + \alpha_1 - \alpha_2 (\hat{f}_{i-\frac{1}{2}} - \tilde{f}_{i-\frac{1}{2}} - \tilde{f}_{i+\frac{1}{2}} - g_{i+\frac{1}{2}} + g_{i-\frac{1}{2}})$$

$$a_4 = -\alpha_2 (g_{i+\frac{1}{2}} + \hat{f}_{i+\frac{1}{2}})$$

$$\alpha_1 = (3B / 4A)(\Delta t / \Delta\xi)\, \xi_x$$

$$\alpha_2 = (\xi_x / 2A)(\Delta t / \Delta\xi)^2$$

$$g = 2G\, \xi_y (\xi_y \phi^*_{,\xi} + \phi^*_{,\eta})^2 + (\frac{\xi_y^2}{\xi_x})(1 + H\, \xi_x \phi^*_{,\xi}) + H\, \xi_y (\xi_y \phi^*_{,\xi} + \phi^*_{,\eta})^2$$

$\eta$ - sweep

$$b_1 \Delta\bar{\phi}_{j-1} + b_2 \Delta\bar{\phi}_j + b_3 \Delta\bar{\phi}_{j+1} = \Delta\tilde{\phi}_j$$

$$b_1 = -\beta_1 (F_2)_{j-\frac{1}{2}}$$

$$b_2 = 1 - \beta_1 \{ (F_2)_{j+\frac{1}{2}} + (F_2)_{j-\frac{1}{2}} \}$$

$$b_3 = \beta_1 (F_2)_{j+\frac{1}{2}}$$

$$\beta_1 = (\xi_x / 2A)(\Delta t / \Delta \eta)^2$$

$\zeta$ - sweep

$$c_1 \Delta\phi_{k-1} + c_2 \Delta\phi_k + c_3 \Delta\phi_{k+1} = \Delta\bar{\phi}_k$$

$$c_1 = -\gamma_1 (F_3)_{k-\frac{1}{2}}$$

$$c_2 = 1 + \gamma_1 \{ (F_3)_{k+\frac{1}{2}} + (F_3)_{k-\frac{1}{2}} \}$$

$$c_3 = -\gamma_1 (F_3)_{k+\frac{1}{2}}$$

$$\gamma_1 = (\xi_x / 2A)(\Delta t / \Delta \zeta)^2$$

The time linearization step is carried out, as mentioned earlier, to generate estimate value, $\phi^*$, as starting values in the Newton iteration. A time linearized version of Eq. [3.5.2] is used, in which the equation is linearized about time level n instead of iterate level ( * ),

$$R(\phi^n) + \left(\frac{\partial R}{\partial \phi}\right)_{\phi=\phi^n} \Delta\phi = 0$$

$$\phi^* = \phi^n + \Delta\phi$$

The resulting equations are the same with the equation derived for the Newton iteration step, except $\phi^*$ now is replaced by $\phi^n$. So, the equation for the linearization step may be written as

$$L_\xi L_\eta L_\zeta \Delta\phi = R(\phi^n, \phi^{n-1}, \phi^{n-2}) \qquad [3.5.6]$$

where $L_\xi$ , $L_\eta$ , $L_\zeta$ operators and R have the same definitions as given previously, with the $\phi^*$ replaced by $\phi^n$

The boundary conditions need to be imposed in the computation are defined in Section 3.2.1 . These conditions are applied numerically by redefining the matrix equations in all sweeps at the appropriate grid points on the boundaries and including these new equations with the matrix equation at the other points for the solution.

The surface flow tangency condition, Eq. [3.3.2] , is imposed along the wing mean surface through the [ $\partial\phi^*_{,\zeta} / \partial\xi$ ] term in R at $\xi$ - sweep, and the $L_\zeta$ - operator during the time linearization step in the unsteady computation. The formulation of this boundary condition in the [ $\partial\phi^*_{,\zeta} / \partial\xi$ ] term is derived following the same procedure as described in Section 3.4. Similar procedure also applied in the modification of $L_\zeta$ operator. Since the surface slopes at both time level n and n+1 are known values, the $(\Delta\phi_\zeta)_{k-\frac{1}{2}}$ and $(\Delta\phi_\zeta)_{k+\frac{1}{2}}$ terms in this operator are replaced by :

$$(\Delta\phi_{,\zeta})_{k-\frac{1}{2}} = (f_x^+ + f_t + f_r)^{n+1} + (f_x^+ + f_t + f_r)^n$$

for grid points directly above the wing surface , and

$$(\Delta\phi_{,\zeta})_{k+\frac{1}{2}} = (f_x^- + f_t + f_r)^{n+1} + (f_x^- + f_t + f_r)^n$$

for grid points directly below the wing surface. Bring these known values into the right hand-side of the difference equation, result in a bi-diagonal matrix equations at the boundary points. The wake boundary conditions are imposed within the [ $\partial\phi^*_{,\zeta} / \partial\xi$ ] term in R at $\xi$ - sweep, and the $L_\zeta$ - operator. The inclusion of this

boundary condition in the $[\partial\phi^*_{,\zeta} / \partial\xi]$ term following the same procedure as explained in

Section 3.4 . Similar substitution are made in the $L_\zeta$ operator, by replacing

$$(\Delta\phi_{,\zeta})_{k-\frac{1}{2}} = \frac{1}{\Delta\zeta}\left[\Delta\phi_k - \Delta\phi_{k-1} - (\Gamma^{n+1} - \Gamma^*)\right]$$

for grid points directly above the wing surface, and

$$(\Delta\phi_{,\zeta})_{k+\frac{1}{2}} = \frac{1}{\Delta\zeta}\left[\Delta\phi_{k+1} - \Delta\phi_k - (\Gamma^{n+1} - \Gamma^*)\right]$$

for grid points directly below the wing surface. The upstream, downstream, far - above / below and spanwise conditions are treated in the same ways. The condition at the above far field boundary, for instance, is imposed by applying the following conditions along the boundary line k = kmax ,

$$\left(\frac{\phi_{,\xi}}{\xi_x}\right)_{k+\frac{1}{2}} = \left(\frac{\phi_{,\xi}}{\xi_x}\right)_{k-\frac{1}{2}} - \left(\frac{D}{2\xi_x}\right)\phi_t$$

$$\left(\frac{\Delta\phi_{,\xi}}{\xi_x}\right)_{k+\frac{1}{2}} = \left(\frac{\Delta\phi_{,\xi}}{\xi_x}\right)_{k-\frac{1}{2}} - \left(\frac{D}{2\xi_x}\right)\phi_t$$

The first condition is included in the R term, while the second one is incorporated in the $L_\zeta$ operator.

Since all terms in this scheme are treated implicitly, this scheme does not have a time step restriction. In steady flow calculations, however, it is possible to accelerate the convergence to the steady state solution. This can be achieved by allowing a cyclic variation of variable $\alpha$ ( which contains $\Delta t$ , the time step ). In present study we used a variation according to geometric sequence defined by

$$\alpha^n = \alpha_{max} \left( \frac{\alpha_{min}}{\alpha_{max}} \right)^{(n-1)/(n1-1)}$$

where n = 1,2, ... , n1

n1 is selected between 6 to 8 .

There is no exact rule in choosing the value of n1. In the steady calculation of a F-5 wing configuration, the value of n1 = 7 gave the fastest convergence steady - state solution. Meanwhile, for the 45° swept wing configuration, the fastest convergence are obtained at n1 = 8 .

To demonstrate the accuracy and efficiency of the AF algorithm developed here, calculation are performed for a F-5 wing configuration. The wing has a full span panel aspect ratio of 3.16, panel taper ratio of 0.28, and a leading edge sweep angle of 31.9° . The configuration of the wing is shown in Fig. 3.5.2 . The cross section of the F-5 wing is a modification of NACA65A004 airfoil which has a drooped nose and is symmetric aft at 40% chord. The AF calculation results are compared qualitatively with the results obtained using ADI algorithm as reported in Ref. 74 . The ADI calculation was performed using a modified grid transformation which is similar to the one used in the present study ( described in Section 3.2 ) and the results was presented at four span stations along the wing span. The station were located at $\eta$ = 0.2 , 0.5 , 0.7 and 0.8 semispan length from the wing root.

The results are also compared with the experimental data from an F-5 wing model tested by Tijdeman, Ref. 40 . In the experiments, the steady and unsteady pressure distribution were measured at eight span stations along the wing, which are $\eta$ = 0.18 , 0.36 , 0.51 , 0.64 , 0.72 , 0.82 , 0.88 and 0.98 . Because of the difference in the grid distributions used in the present calculation, no span station has location exactly

the same as the span station used in the experiment as given above. An interpolation of values are used in making the comparison of the results.

In the first case, the calculation was carried out for Mach number = 0.8 and angle of attack of 0° . The coordinate transformation used is as described in Section 3.5.2 , with grid system has 81x41x36 points. Plots of the upper and lower surface steady pressure distribution obtained by present procedure at four span stations are given in Fig. 3.5.3. This results is computed using 125 time steps of the maximum size 0.5 ( the time step is cycled ). Comparison with experimental result are good at all span stations. At the region close to the leading edge, the AF procedure predicts a lower pressure coefficients compare to the experiment results. But compared to the ADI calculation reported in Ref. 74 , this result is much closer to the result from the experiment. Moreover, the converged ADI solution required about 1000 time steps of size 0.01.

Figure 3.5.4 shows the upper and lower surface pressure distribution at Mach number = 0.95. It can be observed from this figure that the shock given by present algorithm is approximately as strong as the one measured in the experiment, but shifted further upward. Since at this Mach number the shock wave is quite strong, this disagreement could be due to the strong shock wave - boundary layer interaction in the flow which changes the shock position on the surface. This strong viscous interaction can not be accurately predicted using simplified viscous model as was done in this study. The viscous ramp model that were used in present study, as described in Section 3.3 , can't be expected to predict the viscous effect precisely in the flow with strong shocks . Contrary to the results from the AF algorithm, the results from ADI solution shows stronger shocks which shifted farther aft. The convergence

history of the steady flow calculation at Mach number = 0.90 is presented in Fig. 3.5.5. The residual ( R ) reaches the value of about $10^{-9}$ and $\Delta\phi_{max} = 10^{-7}$ just in 125 iterations. It can be seen that once the circulation , $\Gamma$ , obtained its converged value, the residual R and $\Delta\phi_{max}$ decrease much faster than their decrease at the beginning of the iteration. Compared with the solution ADI algorithm, this solution is about 8 to 10 times faster.

## 3.6 Generalized aerodynamic forces calculation

As mentioned briefly in the previous section, the solution of the aeroelastic equations can be obtained by integrating the aerodynamic and structural terms simultaneously in time domain. Or, by presenting the equation in frequency domain and solving it as linearized eigenvalue problem. In the first approach, the interaction between the flow and the structure occurs through the surface boundary conditions. At every time step, a new surface boundary conditions are employed in the flow solution according to the surface displacements.

In the frequency domain solution, however, no such direct interaction happen. The compatibility between the structural motion and the aerodynamic forces comes indirectly through the parameter k , the reduced frequency of the motion. In conventional U - g flutter analysis, the solution is carried out in k - plane and in the root - locus method it is carried out in the s - plane. So, in both of these methods the aerodynamic forces as function of the reduced frequency or Laplace variable, s, are needed.

Two methods are used in this study to compute the aerodynamic load for flutter analysis in frequency domain, which will be described in the next two sections.

### *3.6.1 Harmonic oscillation method*

The harmonic oscillation method assumes that the disturbance velocity potential for some sinusoidal body motion of frequency $\omega$ can be expressed in an infinite series as, Ref. 20 ,

$$\phi(x,y,t) = \phi_0(x,y) + \varepsilon\,\phi_1(x,y)\,e^{i\omega t} + \varepsilon^2\,\phi_2(x,y)\,e^{2i\omega t} + \ldots$$

where $\varepsilon$ is related to the amplitude of the body motion. For purely subsonic and supersonic flows, the aerodynamic response induced by sinusoidal motion is also sinusoidal at the same frequency, so the higher terms in $\phi$ are zero. But in transonic flows, this is not true because the nonlinearity of the flow equation produces the higher order terms in the responses. However, for a small amplitude motion, i.e. for $\varepsilon << 1$ , the terms of order $\varepsilon^2$ or higher can still be ignored.
But $\phi_1$ (x,y) now depends on the mean steady - state solution, $\phi_0$ . In other words, the flow is assumed to be a linear perturbation about nonlinear mean steady-state conditions.

The aerodynamic forces, then, are obtained by calculating the aerodynamic responses ( in term of the total lifting pressure , $\Delta p$ , or the lift and moment coefficients , $C_l$ and $C_m$ ) of several cycles of a harmonically forced oscillation at each structural mode. The determination of the forces is based on the last cycle of the oscillation.

With this method, the flow field calculations are performed for each combination of the flow Mach number, structure modes and reduced frequency of interest.

For a two-dimensional, two degree-of-freedom typical section model, the calculation of the aerodynamic forces using this method is still affordable. But for three-dimensional wing model, where 3 or more structural modes are usually used for the aeroelastic calculation and the calculations must be performed at a wide range of reduced frequencies, this method is not efficient. A more efficient method, called 'pulse transfer function method' which is described in the next section, is applied.

The harmonic oscillation method is used to calculate the generalized aerodynamic forces ( lift and moment coefficients ) of two-dimensional typical section model having a NACA64A006 cross section ( see Fig. 2.1.1 ) . The airfoil is given a sinusoidal pitching motion with respect to the elastic point located at quarter chord aft from the leading edge,

$$\alpha(t) = \alpha_0 \sin(\omega t)$$

The flow field calculation was carried out using the ADI algorithm, for free-stream Mach number = 0.875 , reduced frequency = 0.4680 , at pitching amplitude $\alpha_0 = 1°$ . The flow equation are integrated for 6 full cycles, with 120 time steps for each cycle ( which is associated with $\Delta(\omega t) = 3°$ ) .

Figure 3.6.1 shows the aerodynamic response of the airfoil due to the sinusoidal pitching motion in term of the total lift and moment coefficients with respect to the elastic point. It can be observed that both the lift and moment coefficients becomes harmonic after about 4 cycles of motion. From several calculations it was found that the number of cycles needed for the aerodynamic response to become harmonic depends on the reduced frequency of the motion, k , the pitching amplitude, $\alpha_0$ , and

the free-stream Mach number , M. For higher values of reduced frequency ( approximately for k > 0.3 ), more cycles are needed to obtained periodic response ( between 4 to 5 cycles ) and at lower values of k only 2 - 3 cycles is required. The reason for this is that at higher values of k ( which means stronger unsteadyness in the flow ) , a strong transient aerodynamic response is found in the flow which take a longer time to die out. A similar pattern is also observed in the case of the effect of pitching amplitude. The larger the values of $\alpha_0$ , the longer time it takes for the aerodynamic response to be periodic because of stronger disturbance exist in the flow field. The dependency of the number of cycles on the free-stream Mach number is not as strong as in the two parameters described above. This could be due to the fact that the dependency with the Mach number are more closely related to the change in the flow structure at different values of Mach number ( such as the shock strength and position ) . Since the flow structure over NACA64A006 airfoil section is only slightly change over the computed Mach number range ( from M = 0.80 to M = 0.90 ), periodic response is also expected to be obtained after approximately the same number of cycles.

Note the phase difference between the lift coefficient and the moment coefficient with respect to the airfoil motion. When the periodic response has been already achieved, these two phase shifts are almost equal and its values depend on the reduced frequency of the motion, as shown in Fig. 3.6.2 . As the reduced frequency increases, the phase shift also increases. The increase at higher values of reduced frequency ( k > 0.3 ) is slower compare to its increase at lower values. From the computation at two different free-stream Mach number, M = 0.80 and M = 0.85 , it was found that the phase shift of the lift and moment coefficients are not strongly affected by the free-stream Mach number. This fact is also observed in the investigation performed by Ballhaus and Goorjian as reported in Ref. 84 .

The value of the lift and moment coefficient are

$$|C_l| = C_l' / \alpha_0 \sin(\omega t - \psi_l)$$

$$|C_m| = C_m' / \alpha_0 \sin(\omega t - \psi_m)$$

where $C_l'$ and $C_m'$ are the aerodynamic lift and moment coefficient response, respectively, and $\psi_l$ and $\psi_m$ are the phase shift of the lift and moment coefficients relative the airfoil motion, respectively.

Figure 3.6.3 shows the lift coefficients as function of reduced frequency. It is clear from the results shown here and in Fig. 3.6.2 that the effect of increasing frequency on the lift coefficients ( as well as moment coefficients ) is to decrease their amplitude/value and increase their phase shift relative to the airfoil motion. The comparison between the lift coefficients obtained from the present calculation with the results from LTRAN2 , Ref. 84 , is presented in Fig. 3.6.4 . In LTRAN2 code the calculation of the lift and moment coefficients were carried out using the indicial method. In this method, the indicial response at each motion mode is computed. The indicial response is the flow field response to a step change in the given mode of motion. From the indicial response, the solution for any arbitrary frequency of that motion can be obtained with the aid of the Duhamel integral. This approach ( which is similar to the pulse transfer function method that will be discussed in the next section ) has the advantage that solutions for all reduced frequencies for each combination of the mode of motion and free-stream Mach number can be obtained from a single flow field computation. From Fig. 3.6.4 it can be observed that present results compare well with the previous results. The discrepancy in the two results may be due to two reasons. The first one is due to the low frequency approximation applied in LTRAN2 solution which limit its application only for flow with reduced frequency less than 0.2 . The second reason is due to the consideration that have to

be made in computing the indicial response for transonic flow. This consideration is that the amplitude of the step change in the motion should be sufficiently small that the shock waves locations remained essentially fixed and the superposition principle is still valid. For the NACA64A006 airfoil considered, a very small step change is required , such as $\alpha_0 = 0.1°$ was used in the calculation using the indicial method reported in Ref. 84 , in order the above consideration to be fulfilled. On the other hand, in the present calculation, using the harmonic oscillation method, it was necessary to use a value of amplitude of pitching motion of 1° , in order to obtained an accurate response. It was found very difficult to obtain periodic response for amplitude less than 0.5° . Since the flow response, as mentioned earlier, is amplitude dependent, this large amplitude difference should be considered as a major contributor to the difference observed for the lift and moment coefficients.

### *3.6.2 The pulse transfer function method*

The pulse transfer function method was used for two-dimensional transonic aeroelastic problems by Bland and Edwards, Ref. 87. We have extended this approach to three-dimensional problems. For the three-dimensional model, the calculation of the generalized aerodynamic force for flutter calculation using the harmonic oscillation method becomes expensive because for each combination of reduced frequency, mode of motion and free-stream Mach number, a complete flow field computation is required. In the pulse transfer function method, the aerodynamic forces for each combination of the structural mode and Mach number in a wide range of reduced frequency are obtained in a single flow field calculation. The aerodynamic

forces are computed indirectly from the aerodynamic response due to a smoothly varying exponentially shaped pulse, as shown in Fig. 3.6.5 . This method is a modification of the indicial method , briefly mentioned in the previous section, in which a step - displacement is replaced by an exponentially shaped pulse. The advantage of using the pulse input is to avoid the non-physical transients that was found when using the step function input in indicial method with ADI solution for the TSD equation in which the second-order time derivative included, Ref. 85 . The non-physical transient is due to the approximation of the infinite intial derivative using the finite time step taken.

The pulse is expressed as

$$q(t) = q_0 e^{-a(t-t_0)^2}$$

Where $q_0$ is the amplitude of the pulse , a and $t_0$ are constants related to the width and center of the pulse.

The deformation Z of any points (x,y) on the structure surface at any time t is determined by the product of the the pulse and the structure mode, z(x,y) , and may be written as follows

$$Z(x,y,t) = q_0 e^{-a(t-t_0)^2} z(x,y) \qquad [3.6.1]$$

This deformation is applied to the structure and the aerodynamic transients response ( which may be expressed in term of the total lifting pressure at point (x,y) on the surface , $\Delta p$ (x,y) ) are computed. By using a Fast Fourier Transform ( FFT ) analysis, both the response and the input pulse are transformed into reduced frequency, k , domain. The aerodynamic forces is defined as the ratio between the FFT of the transient response divided by the FFT of the deformation,

$$Q(k) = \frac{\text{FFT of the aerodynamic response}}{\text{FFT of the deformation}}$$

Specifically, if Q represents the total lifting pressure $\Delta p_j$ (x,y) , which is the total pressure at point (x,y) induced by the displacement in the j-th structural mode, then in k - plane it can be written as

$$\Delta p_j(x,y,k) = \frac{\text{FFT}\,[\,\Delta p_j(x,y,t)\,]}{\text{FFT}\,[\,L(t)\,.\,z_j(x,y)\,]}$$

$$\text{and} \quad \Delta p_j(x,y,t) = \bar{q}\,[\,C_p^+(x,y,t) - C_p^-(x,y,t)\,]$$

where $z_j(x,y)$ is the j-th structural mode. Once these quantities are computed, the generalized aerodynamic forces , $A_{ij}$ , for the aeroelastic solution are obtained by substituting these values into the Eq. [2.2.2] .

In a three-dimensional wing model, for the purpose of the compatibility between the structure and aerodynamic terms in the derivation of the aeroelastic equation of motion ( see Section 2.2 ), z(x,y) are selected as the mode shapes of the wing, $h_j(x,y)$. In this study, the values of a and $t_0$ in Eq. [3.6.1] are selected to be equal to 0.25 and 17.5 $\Delta t$ , respectively, where $\Delta t$ is the non-dimensional time step. It is important to note that the transient response has to be calculated for a time interval that is long enough such that the final value of the response becomes steady and equal to its initial value. Otherwise, the Fourier transform of the response will not be accurate. A calculation for 1024 time steps with the $\Delta t = 5\pi/48$ is used, which is found to be accurate and gave a stable response.

This method was used to calculate the generalized aerodynamic forces for the flutter calculations of a 45° swept wing. This wing is a semispan wind - tunnel wall - mounted model that has a quarter chord sweep angle of 45° ( leading edge sweep angle of 46.3° ), a panel aspect ratio of 1.6525 and panel taper ratio of 0.66 . This series of wings was tested in the Transonic Dynamic Tunnel ( TDT ) at NASA Langley Research Center, Ref. 13 , and is an AGARD standard three-dimensional configuration, Ref. 86 . A plan view of the wing is shown in Fig. 5.5.1. The wing has a NACA64A004 airfoil section and was constructed of laminated mahogany. In order to obtain flutter for a wide range of free-stream Mach numbers and mass density ratio in the TDT, some of the wings had holes drilled through the wing to reduce the stiffness, and filled with a rigid plastic foam to maintain the airfoil shape. The wing model that is used in present study is the one that denoted as WEAK3 model. Figure 5.5.2 shows oblique projections for the four natural modes and its displacement contour used to model wing WEAK3 structurally. These modes which are numbered 1 through 4 represent the wing first bending, first torsion, second bending and second torsion mode, respectively. The natural frequencies range from 9.60 Hz for the first bending mode to 98.50 Hz for the second torsion mode.

The flow field calculation is performed in the computational domain with 90x20x40 grid points which are distributed following the coordinate transformation given in Section 3.2 , and shown in Figs. 3.2.5a and 3.2.5b . The impulse response calculation are calculated using the AF algorithm and are initiated with the steady flow solution as the first estimate of the potential values. The steady upper surface pressure distribution for mean angle of attack 0° at the span section located 0.2 semispan length from the wing root is presented in Fig. 3.6.6 . At Mach number range from 0.499 to

0.954 the flow field is generally free of shocks, except at Mach number equal to 0.954 a weak shock was observed at two span sections at the wing tip region.

Figure 3.6.7 shows the total-lift pressure response, $\Delta p_j$ , at the grid point located at the wing tip, one half chord length from the leading edge, induced by the displacement in the second mode ( first torsion mode ), at Mach number M = 0.90. The wing is given a displacement according to Eq. 3.6.1 with z(x,y) replaced by the displacement of the wing second natural mode. The pulse amplitude, $q_0$ , is taken to be equal to 0.00215 which associated with the deflection of 1% of chord length at the wing tip. The response becomes steady, returning to its initial value very quickly in 60 - 100 time steps after the wing returning to its steady position. Since at this Mach number, the entire flow field is free of shocks so that the flow is not highly nonlinear, a quick converged response can be expected. When the amplitude of the pulse, $q_0$ , is doubled, the wing motion gave a diverged aerodynamic response ( the response did not come back to its initial value after about 1024 time steps ). So, the amplitude of the pulse should be chosen in such a way that it is not so large which might give a diverged response, but also it is not so small that the response become inaccurate. For calculations reported in Ref. 87, the pulse amplitude was selected such that the maximum angle of attack is equal to 1° . In general, the selection of the $q_0$ value is dependent on the geometry of the wing and also the characteristic of the flow.

After the Fourier transformation of this response, the generalized aerodynamic force is obtained through the integration of Eq. [2.2.2] . The value of $A_{12}$ , the generalized aerodynamic coefficients induced by the second natural mode and acting through the first mode , is given in Fig. 3.6.8 as a function of reduced frequency. The comparison was made with the results computed using the harmonic oscillation method. Results

from harmonic method were obtained for 7 values of reduced frequency, ranging from k = 0.0 to 0.9 with increment of 0.15 . The two set of results are in very good agreement, which validates the pulse transfer - function analysis for application to transonic flow problem. The same agreement for the $A_{22}$ coefficient is shown in Fig. 3.6.9.

Using this method, the number of flow field calculation needed to compute all of the elements in the generalized aerodynamic forces matrix, at a certain value of M , is the same as the number of the structural modes being used in the aeroelastic calculation. In the harmonic oscillation method, this number will be equal to the number of the structural modes multiplied by the number of reduced frequencies of interest.

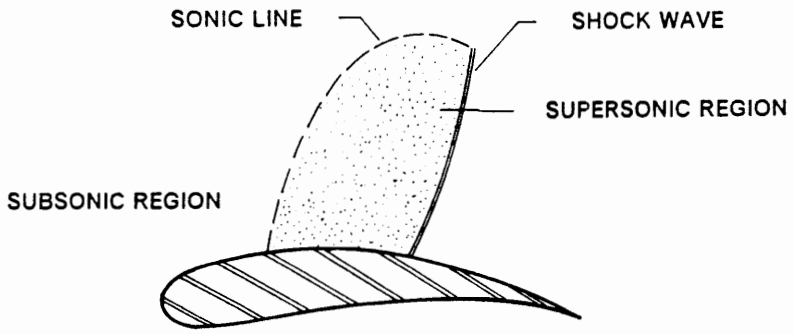


Figure 3.1.1 Typical structure of a transonic flow over lifting body with subsonic free-stream Mach number.

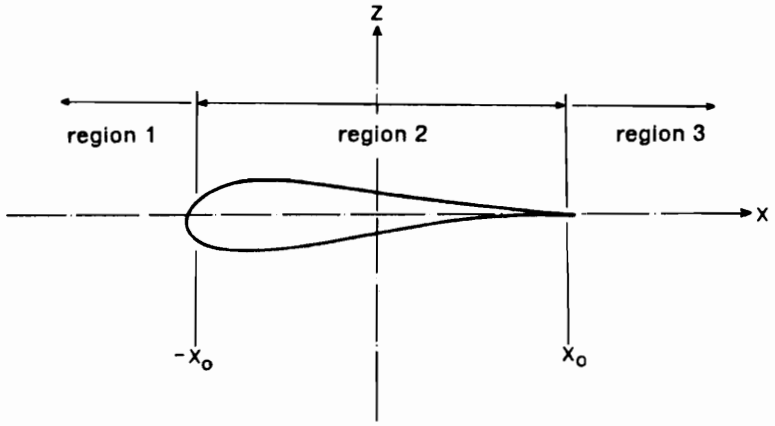


Figure 3.2.1 Regions in airfoil section for coordinate transformation.

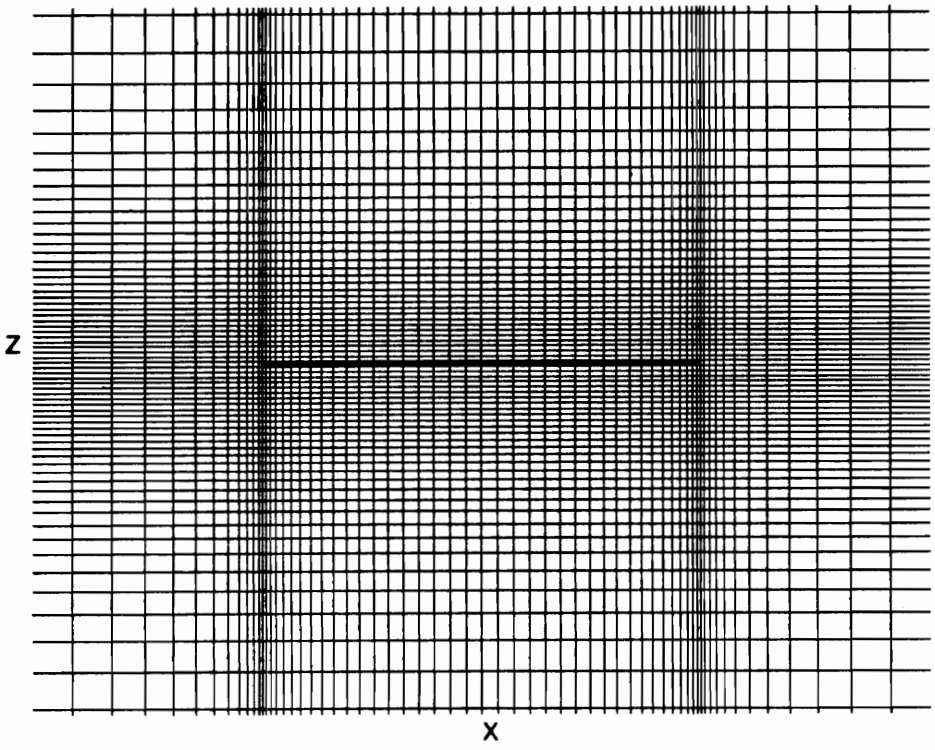


Figure 3.2.2 Grid-system in physical plane for two-dimensional flow calculations based on TSD equation.

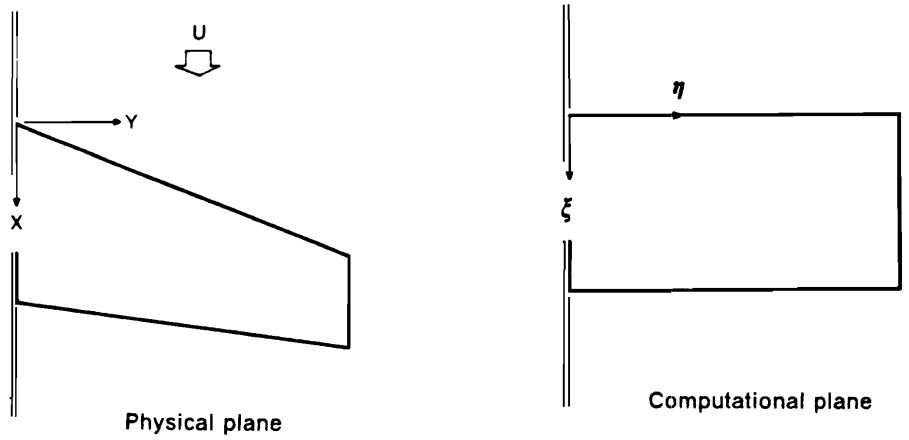


Figure 3.2.3 Physical and computational plane of tapered wing geometry.

a) chordwise variation

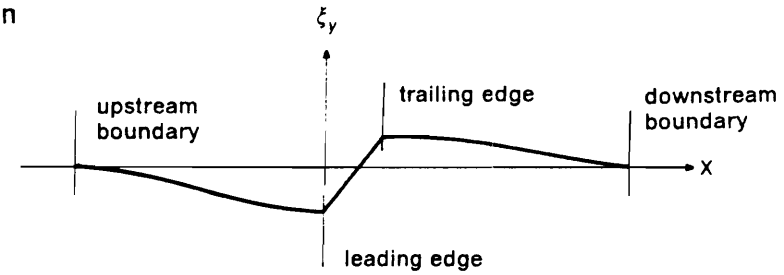


b) spanwise variation

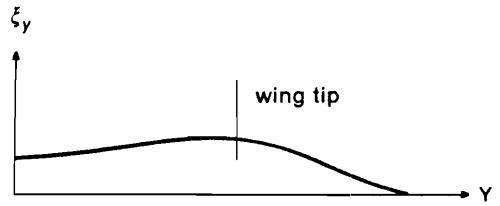


Figure 3.2.4 The metric $\xi_y$ - variations, a) chordwise variation along span-section at the wing root, y = 0 ; and
b) spanwise variation along gridline at the leading edge.

a) gridlines distribution in x-y plane

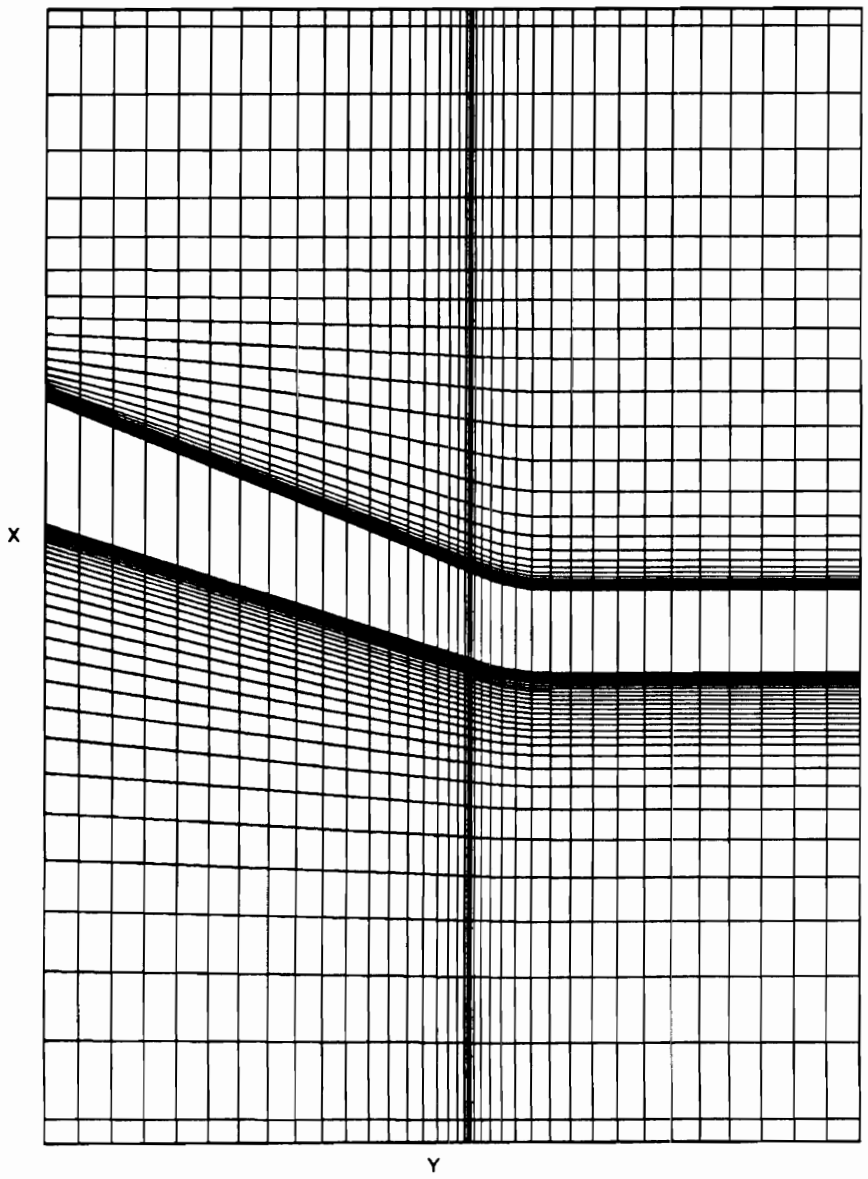


Figure 3.2.5 Gridlines distribution for three-dimensional flow calculations over 45° swept wing, a) gridlines distribution in x-y plane ; and b) gridlines distribution in x-z plane.

b) gridlines distribution in x-z plane

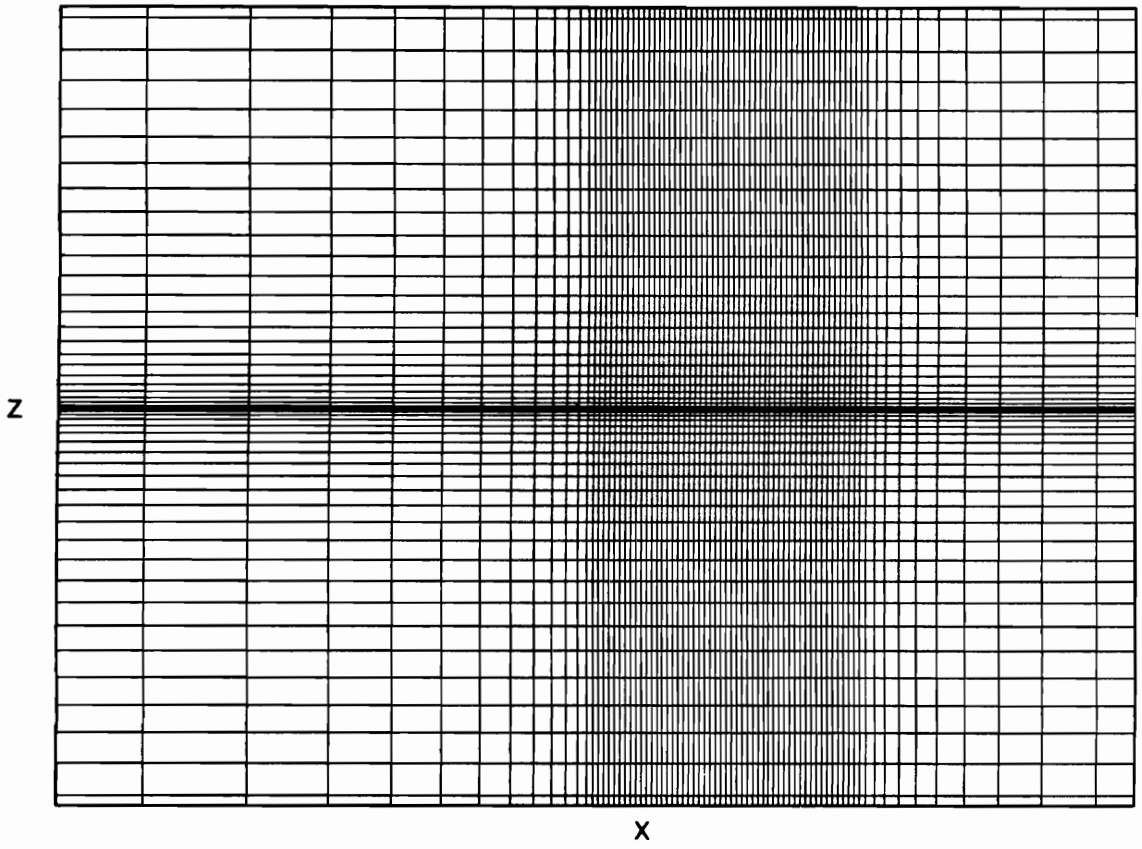


Figure 3.2.5 Concluded

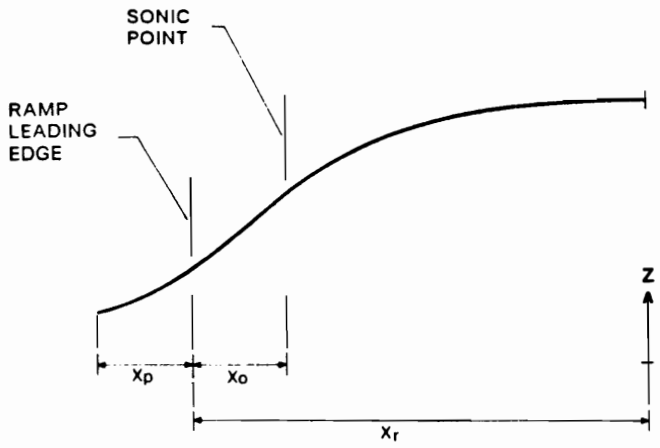


Figure 3.3.1 Viscous ramp geometry used to model the viscous effect in flow calculation based on inviscid flow equation.

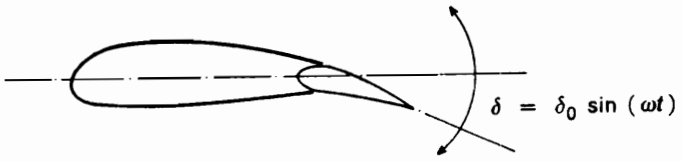


Figure 3.4.1 NACA64A006 airfoil section with sinusoidaly oscillating trailing edge flap of length 0.25 chords.

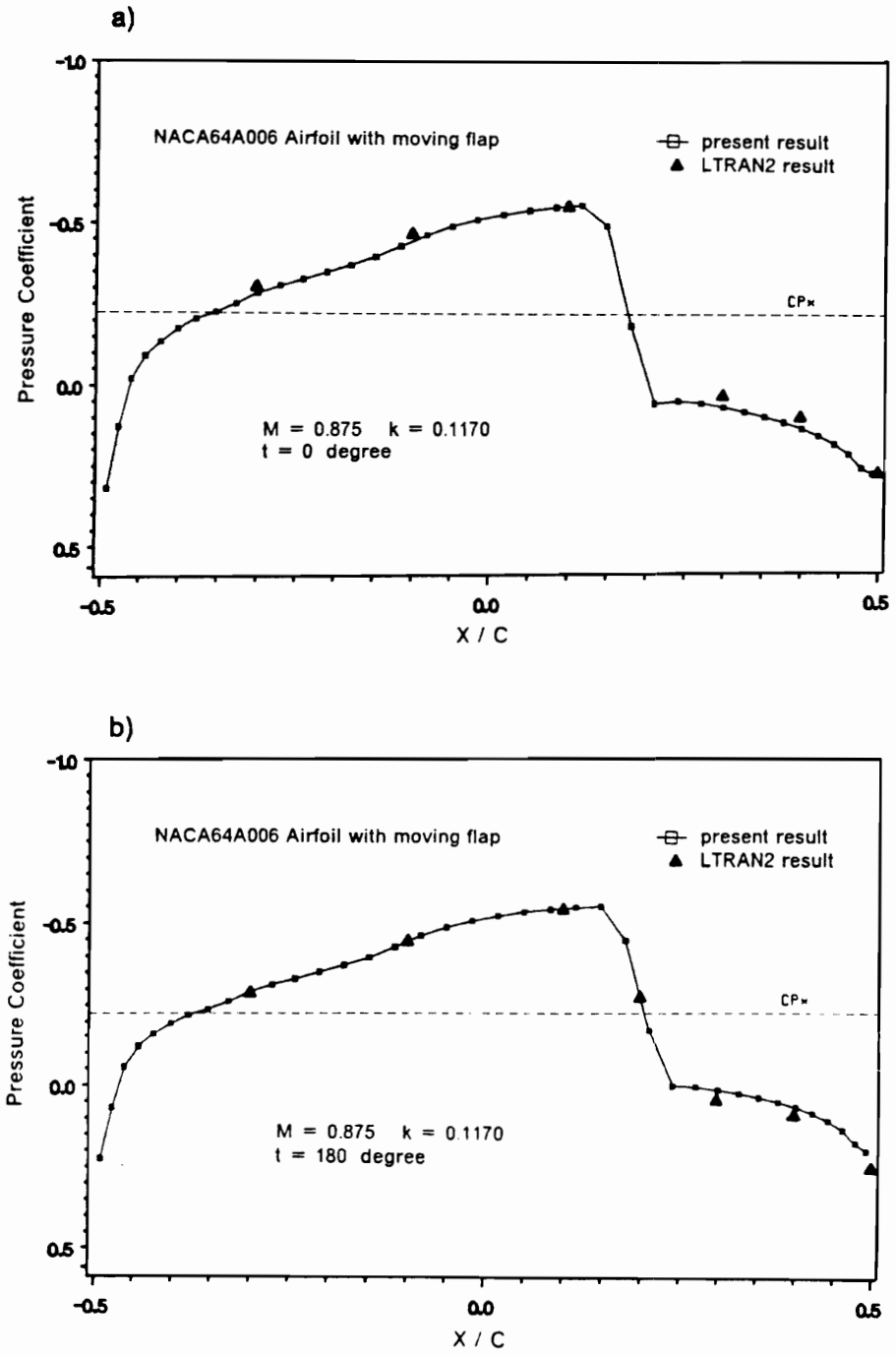


Figure 3.4.2 Unsteady upper surface pressure distribution of NACA64A006 airfoil section induced by oscillating trailing edge at M = 0.875 and k = 0.1170 , a) at time t = 0° , and b) at time t = 180° .

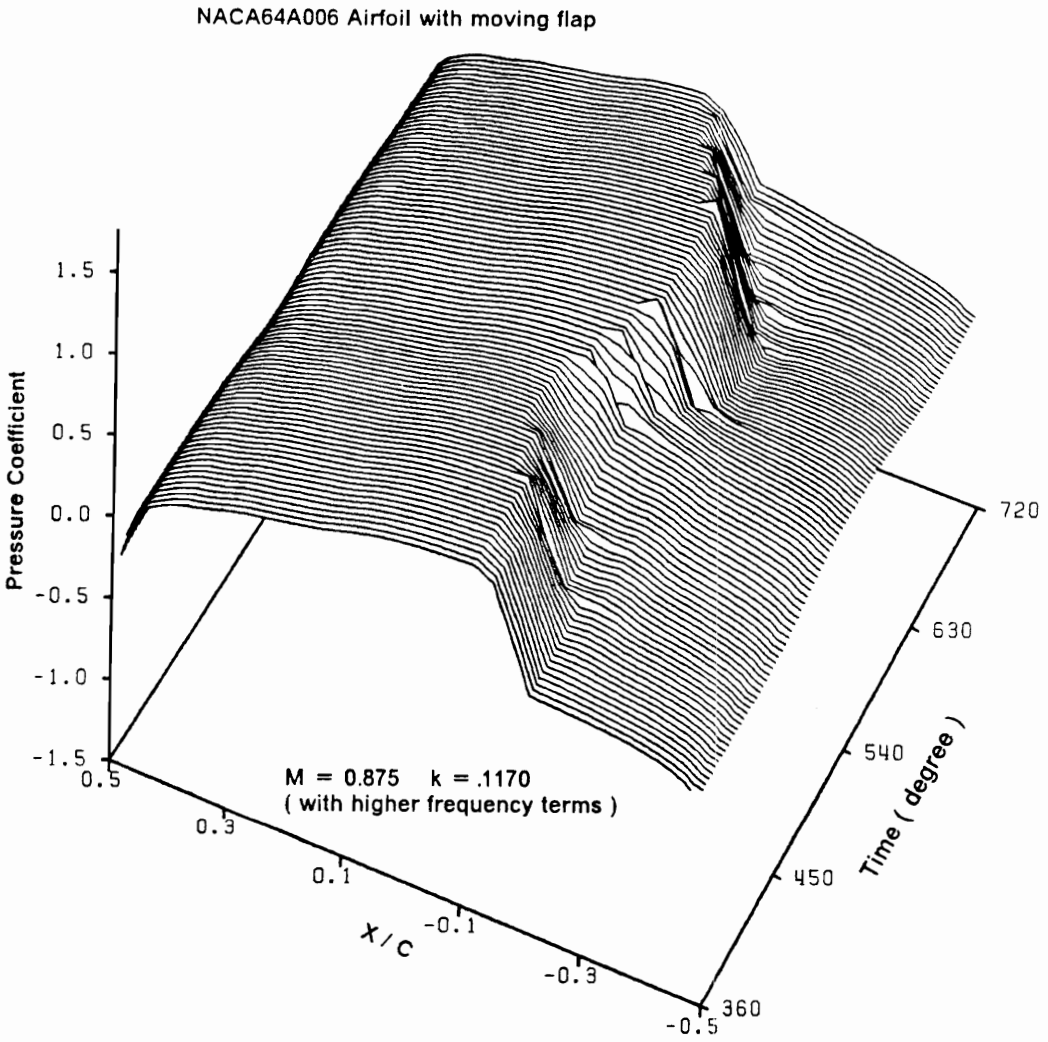


Figure 3.4.3 The time history of the upper surface pressure distribution of NACA64A006 airfoil section induced by oscillating trailing edge flap, obtained using general-frequency TSD equation.

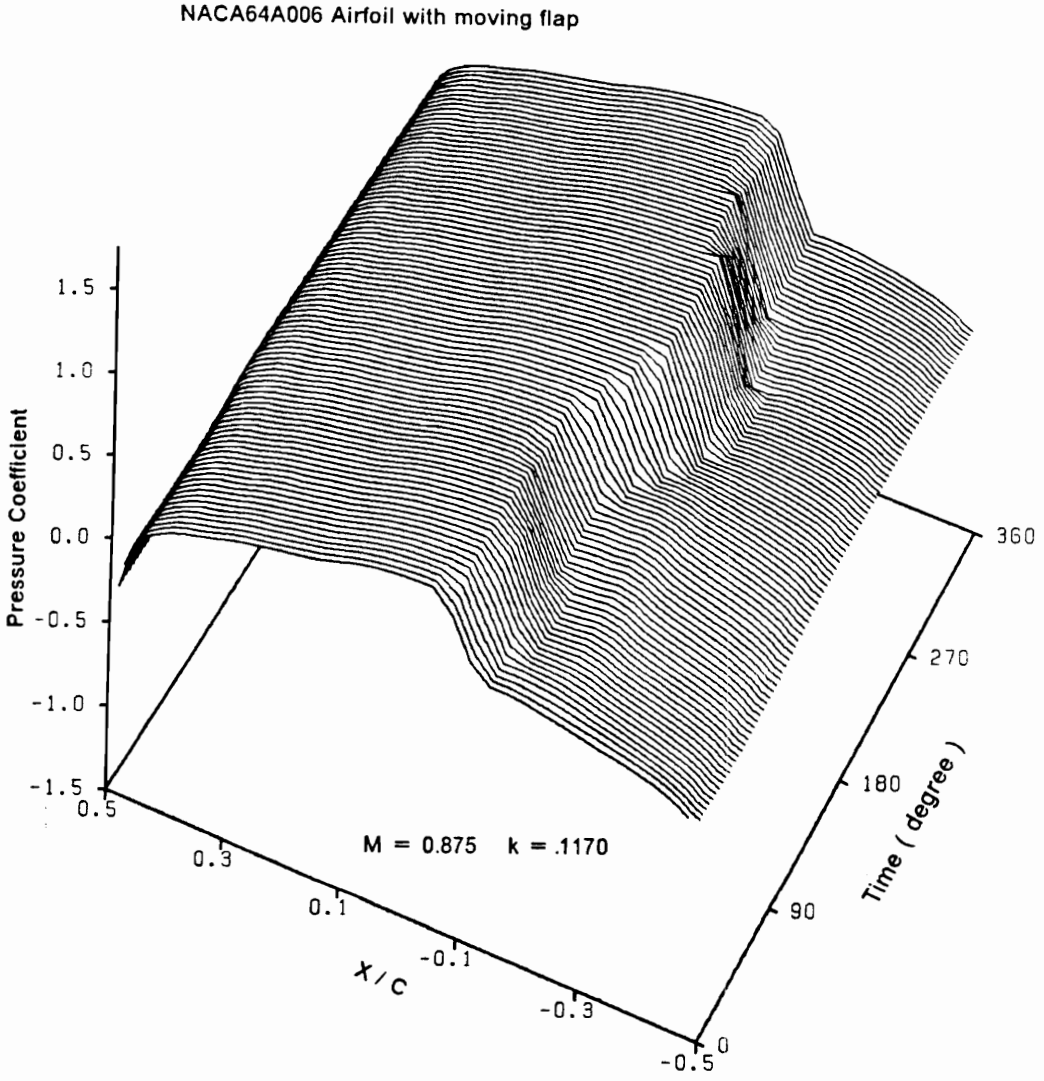


Figure 3.4.4 The time history of the upper surface pressure distribution of NACA64A006 airfoil section induced by oscillating trailing edge flap, obtained using low-frequency TSD equation.

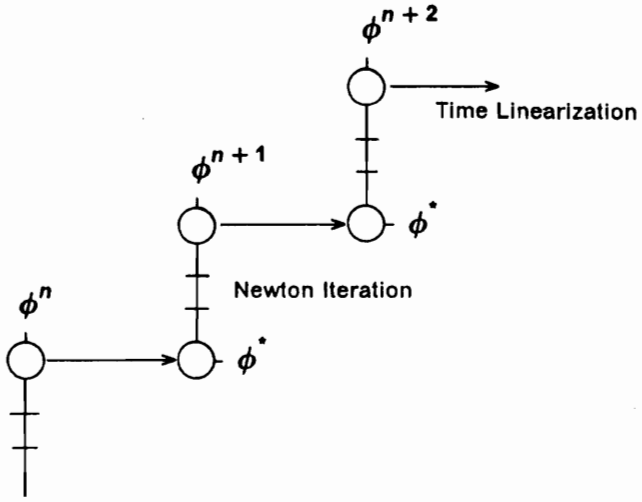


Figure 3.5.1 An approximate factorization (AF) algorithm for unsteady flow calculations, consists of i) a time linearization step and ii) Newton iteration.

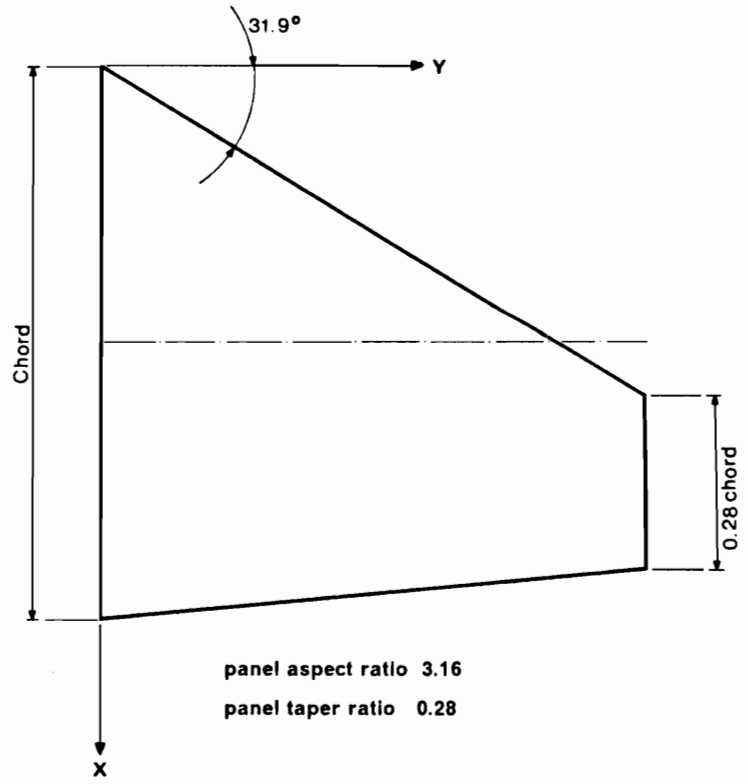


Figure 3.5.2 F-5 wing configuration with a modified NACA65A004 airfoil cross-section.

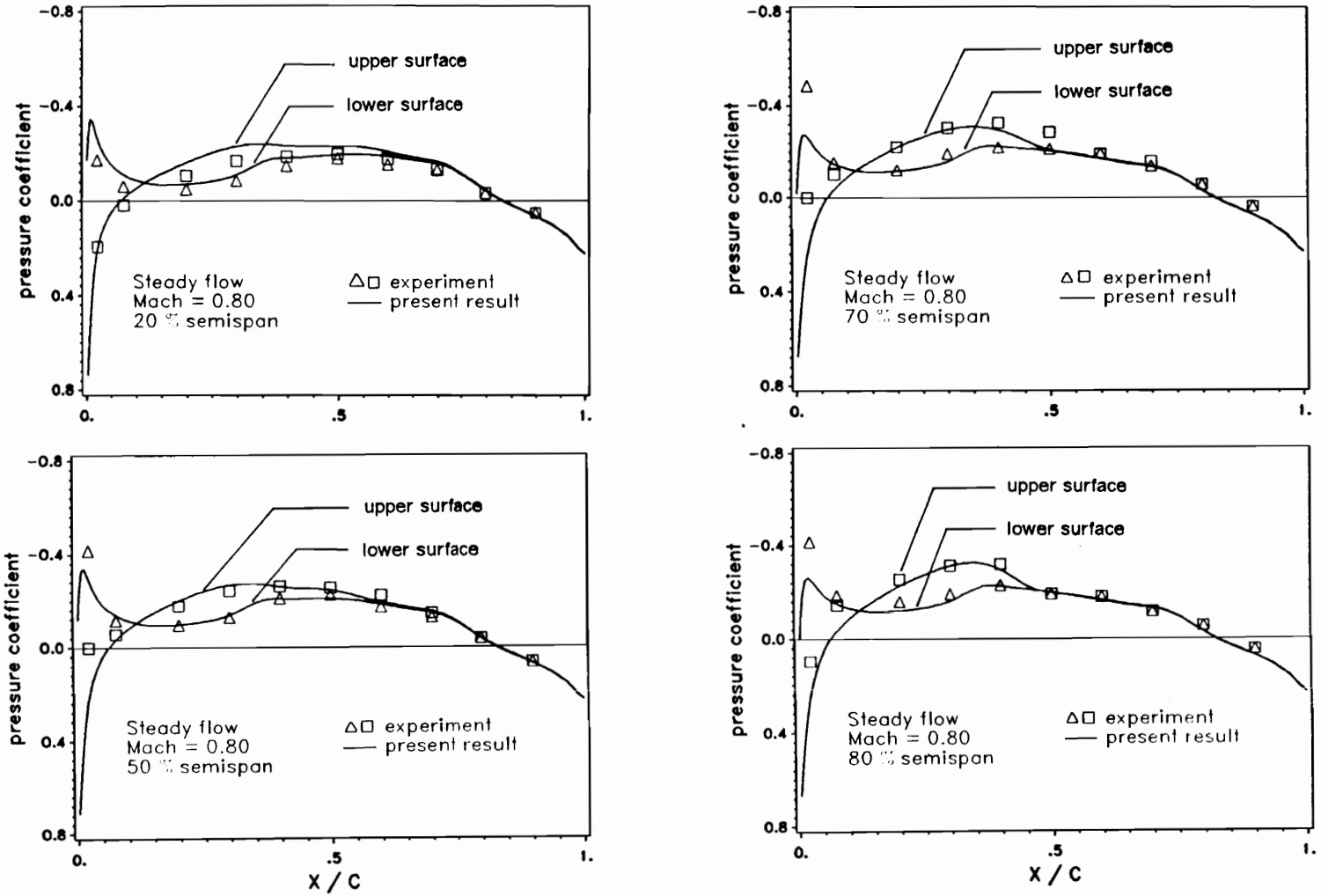


Figure 3.5.3 Comparison of calculated and measured streamwise steady pressure distribution for F-5 wing at four span-sections, M = 0.80 and $\alpha_0 = 0°$ .

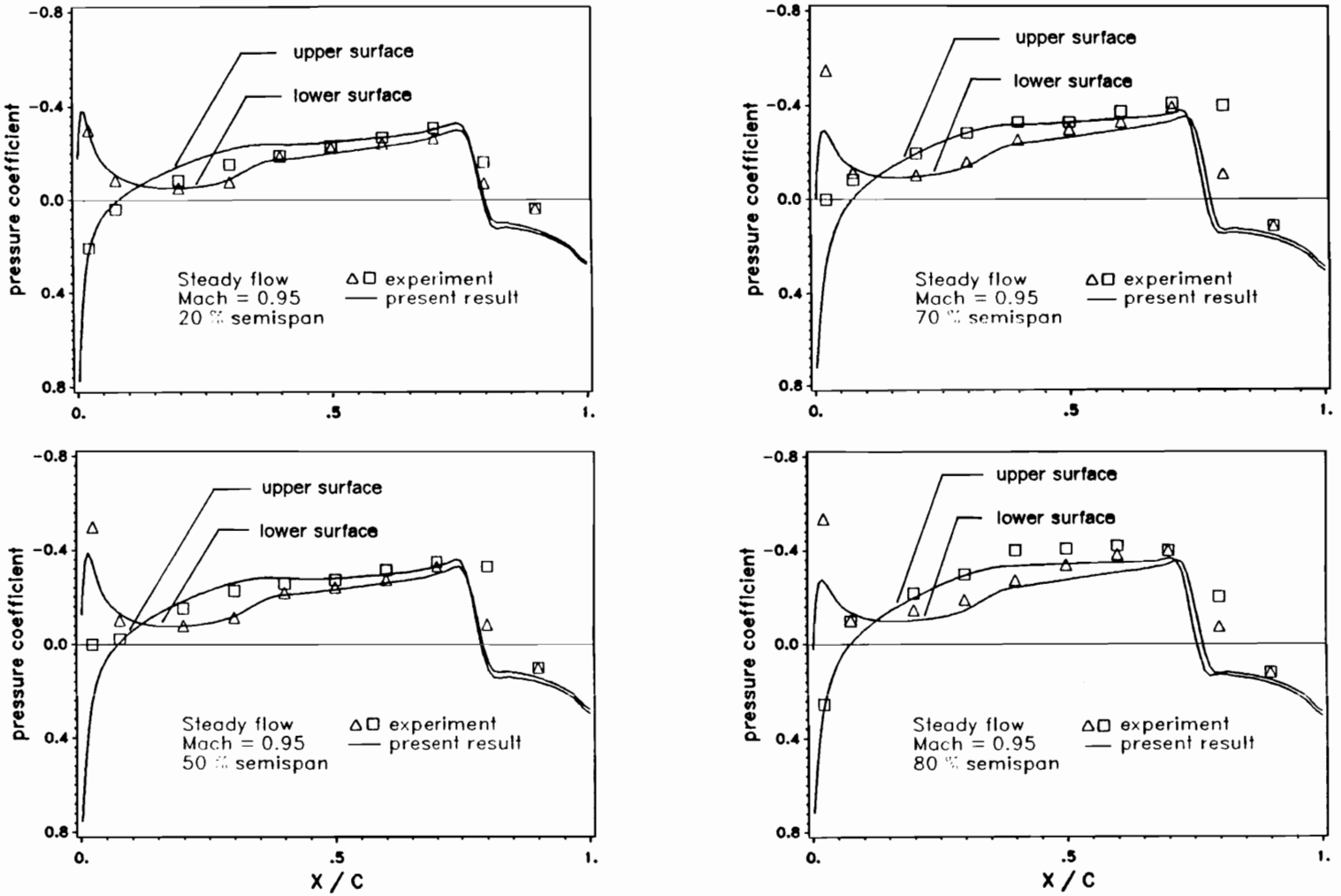


Figure 3.5.4 Comparison of calculated and measured streamwise steady pressure distribution for F-5 wing at four span-sections, M = 0.95 and $\alpha_0 = 0°$ .

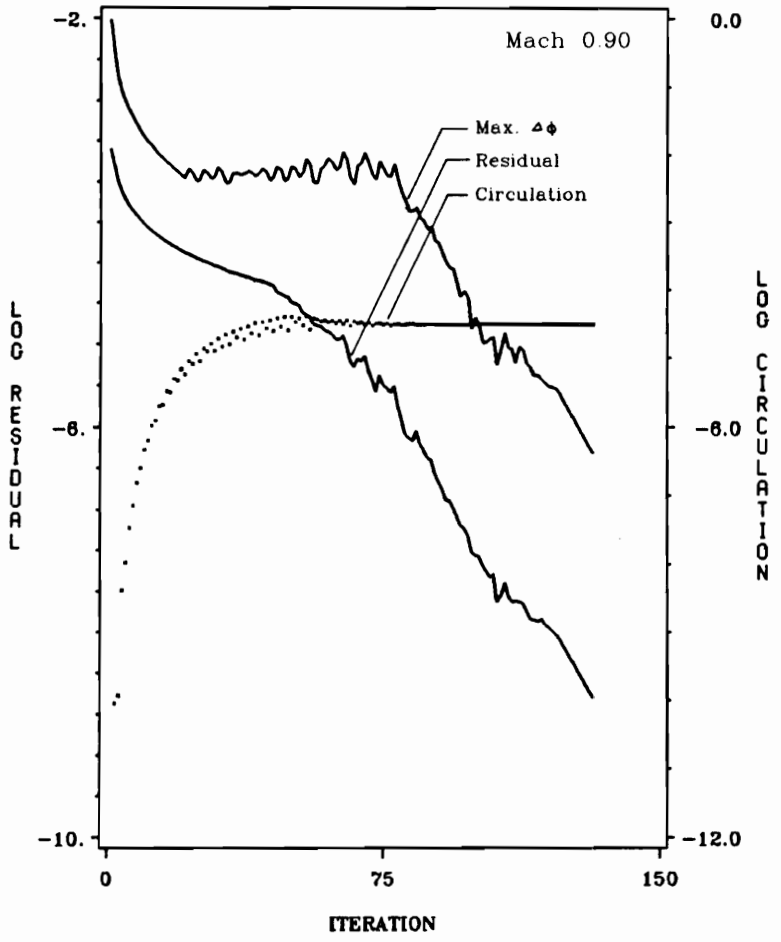


Figure 3.5.5 The convergence history of steady flow calculation over F-5 wing configuration using AF algorithm, M = 0.90 and $\alpha = 0°$ .

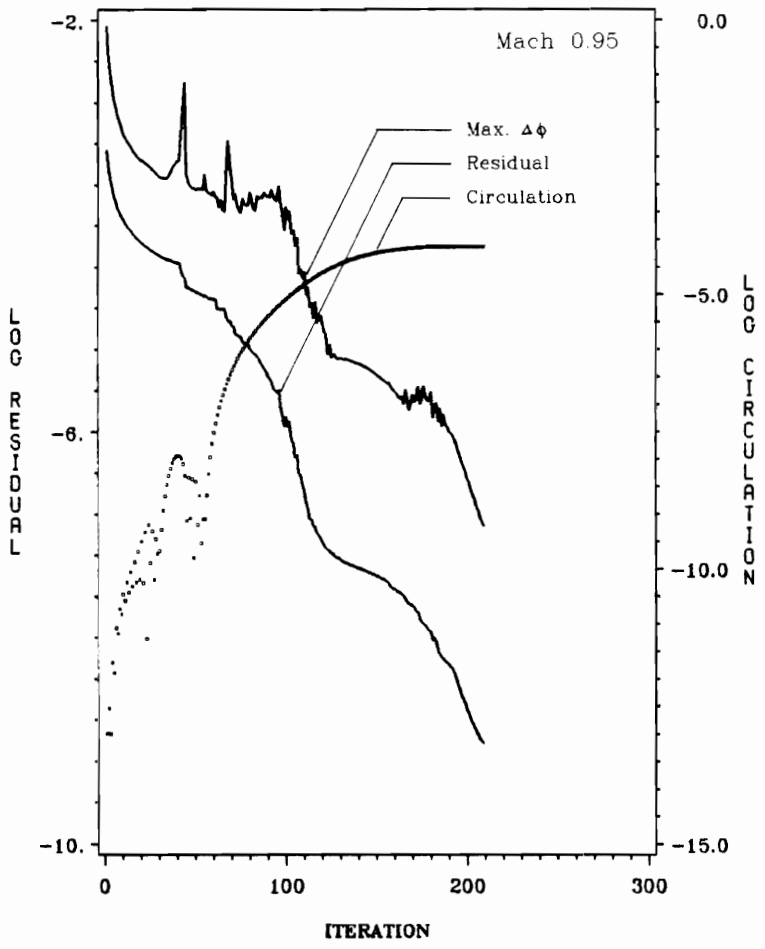


Figure 3.5.6 The convergence history of steady flow calculation over F-5 wing configuration using AF algorithm, M = 0.95 and $\alpha = 0°$ .

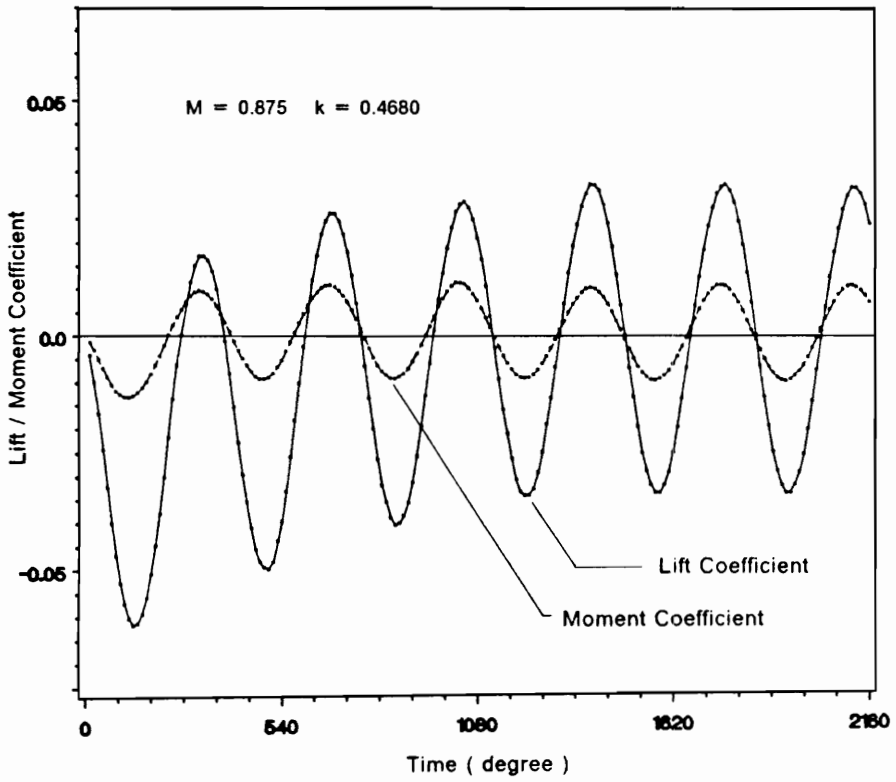


Figure 3.6.1 Aerodynamic response of NACA64A006 Airfoil section due to sinusoidal pitching motion about elastic axis located a quarter chord aft from leading edge, M = 0.875, pitching amplitude = 1° .

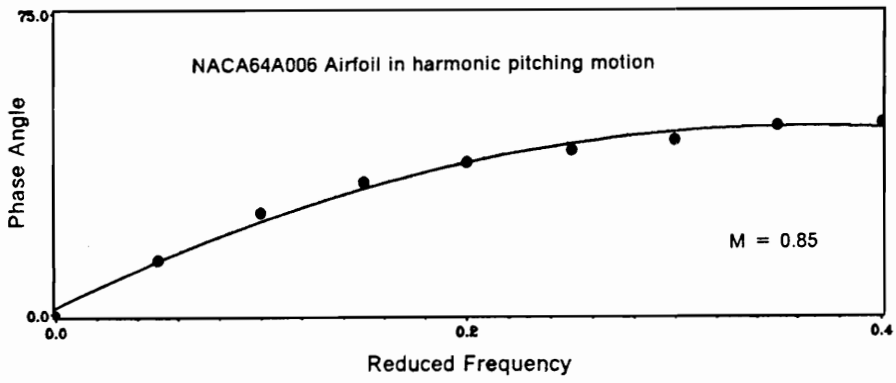


Figure 3.6.2 Variation of the phase angle, between lift force and pitching motion, with reduced frequency of the motion for NACA64A006 airfoil section.

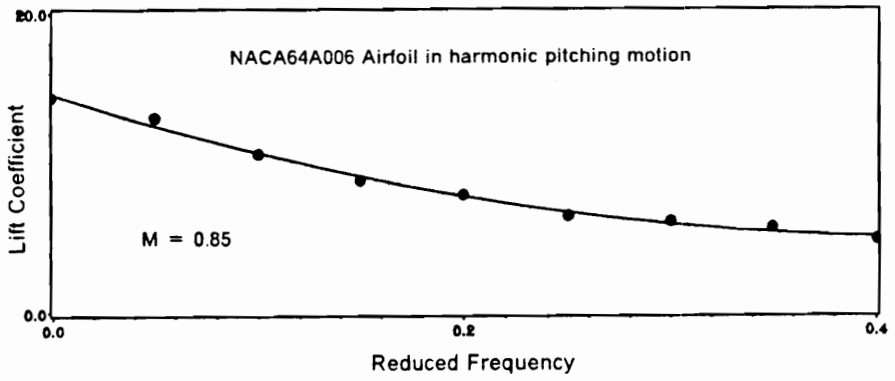


Figure 3.6.3 Variation of lift coefficients with reduced frequency of the motion for NACA64A006 airfoil having sinusoidal pitching motion.

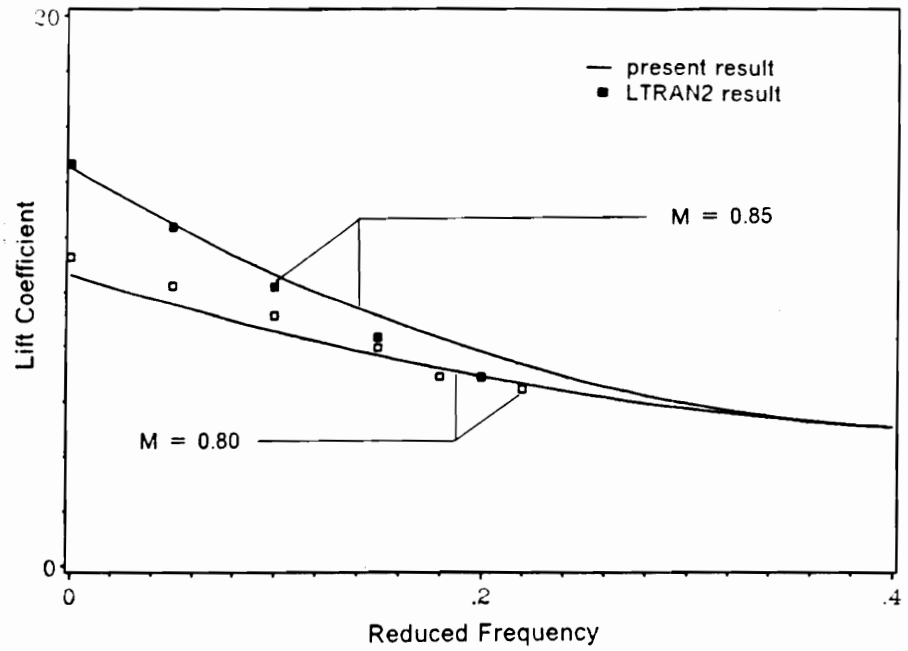


Figure 3.6.4 Comparison between litf coefficients obtained using harmonic oscillation method ( present results ) and using indicial method ( LTRAN2 solution ) at M = 0.80 and 0.85.

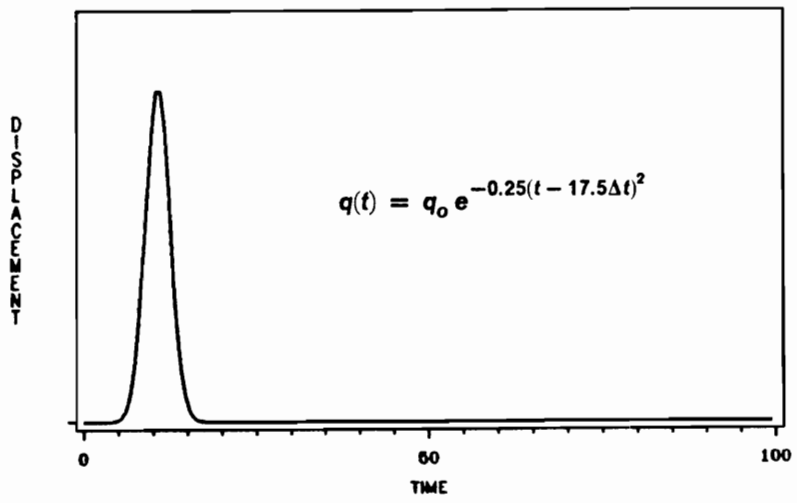


Figure 3.6.5 Smoothly varying exponentially shaped pulse used in the pulse transfer function method.

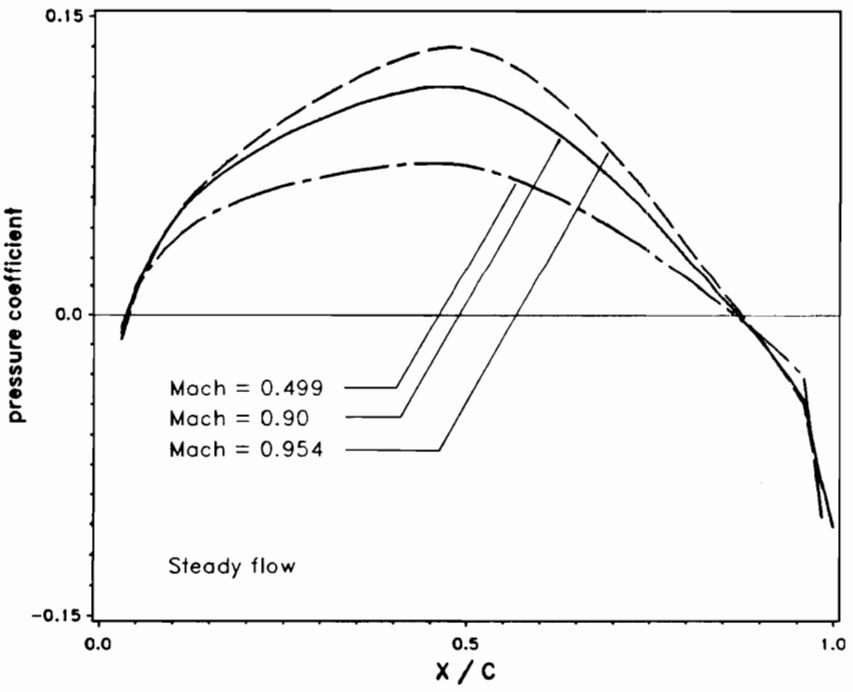


Figure 3.6.6 Steady upper surface pressure distribution over 45° swept wing at span-section located 0.2 semispan length from the root $\alpha_0 = 0$

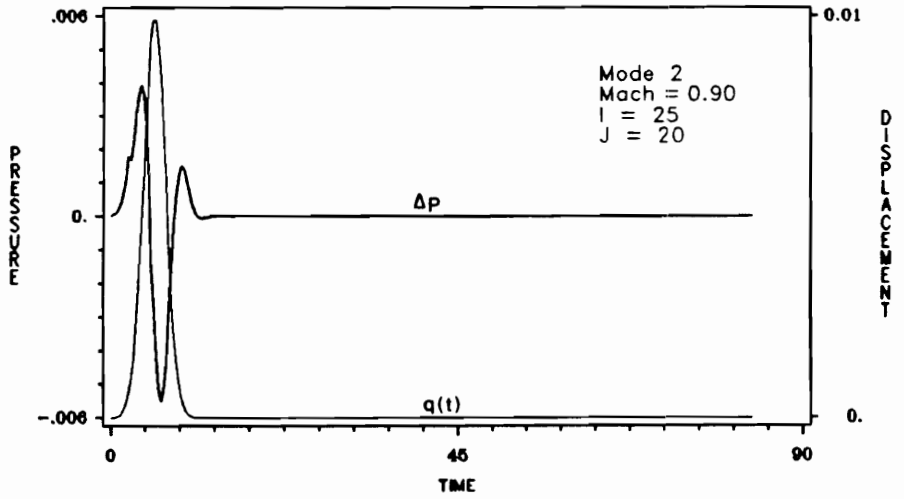


Figure 3.6.7 The total aerodynamic lift force reponse $\Delta p$ at the wingtip mid-section, induced by the displacement in the second mode ( first torsional mode ) of the wing, M = 0.90 .

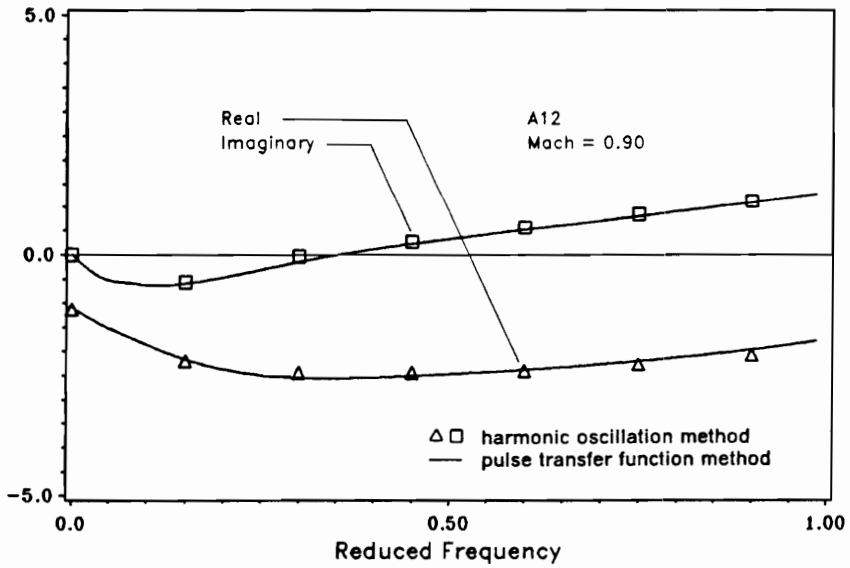


Figure 3.6.8 Comparison of the generalized aerodynamic coefficient $A_{12}$ , obtained using the harmonic oscillation and pulse transfer function method.

# Chapter 4

# Structural Nonlinearity Model

As mentioned in chapter 2, since virtually many aircraft structures contain some kind of nonlinearity, it is necessary to include this nonlinear behavior of the structure in the aeroelastic analysis. In this chapter, the derivation of several structural nonlinearity model are given. Two different approaches for predicting its effects on flutter behavior are described. The first one is the asymptotic expansion method for concentrated nonlinearities and the second one is a quasi-nonlinear approach that is used to include the effects of distributed nonlinearities. The procedure to include these effects into the aeroelastic solution, is also described. Results from the case studies that have been investigated are presented.

## 4.1 Overview

It is known that the structural nonlinearities play a significant role in the aeroelastic response and flutter characteristic of an aircraft structure. A survey of various types of structural nonlinearities and their sources in aircraft structures is given by Breitbach in Ref. 56 . In general, nonlinearities arising in an aircraft structure can be divided into two major groups :

1. Distributed nonlinearities which are activated continuously throughout the structure by elasto-dynamic deformation in riveted, screwed and bolted connections as well as within the structure components themselves. Because of the large number of the rivets and screws it can be assumed that the resulting damping and stiffness nonlinearities are more or less distributed throughout the structure. This type of nonlinearity, will directly affect the natural frequencies, mode shapes and damping coefficients of the structure.
2. Concentrated nonlinearities which act locally in the structure or part of the structure, especially in the control mechanism or in the part connecting the wing with external store. This type of nonlinearity, furthermore, may be identified according to its physical sources and effects and can be further sub-divided into three categories :

   (i) Freeplay and preload nonlinearity - because of the back-lash in the linkage elements of the control system or the solid friction in a control cable. The force - displacement relationships of these kind of nonlinearities are shown in Figs. 4.1.1 and 4.1.2 .

   (ii) Hysteresis type of nonlinearities , such as shown in Fig. 4.1.3 . As the applied force increases, the displacement grows linearly until a certain point at which a

jump occurs and beyond that the displacement becomes linear again. For the displacement in the opposite direction, the same jump occours at a different force level. This type of nonlinearity exists in the control system where static friction changes to sliding friction beyond the critical slip - stick point. It also can represent the slip of the wing skin panel at the rivets.

(iii) Cubic/Geometric nonlinerities , where the force exerted depends not only on the linear terms of the displacements but also on its higher - order terms, so the force - displacement relation is not linear as shown in Fig. 4.1.4 . In structure this effect found when a thin wing, or perhaps a propeller, is subjected to increasing amplitude of torsion.

The nonlinear effects on the actual structure and control mechanism, in general, come as a combination of these three kind of nonlinearities coupled with the distributed one.

At first sight, the above described distributed nonlinearities do not seem to be of great importance for aeroelastic investigations. However, many difficulties as occurring particularly during measurements in the vibration and flight flutter tests can be attributed to these effects. It has been shown in Ref. 88 that weak distributed stiffness nonlinearities in concurrence with equally weak manufacture - related structural asymmetries can be identified as physical sources of the well - known phenomenon of amplitude dependent normal mode asymmetries.

Very interesting problem concerning the measurement of generalized masses is investigated in Ref. 89 . The study comes to the conclusion that measured generalized masses can be considerably affected by measuring error due to small distributed

stiffness nonlinearities. Several means to overcome this problem are proposed in that study.

As to the influence of distributed physical nonlinearities toward the natural frequencies and damping coefficients, experience has shown that natural frequencies are weakly decreasing function of the amplitude of the vibration. But the overall damping coefficients can undergo much higher variation with respect to the vibration amplitude. In the ground vibration test of a F104G Starfighter aircraft as reported in Ref. 90 , test results indicate a trend of slightly reducing natural frequencies with increasing amplitude level ( Ref. 90 , Table 23 and 24 ). A strong nonlinear behavior was found for a fin torsion, tailplane coplanar rotation mode. With increasing amplitude the resonance frequency drops from 12.7 Hz to a minimum of 10.2 Hz but increase to 11.2 Hz with higher amplitude. No such common trend in damping coefficients was observed. For a wing bending, tailplane rotation mode, the damping coefficients decrease with an increasing amplitude ( Ref. 90 , Table 25 ). But for the wing torsion mode, the damping coefficient increases from 0.007 to a maximum value of 0.082 and then decreases to 0.042 at higher amplitude.
Consequently, it can be said that in aeroelastic analysis in which the structural properties ( natural frequencies , mode shapes and damping coefficients ) are obtained from the ground vibration test, certain changes of the critical flutter speed resulting from nonlinear damping effects can be expected, especially in cases of mild flutter. The nonlinear effects on natural frequencies and modes may be regarded as negligible.

Regarding the concentrated nonlinearities, it is evident that as the magnitude of the structural nonlinearity in a system becomes significant, the simplified linearized

approach may lead to inadmissible errors and in some cases to a totally different result, that may give a complete misinterpretation of what actually happens physically. Flutter studies of wing structure configurations with nonlinearities existing in the control surfaces, Refs. 51-58 , have shown that nonlinearities can affect not only the flutter speed but also the characteristics of the wing motion. With the assumption of linear structure theory, one can always define a wing flutter speed, above which the wing motion is unstable and the motion grows exponentially with time. However, as the amplitude of the oscillation begins to grow, the extent to which this increase continues depends upon the nature of the stiffness characteristic of the wing and that of the control surface. If the structure exhibits any type of nonlinearities, the stiffness characteristics change with amplitude of the motion and the oscillation may increase to an amplitude at which the wing experiences a stable limit cycle oscillation. A missile control surface having a freeplay nonlinearity, or 'slop' , is an example of a system whose response characteristic are function of the amplitude oscillation. At a particular flight speed, the amplitude of the oscillation, caused by external aerodynamic excitation , starts to build up. Due to the presence of a freeplay nonlinearity, in combination with increasing amplitude of oscillation, the effective stiffness of the system increases and the motion becomes stable at some limited amplitude. Thus, although the critical flutter speed of a linear configuration might be exceeded, destructive oscillation for nonlinear system may not result from this tendency toward instability. The system possibly experiences a failure due to large amplitude steady oscillation or due to fatigue .

Studies in Ref. 51 investigate the effects of control system nonlinearities, such as actuator force and the deflection limits, on performance of an active flutter supression system. Whereas flutter of a linear system is characterized by an exponential growth

of oscillation amplitude with time, flutter of a nonlinear system may be amplitude limited. On the other hand, a nonlinear system which is stable with respect to a small disturbance may be unstable with respect to large ones. Interest in this particular problem stems from studies in Ref. 54 of a passive wing/ store flutter suppression concept known as the 'decoupler pylon'. These studies have shown that a store mounted on a pylon with low pitch stiffness can provide substantial increase in flutter speed and reduce the dependency of flutter on the mass and inertia of the stores relative to that of stiff-mounted store. By decoupling the influence of store pitch inertia on wing torsion mode, the frequency separation between flutter critical modes is increased and the flutter speed is also increased.

As mentioned in Chapter 1, most of the studies on the structural, concentrated nonlinearity effects on flutter characteristics of aircraft structures make use of the describing function technique, Ref. 52 , which is an adaption of the method of harmonic balances. In this technique the motion of the structure is assumed to be sinusoidal, and the load developed in the nonlinear elements ( obtained from the load - displacement relationship of those elements ) are expanded in Fourier series. All harmonics except for the fundamental one are neglected, and the ratio of the amplitude of the fundamental harmonic of the load to that of the assumed displacement is used to define an 'equivalent ' linear spring. The equivalent linearized system is then analyzed by the conventional linear flutter theory. This technique gives satisfactory results for freeplay nonlinearities only when the amplitude of the motion is larger then the amplitude of the freeplay. If these two amplitudes are of the same order, significant errors can occur. This is due to the fact that only the fundamental term of the Fourier series expansion of the load ( as described in Section 4.2 ) is being used in computing the effective stiffness coefficient of the element. An asymptotic expan-

sion method is developed in this study for the purpose of including the higher order terms of the expansion series. In this method, the higher order terms can be included to any degree of approximation. This method, thus, does have a more general form compared to the describing function method.

The distributed nonlinearity effect in the aeroelastic calculation is employed indirectly by allowing the variation of the natural frequencies and damping coefficients with respect to the vibration amplitude. The next two sections are devoted to describing the asymptotic expansion method used to compute the effective spring stiffness coeffcients and the method used to include the distributed nonlinearity effects in the flutter analysis.

## 4.2 Asymptotic expansion method for a concentrated nonlinearity

The equivalent stiffness coefficients of the nonlinear spring are calculated using the asymptotic expansion method, based on the method proposed by Krylov - Bogoliubov - Mitropolsky for nonlinear oscillation problems, Ref. 92 . The fundamental idea of this linearization approach is based on the assumption that a nonlinear element can be approximately replaced by a linear element with equivalent internal energy when the element is activated at equivalent amplitude level.

Let us first, consider an oscillating system defined by a differential equation of the form

$$x'' + \omega^2 x = \varepsilon f(x, x') \qquad [4.2.1]$$

where $\omega$ is the frequency of the motion , $f(x, x')$ is small nonlinear perturbation forces which can be presented as a summation of periodic functions of period $2\pi$ radian , $\varepsilon$ is a small positive parameter , and prime indicates the derivatives with respect to time .

The contribution of the perturbation load in the solution is expanded in term of parameter $\varepsilon$ using a perturbation technique. This expansion function take the form of an asymptotic series comprised of integer power of $\varepsilon$ , which can be expressed as :

$$x = a\cos\psi + \sum_{n=1}^{N} \varepsilon^n u_n(a, \psi) + O(\varepsilon^{N+1}) \qquad [4.2.2]$$

Here, the first term is the fundamental solution ( $\varepsilon = 0$ ), and the remaining terms represents the asymptotic approximation of the nonlinear contribution to the response. $O(\varepsilon^{N+1})$ is a quantity of order $\varepsilon^{N+1}$ . The functions $u_n(a, \psi)$ are periodic functions in angular variable , $\psi$ , with period $2\pi$, and the motion amplitude , a . The parameter N indicates the order of the asymptotic approximation. The quantities a and $\psi$ are function of time and are defined by the differential equations :

$$\frac{da}{dt} = \sum_{n=1}^{N} \varepsilon^n A_n(a) + O(\varepsilon^{N+1})$$

$$\frac{d\psi}{dt} = \omega - \sum_{n=1}^{N} \varepsilon^n B_n(a) + O(\varepsilon^{N+1}) \qquad [4.2.3]$$

The right hand - side of this equation are series expansions of $\varepsilon$ and the parameter $A_n(a)$ and $B_n(a)$ which are function of the motion amplitude, a . We have to derive the function $u_n(a, \psi)$ , $A_n(a)$ , $B_n(a)$ such that the expression [4.2.2] , with a and $\psi$ substituted by function defined by Eq. [4.2.3] , will be the solution of the original equation, Eq. [4.2.1]. Differentiating Eq. [4.2.2] gives,

$$\frac{dx}{dt} = \{\cos\psi + \varepsilon \frac{\partial u_1}{\partial a} + \varepsilon^2 \frac{\partial u_2}{\partial a} + \ldots.\} \frac{da}{dt} + \{-a\sin\psi + \varepsilon \frac{\partial u_1}{\partial \psi} + \varepsilon^2 \frac{\partial u_2}{\partial \psi} + \ldots.\} \frac{d\psi}{dt} \qquad [4.2.4]$$

and differentiating this equation once more, yields

$$\begin{aligned}\frac{d^2x}{dt^2} = {} & \frac{d^2a}{dt^2}\left\{\cos\psi + \varepsilon \frac{\partial u_1}{\partial a} + \varepsilon^2 \frac{\partial u_2}{\partial a} + \ldots\right\} + \\ & \frac{d^2\psi}{dt^2}\left\{-a\sin\psi + \varepsilon \frac{\partial u_1}{\partial \psi} + \varepsilon^2 \frac{\partial u_2}{\partial \psi} + \ldots\right\} + \\ & \left(\frac{da}{dt}\right)^2\left\{\varepsilon \frac{\partial^2 u_1}{\partial a^2} + \varepsilon^2 \frac{\partial^2 u_2}{\partial a^2} + \ldots\right\} + \\ & 2\left(\frac{da}{dt}\frac{d\psi}{dt}\right)\left\{-\sin\psi + \varepsilon \frac{\partial^2 u_1}{\partial a \partial \psi} + \varepsilon^2 \frac{\partial^2 u_2}{\partial a \partial \psi} + \ldots\right\} + \\ & \left(\frac{d\psi}{dt}\right)^2\left\{-a\cos\psi + \varepsilon \frac{\partial^2 u_1}{\partial \psi^2} + \varepsilon^2 \frac{\partial^2 u_2}{\partial \psi^2} + \ldots\right\}\end{aligned} \qquad [4.2.5]$$

From Eq. [4.2.3] , the following relations can be derived,

$$\frac{d^2a}{dt^2} = \varepsilon^2 A_1 \frac{dA_1}{da} + \varepsilon^3 \ldots$$

$$\frac{d^2\psi}{dt^2} = \varepsilon^2 B_1 \frac{dA_1}{da} + \varepsilon^3 \ldots$$

$$\left(\frac{da}{dt}\right)^2 = \varepsilon^2 A_1^2 + \varepsilon^3 \ldots$$

$$\left(\frac{d\psi}{dt}\right)^2 = \varepsilon^2 B_1^2 + \varepsilon^3 \ldots$$

$$\left(\frac{d\psi}{dt}\right)\left(\frac{da}{dt}\right) = \omega^2 + 2\varepsilon\omega B_1 + \varepsilon^2 (B_1^2 + 2\omega B_2) + \varepsilon^3 \ldots \qquad [4.2.6]$$

Putting Eqs. [4.2.3] and [4.2.6] into Eqs. [4.2.4] and [4.2.5] , and substituting the resulting equations into Eq. [4.2.1] , which follows that the left hand side of Eq. [4.2.1] may be written as,

$$\begin{aligned} x'' + \omega^2 x = {} & \varepsilon \left\{ -2\omega A_1 \sin\psi - 2\omega a B_1 \cos\psi + \omega^2 \frac{\partial^2 u_1}{\partial\psi^2} + \omega^2 u_1 \right\} + \\ & \varepsilon^2 \left\{ \left(A_1 \frac{dA_1}{da} - aB_1^2 - 2\omega a B_2\right) \cos\psi - \right. \\ & \left(2\omega A_2 + 2A_1 B_1 + A_1 \frac{dB_1}{da} a\right) \sin\psi + 2\omega A_1 \frac{\partial^2 u_1}{\partial a \partial\psi} + \\ & \left. 2\omega B_1 \frac{\partial^2 u_1}{\partial\psi^2} + \omega^2 \frac{\partial^2 u_2}{\partial\psi^2} + \omega^2 u_2 \right\} + \varepsilon^3 \ldots . \end{aligned} \qquad [4.2.7]$$

Also the right hand side of Eq. [4.2.1] , with the help of Eqs. [4.2.2] and [4.2.4], may be written in the form

$$\begin{aligned} \varepsilon f(x, x') = {} & \varepsilon f(a\cos\psi, -a\sin\psi) + \varepsilon^2 \{ f'_x u_1 (a\cos\psi, -a\omega\sin\psi) + \\ & f'_{x'} (a\cos\psi, -a\omega\sin\psi)(A_1 \cos\psi - aB_1 \sin\psi + \\ & \frac{\partial u_1}{\partial\psi} \omega) \} + \varepsilon^3 \ldots \end{aligned} \qquad [4.2.8]$$

In order that the forgoing expression [4.2.2] may satisfy the original equation with an accuracy of the order $\varepsilon^{N+1}$ , it is necessary to equate coefficients of equal power of

$\varepsilon$ in the right hand side of Eqs. [4.2.7] and [4.2.8] upto terms of the N-th order (inclusive ). Doing so, yields to the following system of equations :

$$\omega^2 \left(\frac{\partial^2 u_1}{\partial \psi^2} + u_1\right) = f_0(a, \psi) + 2\omega A_1 \sin\psi + 2\omega a B_1 \cos\psi$$

$$\omega^2 \left(\frac{\partial^2 u_2}{\partial \psi^2} + u_2\right) = f_1(a, \psi) + 2\omega A_2 \sin\psi + 2\omega a B_2 \cos\psi$$

$$\vdots$$

$$\omega^2 \left(\frac{\partial^2 u_N}{\partial \psi^2} + u_N\right) = f_{N-1}(a, \psi) + 2\omega A_2 \sin\psi + 2\omega a B_2 \cos\psi \qquad [4.2.9]$$

where for brevity the following symbols have been used :

$$f_0(a, \psi) = f(a\cos\psi, -a\sin\psi)$$

$$f_1(a, \psi) = u_1 f_{x'}(a\cos\psi, -a\omega\sin\psi) + \left[A_1\cos\psi - aB_1\sin\psi + \omega\frac{\partial u_1}{\partial \psi}\right]$$
$$f'_{x'}(a\cos\psi, -a\omega\sin\psi) + \left(aB_1^2 - A_1\frac{dA_1}{da}\right)\cos\psi +$$
$$\left(2A_1 B_1 + A_1\frac{dB_1}{da}a\right)\sin\psi - 2\omega A_1\frac{\partial^2 u_1}{\partial a\partial\psi} + 2\omega B_1\frac{\partial^2 u_1}{\partial\psi^2}$$

[ 4.2.10 ]

It can be observed that $f_i(a, \psi)$ is a periodic function of the variable $\psi$ with a period $2\pi$ and is dependent on a. The explicit expression of these function will be known as soon as the expressions for $A_i(a)$ , $B_i(a)$ , and $u_i(a, \psi)$ are found. So, in seeking the complete solution up to the N-terms, the computation have to be started from N = 1. For the value of N = 1, $A_1$ , $B_1$ and $u_1$ are determined from the first equation in [4.2.9]. Examine the Fourier series expansion of $f_0(a, \psi)$ and $u_1(a, \psi)$ :

$$f_0(a,\psi) = g_0(a) + \sum_{n=1}^{\infty}\{g_n(a)\cos(n\psi) + h_n(a)\sin(n\psi)\}$$

$$u_1(a,\psi) = v_0(a) + \sum_{n=1}^{\infty}\{v_n(a)\cos(n\psi) + w_n(a)\sin(n\psi)\}$$

Substituting these two expressions into the first equation in [4.2.9] , and equating coefficients of identical harmonics ( such as $\cos\psi$ , $\sin\psi$ , ..... ) the expression for $A_1(a)$ , $B_1(a)$ are uniquely determined as follows

$$A_1(a) = \frac{1}{2\omega}h_1(a) \qquad B_1(a) = \frac{1}{2\omega a}g_1(a) \qquad [4.2.11]$$

and then $u_1(a,\psi)$ expression is obtained as

$$u_1(a,\psi) = \frac{g_0(a)}{\omega^2} + \frac{1}{\omega^2}\sum_{n=2}^{\infty}\frac{\{g_n(a)\cos n\psi + h_n(a)\sin n\psi\}}{(1-n^2)}$$

By completely determining $A_1(a)$ , $B_1(a)$ , $u_1(a,\psi)$ , from Eq. [4.2.10] the explicit expression of $f_1(a,\psi)$ can be formulated. Expanding it in a Fourier series ,

$$f_1(a,\psi) = \bar{g}_0(a) + \sum_{n=1}^{\infty}\{\bar{g}_n(a)\cos(n\psi) + \bar{h}_n(a)\sin(n\psi)\}$$

Using the second equation in [4.2.9] and following the same step as in the calculation of $A_1$ , $B_1$ explained above, the $A_2(a)$ , $B_2(a)$ expression are obtained,

$$A_2(a) = \frac{1}{2\omega}\bar{h}_1(a) \qquad B_2(a) = \frac{1}{2\omega a}\bar{g}_1(a) \qquad [4.2.12]$$

$$u_2(a, \psi) = \frac{\bar{g}_0(a)}{\omega^2} + \frac{1}{\omega^2} \sum_{n=2}^{\infty} \frac{\{ \bar{g}_n(a) \cos n\psi + \bar{h}_n(a) \sin n\psi \}}{(1 - n^2)}$$

So, we have a process for determining successively and uniquely the quantities

$$A_n(a) \ , \ B_n(a) \ , \ u_n(a, \psi) \ , \ n = 1,2, ....$$

up to any value of n . The solution of the Eq. [4.2.1] can be constructed to any degree of approximation by substituting the expression of $u_n(a, \psi)$ into Eq. [4.2.2].

The Fourier series coefficients $g_n(a)$ , $h_n(a)$ can be written as

$$g_n(a) = \frac{1}{2} \pi \int_0^{2\pi} f(a \cos \psi \ , \ -a\omega \sin \psi) \cos n\psi \, d\psi$$

$$h_n(a) = \frac{1}{2} \pi \int_0^{2\pi} f(a \cos \psi \ , \ -a\omega \sin \psi) \sin n\psi \, d\psi$$

Then, for the second order approximation, the $A_1$ , $A_2$ , $B_1$ , $B_2$ coefficients can be written as

$$A_1(a) = \frac{-1}{2\pi^2 \omega} \int_0^{2\pi} f(a \cos \psi, -a \sin \psi) \sin \psi \, d\psi$$

$$B_1(a) = \frac{-1}{2a\pi^2 \omega} \int_0^{2\pi} f(a \cos \psi, -a \sin \psi) \cos \psi \, d\psi$$

$$A_2(a) = \frac{-1}{2\omega} \left[ \frac{dB_1}{da} aA_1 + 2A_1B_1 \right] - \frac{1}{2\omega\pi^2} \int_0^{2\pi} \{ f'_x(a \cos \psi, -a\omega \sin \psi) u_1 + f'_{x'}(a \cos \psi, -a\omega \sin \psi)(A_1 \cos \psi - aB_1 \sin \psi + \frac{\partial u_1}{\partial \psi} \omega) \} \sin \psi \, d\psi$$

$$B_2(a) = \frac{1}{2a\omega} \left[ \frac{dA_1}{da} A_1 - aB_1^2 \right] - \frac{1}{2a\omega\pi^2} \int_0^{2\pi} \{ f'_x(a \cos \psi, -a\omega \sin \psi) u_1 + f'_{x'}(a \cos \psi, -a\omega \sin \psi)(A_1 \cos \psi - aB_1 \sin \psi + \frac{\partial u_1}{\partial \psi} \omega) \} \cos \psi \, d\psi$$

[4.2.13]

Consider now the oscillation of a system with a nonlinear spring and of mass m. The oscillation equation is given by

$$mx'' + p(x) = 0 \qquad [4.2.14]$$

in which the relation between elastic force and displacement is nonlinear and may be expressed as

$$p(x) = K x + \varepsilon \chi(x) \qquad [4.2.15]$$

where $\chi(x)$ is function that account for the nonlinear load - displacement relationship in the spring and K is the linear spring coefficient. This equation will belong to a type already discussed, Eq. [4.2.1] with

$$\omega^2 = K / m \quad , \qquad f(x, x') = -\chi(x) / m$$

As it already been shown, the solution of Eq. [4.2.14] have a similar form as given by Eq. [4.2.2] , which satisfy the condition in Eq. [4.2.3] . Introducing two functions of amplitude , $\overline{K}(a)$ and $\overline{\lambda}(a)$ , defined as

$$\overline{\lambda}(a) = \frac{1}{a} \sum_{n=1}^{N} \varepsilon^n A_n(a) + O(\varepsilon^{N+1})$$

$$\overline{K}(a) = K + \sum_{n=1}^{N} \varepsilon^n B_n(a) + O(\varepsilon^{N+1}) \qquad [4.2.16]$$

Considering these two expression, the condition in Eq. [4.2.3] may be rewritten in the following form,

$$\frac{da}{dt} = -\frac{\bar{\lambda}(a)}{m} a$$

$$\frac{d\psi}{dt} = \omega_e \quad \text{in which} \quad \omega_e^2 = \frac{\bar{K}(a)}{m}$$

Substituting these relations into the expression for $x'$ , and $x''$ into Eqs [4.2.4] and [4.2.5], and then use these result to replace terms at the left hand side of Eq. [4.2.14] , gives the oscillation equation in the form,

$$x'' + \bar{\lambda}(a)\, x' + \bar{K}(a)x = O(\varepsilon^{N+1})$$

Hence, the approximation function of the form as defined by Eq. [4.2.2] satisfies the linear differential equation of the oscillation of the form

$$m\, x'' + \bar{\lambda}(a)\, x' + \bar{K}(a)x = 0. \qquad [4.2.17]$$

with the accuracy of the order of magnitude $\varepsilon^{N+1}$. In other words, the nonlinear system represented by Eq. [4.2.14] is equivalent to the system represented by Eq. [4.2.17] with

$$p(x) = \bar{\lambda}(a)\, x' + \bar{K}(a)\, x$$

representing the nonlinear damping and spring forces in which $\bar{\lambda}$ and $\bar{K}$ satisfy Eq. [4.2.16] . The function $\bar{\lambda}$ , therefore, is called the equivalent damping coefficient and $\bar{K}$ is called the equivalent stiffness coefficient. Instead of using the expression given by Eq. [4.2.16] , the equivalent stiffness coefficient may be written as a series expansion of the linear stiffness coefficient

$$\bar{K} = K(1 + \varepsilon B_1 + \varepsilon^2 B_2 + .....) \qquad [4.2.18]$$

The number of terms used in the expression identify the order of the approximation. The first order approximation ( referred to as the 'describing function method ' )

keeps the first two term of the series, the second-order approximation keeps up to the $\varepsilon^2$ terms, and so on.

The nonlinear elastic force - displacement function, p (x) , is obtained from the load - displacement relationship. For a spring with preload nonlinearity, see Fig. 4.1.2 , undergoing sinusoidal oscillation of amplitude a , for instance, the elastic force - displacement functions are given by

1. $a \leq \delta p$

$$p(x) = K x$$

2. $\delta p < a \leq (\delta p + \delta s)$

$$p(x) = K x + K(a \cos \Phi_0 - a \cos \psi) \qquad \text{for } 0 \leq \psi \leq \Phi_0$$

$$= K x \qquad \text{for } \Phi_0 \leq \psi \leq \pi$$

3. $a \geq (\delta p + \delta s)$

$$p(x) = K x + K(a \cos \Phi_0 - a \cos \Psi_0) \qquad \text{for } 0 \leq \psi \leq \Psi_0$$

$$= K x + K(a \cos \Phi_0 - a \cos \psi) \qquad \text{for } \Psi_0 \leq \psi \leq \Phi_0$$

$$= K x \qquad \text{for } \Phi_0 \leq \psi \leq \pi$$

where $\Psi_0 = \cos^{-1}\left(\frac{\delta p + \delta s}{a}\right)$

$\Phi_0 = \cos^{-1}\left(\frac{\delta p}{a}\right)$

$\psi = \cos^{-1}\left(\frac{x}{a}\right)$

The expression of $\chi(x)$ may be deducted from each of the p(x) functions given above using Eq. [4.2.15] . Once the $\chi(x)$ expressions are known, the coefficient of the series for the equivalent stiffness coefficient , $B_i(a)$ , can be easily computed. The integration of Eq. [4.2.13] gives the coefficient needed for a second order approximation,

$$\overline{K} = K(1 + \varepsilon B_1 + \varepsilon^2 B_2)$$

1. $a < \delta p$

$$\varepsilon B_1 = 0 \quad , \quad \varepsilon^2 B_2 = 0$$

2. $\delta p < a < (\delta p + \delta s)$

$$\varepsilon B_1 = \frac{1}{\pi}\left[\Phi_0 - \frac{1}{2}\sin 2\Phi_0\right]$$

$$\varepsilon^2 B_2 = \frac{1}{2\pi^2}\left\{\left(\frac{\Phi_0}{2} - \frac{1}{4}\sin 2\Phi_0\right)^2 - \left(\frac{3}{4} - \cos\Phi_0 + \frac{1}{4}\cos 2\Phi_0\right)^2 + 2\sin\Phi_0\,(\Phi_0\cos\Phi_0 - \sin\Phi_0) - \sum_{n=2}^{N}\left(\frac{1}{n^2-1}\right)(\sigma_{n1} + \sigma_{n2})\right\}$$

3. $a > (\delta p + \delta s)$

$$\varepsilon B_1 = \frac{1}{\pi}\left\{\frac{1}{4}(\sin 2\Phi_0 - \sin 2\Psi_0) - \frac{1}{2}(\Phi_0 - \Psi_0)\right\}$$

$$\varepsilon^2 B_2 = \frac{K}{2\pi^2}\left\{(\varepsilon B_1)^2 - \left[(\cos\Phi_0 - \cos\Psi_0) - (\cos^2\Phi_0 - \cos^2\Psi_0) + \frac{1}{4}(\cos 2\Phi_0 - \cos 2\Psi_0)\right]^2 + \left[2(\sin\Phi_0 - \sin\Psi_0)(\Phi_0\cos\Phi_0 - \Psi_0\cos\Psi_0 - \sin\Phi_0 + \sin\Psi_0)\right] - \sum_{n=2}^{N}\left(\frac{2}{n^2-1}\right)(\sigma_{n1} + \sigma_{n2})\right\}$$

$$\Phi_0 = \cos^{-1}\left(\frac{\delta p}{a}\right)$$

$$\Psi_0 = \cos^{-1}\left(\frac{\delta p + \delta s}{a}\right)$$

$$\sigma_{n1} = \int_{\Psi_0}^{\Phi_0} \Gamma_n \cos n\theta \cos\theta \, d\theta$$

$$\sigma_{n1} = \int_{\Psi_0}^{\Phi_0} \Gamma_n \sin n\theta \cos\theta \, d\theta$$

$$\Gamma_n = \int_{0}^{\Phi_0} (\cos\Psi - \cos\theta) \sin n\theta \, d\theta$$

The same expression can also be derived for spring with freeplay nonlinearity. The ratio between the values of $\overline{K}$ , the equivalent stiffness coefficients, and the linear stiffness coefficients K ( $\overline{K}/K$ is called the effective stiffness coefficient , $\delta$ ) , for a preloaded spring as obtained from the asymptotic expansion method is shown in Fig. 4.2.1 . For this calculation the value of deadband , $\delta s$ is equal to 0.4° and $\delta s/\delta p$ , the ratio of the deadband to the preload amplitude , equal to 4 . Presented here is the effective stiffness coefficients for both the first and second order solutions. For amplitude of motion less than the preload amplitude, $\delta p$ , the effective stiffness coefficient is one and the response is linear. As the amplitude of the motion increases, the stiffness decrease. This softening effect is due to the deadband, $\delta s$ , in the spring causing the effective stiffness to be less than the linear value. As the amplitude increases well beyond the deadband region, the influence of the nonlinearity become small, and the magnitude of the effective stiffness coefficient again approaches one. While both first and second order solution shown in Fig. 4.2.1 exhibit the same trends, the second order solution predicts a larger stiffness reduction when the amplitude of the motion falls within the deadband region of the load - displacement curve, Fig. 4.1.2 . This results because the second-order solution includes higher-order harmonic terms. At higher value of amplitude, the first and second order solutions converge and asymptotically approach the linear solution . Comparison of the first order solution with the solution given by Laurenson et. al. in Ref. 55 are

in good agreement. Laurenson solution used the discribing function method which, as mentioned earlier, is equivalent to the first order approximation. It was found from several calculations that the larger the ratio value of $\delta s/\delta p$ , at a constant value of $\delta p$ , the greater the difference between the first and second-order approximation. Figure 4.2.2 represent the effective stiffness coefficients at different values of $\delta s/\delta p$ , for the values of $\delta p$ equal to 0.3° , 0.35° , and 0.5° and $\delta s$ equal to 0.3° , 0.7° , and 1.5° ( this associated with the $\delta s/\delta p$ values of 1 , 2 and 3 , respectively ) . As this ratio increases ( i.e. as the width of the deadband path , $\delta s$ , increases ), the reduction in the effective stiffness coefficient after the linear path increases. Also, the recovery of the stiffness coefficients in the linear path after the deadband, slows down as the $\delta s/\delta p$ ratio increases. For a constant value of preload , $\delta p$ , the characteristic of the nonlinear spring is greatly dependent upon the width of the deadband, the larger this width, the greater the reduction in the effective stiffness. The same tendency also occurs in springs having a freeplay type of nonlinearity, as illustrated in Fig. 4.1.1 . In this case the effective stiffness coefficient dependent upon the amplitude of the freeplay $\delta s$ , as shown in Fig. 4.2.3 . The calculations were performed for values of the freeplay amplitude of 1° , 1.5° and 2° , respectively. For the amplitude of motion less than the freeplay amplitude, the effective stiffness is zero. As the amplitude increases, the linear spring predominates and the magnitude of $\overline{K}$ approaches that of K . At a smaller value of the freeplay amplitude, the linear value of the stiffness could be approached at a smaller motion amplitude. Mathematically, the linear stiffness value , K , can only be obtained if the ratio of the motion amplitude to the freeplay amplitude approaches infinity ( i.e. either $\delta s$ have to be very small or the amplitude of the motion have to be very large ).

## 4.3 Systems with a distributed nonlinearity

The distributed nonlinearity effects in flutter calculation are imposed indirectly through the variation of natural frequencies and damping coefficients of the wing structure with respect to the oscillation amplitude. For the most part, the variations of these quantities are obtained from the ground vibration test of the structure. For example, variation of the natural frequency and damping coefficients with respect to the oscillation amplitude for swept wing obtained from the ground vibration test, Ref. 91 , are shown in Figs. 4.3.1 and 4.3.2 , respectively. The wing tested has a leading edge sweep angle of 40° , semispan taper ratio 0.47 and aspect ratio of 1.515. It has to be noted that this wing configuration is not exactly the same as the 45° swept wing configuration that is being used for flutter calculation in the present study. However, because of the lack of the ground vibration data available for the latter wing configuration , in the investigation of the distributed nonlinearity effects on the flutter solutions , the 45° swept wing model is assumed to have the natural frequency and damping coefficient variation as given in Figs. 4.3.1 and 4.3.2 . This assumption was made based on the facts that the geometry of the two wings are very similar and also the first four values of the natural frequency of both wing are close to each other.

It can be observed from Fig. 4.3.1 that the natural frequencies have a weak variation with respect to the amplitude, except for the fourth mode ( second torsion mode ). On the contrary, the damping coefficients have a strong variations for all of the 4 structural modes. In Ref. 91 , Kussner attributed this variation due to the slipping of the riveted and bolted joints which changes the stiffness and resonance ( natural ) frequency and cause energy loss and damping. These changes are not constant for different levels of motion amplitude. Therefore, the variation of the resonance fre-

quencies and damping coefficients with respect to the motion amplitude are not linear functions. Another factor that may also affect this variation is the temperature distribution over the aircraft structure. If sun shines on the aircraft during the vibration test, the temperature at different points in the structure may become different. In that case, the stiffness tensor and the phase resonance frequency can change rapidly, as much as 0.5 Hz, due to thermoelastic effects. This kind of thermoelastic effect can become an important consideration in the flight flutter test, since the aircraft will be exposed to the sun for a very long period of time during the test, Ref. 89 . Both of these variations ( those of frequency and damping ) are applied in the flutter calculation of the three-dimensional wing model by performing the calculations for several values of motion amplitude. The elements of the stiffness and damping matrices, [ K ] and [ C ] respectively used in the aeroelastic equation , Eq. [2.2.1] , become motion - amplitude dependent. The elements of these matrices can be redefined as follows :

$$
\begin{aligned}
C_{i,j}(a) &= 2\,\zeta_i(a)\,M_{i,j}\,\omega_{n,i}(a) && \text{for } i = j \\
&= 0 && \text{for } i \neq j \\
K_{i,j}(a) &= \omega_{n,i}^2(a) M_{i,j} && \text{for } i = j \\
&= 0 && \text{for } i \neq j
\end{aligned}
$$

where a is the amplitude of the motion and $\zeta_i(a)$ and $\omega_{n,i}(a)$ variations are given by Figs. 4.3.1 and 4.3.2 , respectively. The aeroelastic equation is solved for several values of the amplitude, and as a result of the analysis, we get variation of the flutter dynamic pressure with respect to the motion amplitude.

## 4.4 Aeroelastic equations with concentrated nonlinearities

As in the case of distributed nonlinearity, with the concentrated nonlinearity in the structure included, the aeroelastic equations will change. The stiffness coefficient is not constant, but is a function of the motion amplitude. For the frequency domain solution, it is assumed that , in the present of structural nonlinearities , the structure does not exhibit a limit cycle oscillation with large amplitude, and that the superposition principle of the aerodynamic load is still valid. It is also assumed that the motion amplitude is small such that the TSD flow equation is still applicable.

### *4.4.1 Two-dimensional airfoil section model*

For the airfoil section model, the nonlinearity may exist in either one of the two ( torsional or bending ) springs, see Fig. 2.1.1 . This model can be used to represent , for instance, the spring tab system in which the concentrated nonlinearity deliberately introduced into the control mechanism in order to relieve pilot operation. At small tab deflection, the stiffness of the spring tab system is relatively high resulting from special pre-tension of the tab spring. At certain tab deflection the pre-tension ceases and the stiffness suddenly drops to a much lower value. This spring properties can be categorized as preload spring nonlinearity. Such spring tab systems have already proven, Ref. 56 , to be very susceptible to a dangerous kind of divergent flutter.

Power operated controls may also have nonlinear effects and could be appropriately modeled using the typical section spring model. The dynamic behavior of power control mechanism is characterized in Ref. 93 as :

1. The complex highly damped stiffness of the hydraulic actuator itself is a nonlinear function of the vibration amplitude as well as of the actuator preload and of the position of the jack piston,
2. The linkage mechanism between the actuator body and the aircraft structure is affected by considerable nonlinear effects due to solid friction and back-lash especially in the hinge bearing , and
3. For a case in which the vibratory motions of the aircraft structure result in relative motions between piston and cylinder of the servo valve, actuator forces are induced which will vary with the vibration amplitude. This kind of dynamic interaction can lead to stability problems.

In Ref. 93 , it was also stated that the dynamic stiffness of the hydraulic actuators is usually a frequency dependent function to be taken into account as a very important part of the flutter clearance process.

Following the derivation in Section 4.2 , the equivalent stiffness coefficients, Eq. [4.2.18] , can be written as

$$\overline{K}_h = \delta_h K_h \qquad \text{and} \qquad \overline{K}_\alpha = \delta_\alpha K_\alpha$$

where $\delta_h$ and $\delta_\alpha$ represent the effective stiffness coefficients of the spring, and by Eq. [4.2.18] is defined as

$$\delta_{h \text{ or } \alpha} = 1 + \varepsilon B_1 + \varepsilon^2 B_2 + \ldots \qquad [4.4.1]$$

With this notation, the stiffness matrix in the aeroelastic equation, Eqs. [2.1.7] and [2.1.8] , may be written in the following form to include the nonlinearity effects,

$$[\bar{K}] = \left(\frac{2}{\bar{U}k}\right)^2 \begin{bmatrix} (\omega_h/\omega_\alpha)^2 \delta_h & 0 \\ 0 & r_\alpha^2 \delta_\alpha \end{bmatrix} \qquad [4.4.2]$$

which is called the equivalent stiffness matrix of the system. Since the $B_1, B_2, \ldots$ coefficients are motion amplitude dependent, elements of this matrix will also dependent on the motion amplitude. Introducing this matrix into the aeroelastic equation of motion, Eq. [2.1.7] , to replace the stiffness matrix [ K ] , the resulting equation for aeroelastic analysis in time domain can be written as

$$[M]\begin{Bmatrix} \xi'' \\ \alpha'' \end{Bmatrix} + [C]\begin{Bmatrix} \xi' \\ \alpha' \end{Bmatrix} + \left(\frac{1}{k^2}\right)[\bar{K}]\begin{Bmatrix} \xi \\ \alpha \end{Bmatrix} = \left(\frac{4}{\pi\mu k^2}\right)\begin{Bmatrix} -C_l \\ 2C_m \end{Bmatrix} \qquad [4.4.3]$$

and for aeroelastic analysis in frequency domain , Eq. [2.1.8] , can be written as

$$[[M] + [C] - [A]]\begin{Bmatrix} \xi_0 \\ \alpha_0 \end{Bmatrix} = \lambda[\bar{K}]\begin{Bmatrix} \xi_0 \\ \alpha_0 \end{Bmatrix} \qquad [4.4.4]$$

Note that both Eqs> [4.4.3] and [4.4.4] are amplitude dependent. The solution of this equation are computed , as described an detail in Section 5.2 , for several values of amplitude of the motion. From this solution, the variation of the flutter speed with respect to the motion amplitude is obtained.

### *4.4.2 Three - dimensional structural model*

The three - dimensional wing model that is used to study the concentrated nonlinearities effects is shown in Fig. 4.4.1 . This model is similar to the structure model described in Section 2.2 , with the addition of two springs ( roll and torsion springs ) at the wing root. This model is representative of a control surface with a loose hinge and/or joint slippage in the surface support structure and control actuator. It can also be used for the problem dealing with tactical missile wing pair ( control surface ) , as investigated by Laurenson, Ref. 55 , in which the nonlinearities exist in the wing root attachment with missile body. In both cases, structural nonlinearities were associated with the root rotational support springs, $K_\theta$ and $K_\phi$ .

By including these two rigid motions into elastic motion of the system and taking also into account the nonlinearities on them, the system flutter problem is represented by the following system of nonlinear equation, Ref. 65 ,

$$\begin{bmatrix} [H] & [PF] \\ [PF]^T & [M] \end{bmatrix} \{v''\} + \begin{bmatrix} [C1] & 0 \\ 0 & [C] \end{bmatrix} \{v'\} + \begin{bmatrix} [K1] & 0 \\ 0 & [K] \end{bmatrix} \{v\} = \bar{q} \begin{bmatrix} [A_r] & [A_{re}] \\ [A_{er}] & [A_e] \end{bmatrix} \qquad [4.4.5]$$

where { v } is the vector of generalized coordinates and which consists of $\theta$ , $\phi$ and the generalized coordinate associated with wing elastic modes , { q }.

$$\{v\} = \begin{Bmatrix} \theta \\ \phi \\ \{q\} \end{Bmatrix}$$

in which $\theta$ is the generalized coordinate associated with pitching displacement ( rotation about y - axis ) , and $\phi$ is the generalized coordinate associated with rolling displacement ( rotation about x - axis ) . Matrix [ H ] is the matrix of moment of inertia of the rigid wing, and is defined as

$$[H] = \begin{bmatrix} I_\theta & I_{\theta\phi} \\ I_{\theta\phi} & I_\phi \end{bmatrix}$$

in which $I_\theta$ and $I_\phi$ are the rigid moment of inertia of the wing about pitching axis and rolling axis, respectively. $I_{\theta\phi}$ is the product of inertia of the rigid wing.

Matrix [ PF ] is the matrix of inertial coupling between rigid and elastic mode of the wing, and which is defined as

$$[PF] = \begin{bmatrix} I_{\theta 1} & \cdots & I_{\theta n} \\ I_{\phi 1} & \cdots & I_{\phi n} \end{bmatrix}$$

where n is the number of the elastic modes use in the analysis and $I_{\theta i}$ is the inertial coupling between the rigid pitching motion , $\theta$ , and the i-th elastic mode. These quantities essentially are the product of inertia of the wing structure calculated with respect to the pitching axis and the elastic axis of the i-th mode. The i-th mode elastic axis is defined as the lines of zero deflection in the i-th elastic mode and can be computed from the mode deflection contour, as shown in Fig. 5.5.2 . $I_{\phi i}$ is the

inertial coupling between the rigid rolling motion , $\phi$ , and the i-th elastic mode, and is defined in a similar way as $l_{\theta i}$ .

The [ K1 ] matrix is the stiffness matrix of the rolling and torsion spring including the nonlinearity effects ; the form of this matrix is similar to the one given by Eq. [4.4.2] , which is

$$[\,K1\,] = \begin{bmatrix} K_\theta \delta_\theta & 0 \\ 0 & K_\phi \delta_\phi \end{bmatrix}$$

where $K_\theta$ and $K_\phi$ are the linear stiffness coefficients of the torsion spring and rolling spring, respectively , and $\delta_\theta$ and $\delta_\phi$ are the effective spring coefficients of the torsion and rolling spring, respectively, as defined in Eq. [4.4.1] . [ C1 ] is the damping matrix associated with the rigid rolling and pitching displacements ,

$$[\,C1\,] = \begin{bmatrix} \zeta_\theta & 0 \\ 0 & \zeta_\phi \end{bmatrix}$$

where $\zeta_\theta$ and $\zeta_\phi$ are the damping coefficient associated with the pitching and rolling motions, respectively .

Matrix $[\,A_e\,]$ is the matrix of generalized aerodynamic loads associated with the wing elastic displacements whose elements are defined by Eq. [2.2.2] , and $[\,A_r\,]$ is the is the matrix of generalized aerodynamic loads associated with the rigid rolling and pitching displacements, defined as :

$$[\,A_r\,] = \begin{bmatrix} A_{\theta\theta} & A_{\theta\phi} \\ A_{\phi\theta} & A_{\phi\phi} \end{bmatrix}$$

The $[A_{re}]$,$[A_{er}]$ matrices are the matrices of aerodynamic load couplings between rigid and elastic displacements which are defined, respectively, as

$$[A_{re}] = \begin{bmatrix} A_{\theta 1} & \cdots & A_{\theta n} \\ A_{\phi 1} & \cdots & A_{\phi n} \end{bmatrix} \qquad [A_{er}] = \begin{bmatrix} A_{1\theta} & A_{1\phi} \\ \cdot & \cdot \\ \cdot & \cdot \\ A_{n\theta} & A_{n\phi} \end{bmatrix}$$

The [ M ] , [ K ] and [ C ] matrices are the generalized mass, stiffness and damping matrices of the elastic wing, respectively , which are defined by Eq. [2.2.1] . The elements of rigid, rigid - elastic and elastic - rigid generalized aerodynamic load matrices, $[A_r]$, $[A_{re}]$, $[A_{er}]$ , are computed using the same approach as for the aerodynamic load matrix for the elastic modes of the wing by considering the roll and pitch displacements as two additional wing modes. $A_{i\theta}$ , for instance, is defined as the generalized aerodynamic force coefficient from the pressure induced by the rigid pitching mode acting through the displacement of elastic mode i . Following the definition given by Eq. [2.2.2] , it can be expressed as

$$A_{i\theta} = -\bar{q}c^2 \int_S \frac{\Delta p_\theta(x,y)}{\bar{q}} \, h_i(x,y) \, \frac{dS}{c^2}$$

where $\Delta p_\theta(x,y)$ is the total pressure distribution on the wing surface due to rigid pitching displacement. These quantities are calculated following the procedure described in Section 3.6.2 .

Equation [4.4.5] may be transformed into the s - plane , in the same way as it was explained in Section 2.2 for purely elastic wing system. This gives the aeroelastic equation in the following form

$$\left[[\bar{M}]s^2 + [\bar{C}]s + [\bar{K}]\right]\{\tilde{q}\} + (\bar{q}c^2)[\tilde{A}]\{\tilde{q}\} = 0 \qquad [4.4.6]$$

where

$$[\bar{M}] = \begin{bmatrix} [H] & [PF] \\ [PF]^T & [M] \end{bmatrix} \qquad [\bar{C}] = \begin{bmatrix} [C1] & 0 \\ 0 & [C] \end{bmatrix}$$

$$[\bar{K}] = \begin{bmatrix} [K1] & 0 \\ 0 & [K] \end{bmatrix} \qquad [\bar{A}] = \begin{bmatrix} [A_r] & [A_{re}] \\ [A_{er}] & [A_e] \end{bmatrix}$$

$[\tilde{A}]$ is the Laplace transform of the aerodynamic force matrix $[\bar{A}]$ . Applying the Pade's interpolation to matrix $[\tilde{A}]$ , following the procedure in Appendix B for the linear system, this equation can be further written into the short form as represented by Eq. [2.2.5] ,

$$\bar{s}\{Z\} = [\bar{H}]\{Z\} \qquad [4.4.7]$$

Matrix $[\bar{H}]$ is defined in a similar way as matrix $[H]$ in Eq. [B.5] in which matrices $[\bar{M}]$ , $[\bar{C}]$ , $[\bar{K}]$ and $[\bar{A}]$ are use to replace matrices $[M]$ , $[C]$ , $[K]$ and $[\tilde{A}]$ , respectively. This equation is used to study the concentrated nonlinearity effects on the wing structure. The solution of this equation is carried out by applying the root-locus method discussed in Section 5.3.2 and some of the results is presented in Section 5.5.3 .

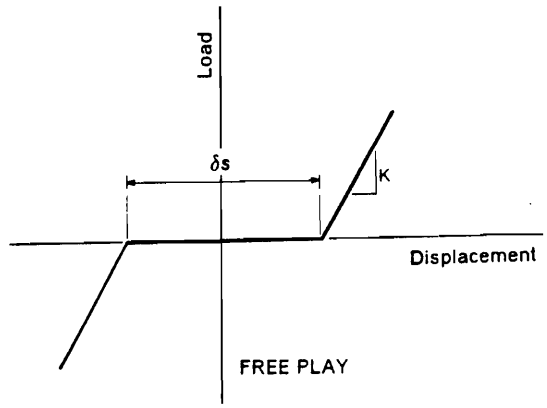


Figure 4.1.1 Load-displacement relationship for a spring with freeplay nonlinearity.

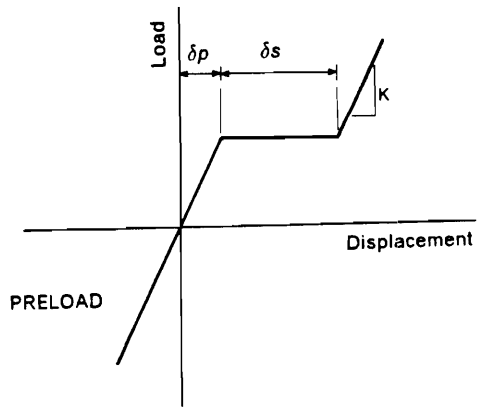


Figure 4.1.2 Load-displacement relationship for a spring with preload nonlinearity.

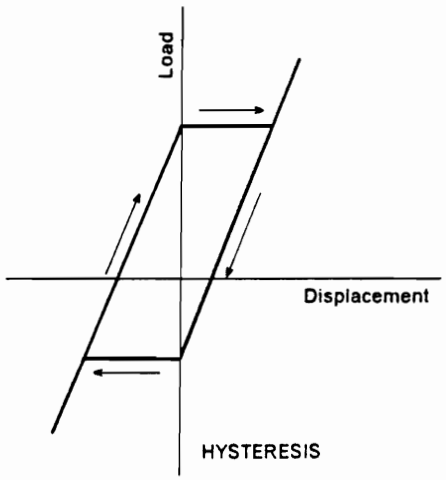


Figure 4.1.3 Load-displacement relationship for a spring with hysterisis nonlinearity.

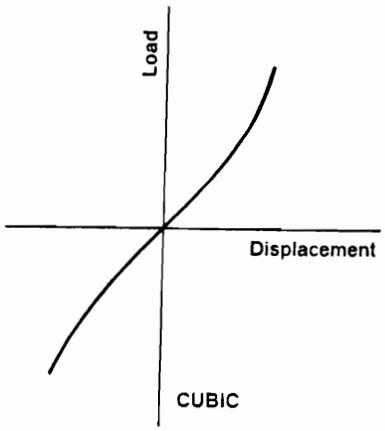


Figure 4.1.4 Load-displacement relationship for a spring with cubic nonlinearity.

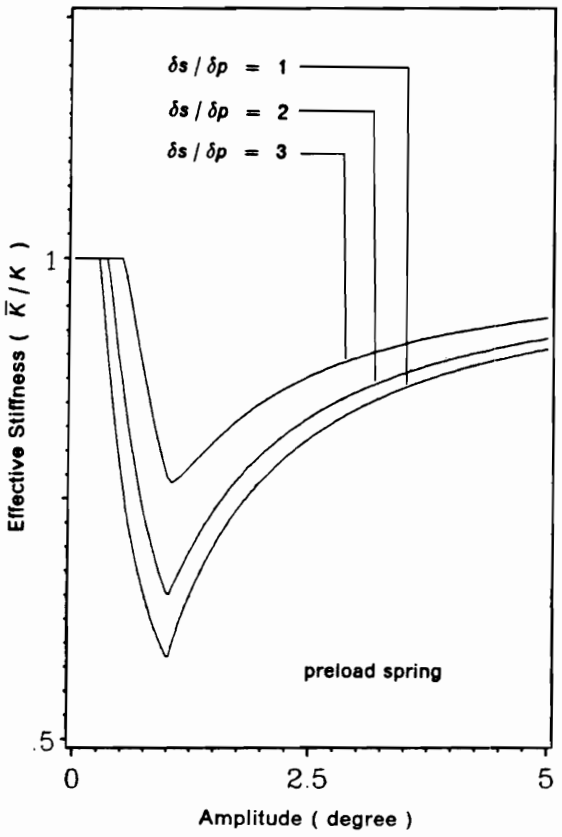


Figure 4.2.1 Effective Stiffness Coefficients ($\bar{K}/K$) variation with displacement amplitude of the spring with preload nonlinearity, $\delta s/\delta p = 4$ and $\delta s = 0.4°$

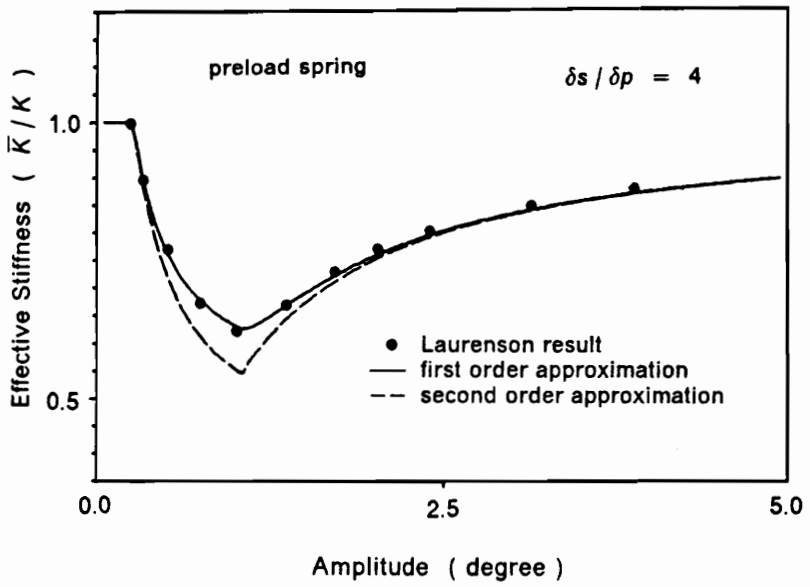


Figure 4.2.2 Effective Stiffness Coefficients ($\bar{K}/K$) variation with displacement amplitude of the spring with preload nonlinearity, for various $\delta s/\delta p$ values.

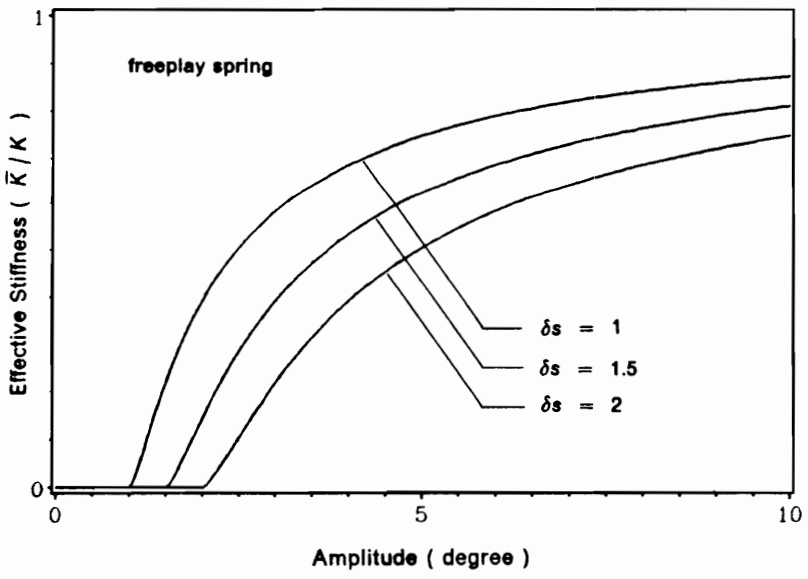


Figure 4.2.3 Effective Stiffness Coefficients ($\bar{K}/K$) variation with displacement amplitude of the spring with freeplay nonlinearity, for various $\delta s$ values .

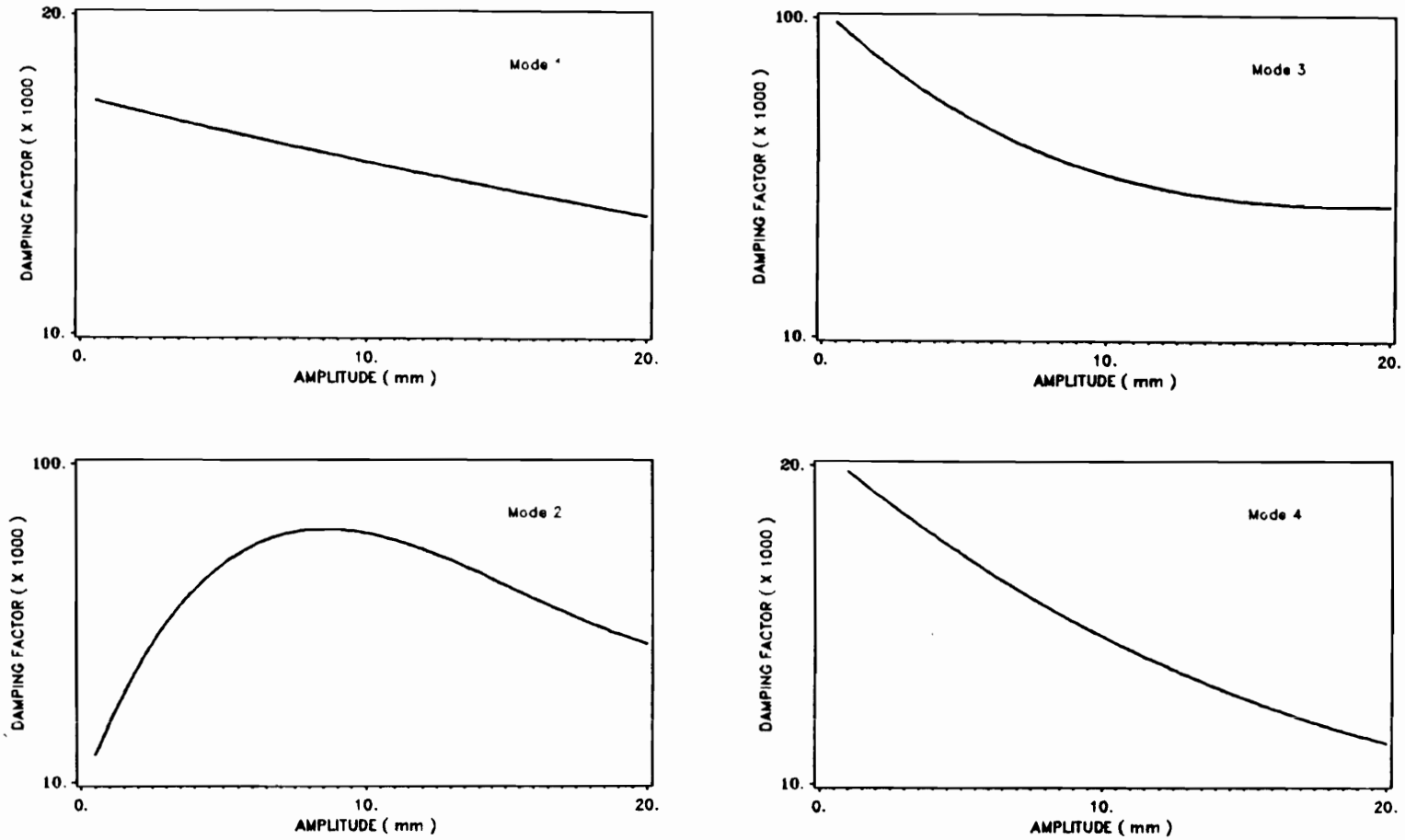


Figure 4.3.2 Variation of damping coefficient measured in the Ground vibration test with vibration amplitude of a sweptback wing configuration.

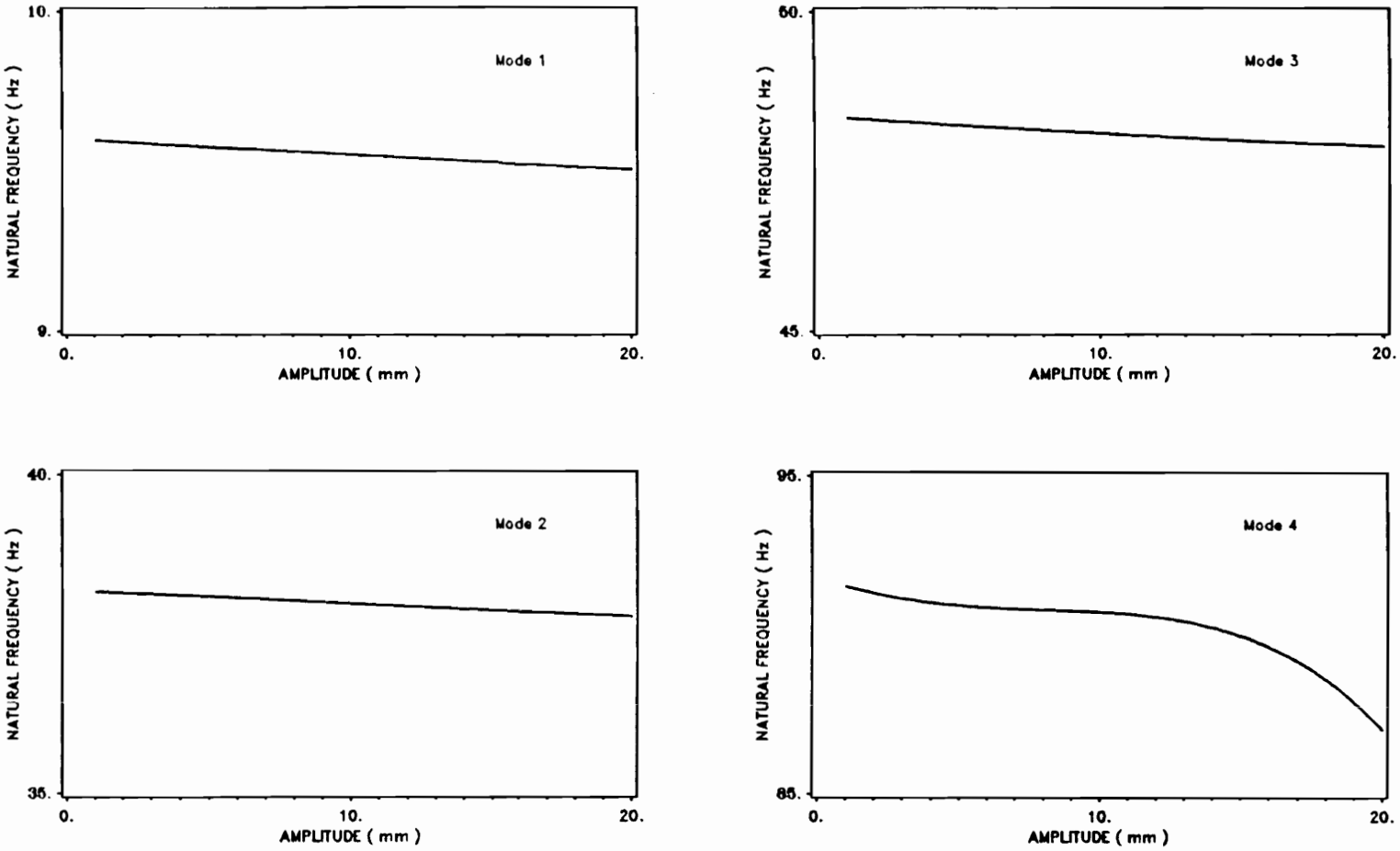


Figure 4.3.1 Variation of natural frequency measured in Ground vibration test with vibration amplitude of a sweptback wing configuration.

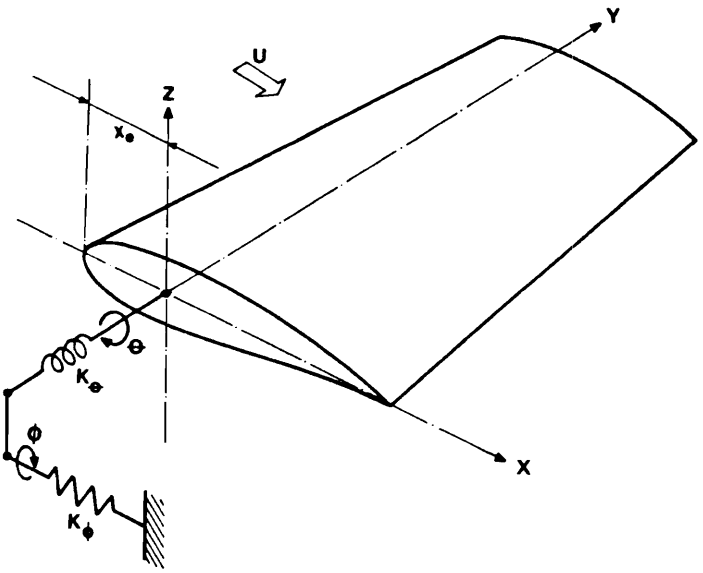


Figure 4.4.1 Three-dimensional elastic wing model with rolling, $K_\phi$, and torsion, $K_\theta$, spring attachment at the root.

# Chapter 5

# Solutions of the Aeroelastic Equations

In Chapter 2, we derived the aeroelastic equations of motion for two different models of wing structures, namely : (i) a two-dimensional typical section model and (ii) a three-dimensional wing model. Two and three-dimensional unsteady transonic flow calculations are described in Chapter 3, which also include the computation of the generalized unsteady aerodynamic load vector / matrix. The possible structural nonlinearities effects and the way of taking them into account in flutter analyses of a system are discussed in Chapter 4.

In this chapter, solutions of the flutter equations given in Chapter 2, for systems with linear structures, and in Section 4.4 , for systems with a nonlinear structures, are discussed . Numerical calculations are performed using both the two and three-dimensional wing models , and with and without structural nonlinearities. Comparisons are made between the numerical results obtained using present method with

data from the wind tunnel experiments and other previously available numerical calculations.

## 5.1 Overview

In the transonic regime, the strongly nonlinear nature of aerodynamic flow equations make it impossible to solve the aerodynamic and structural equations independently. This is unlike in the subsonic and supersonic cases, where the governing equations of motion are linear and the aerodynamic forces can be written as a linear function of the body motion. For transonic flows, the superposition principle is not, in general, applicable in this case and a coupled set of aerodynamic and structural equations have to be solved simultaneously in order to obtain the aeroelastic response and stability boundaries of a system.

In the aeroelastic equation given by Eq. [2.1.7] , the unsteady aerodynamic force coefficients, $C_l$ and $C_m$, in the transonic flow are nonlinear functions of airfoil displacements. The position of the airfoil at every instant of time is required in the calculation of the aerodynamic force coefficients. However, the displacement of the airfoil depends on the unsteady aerodynamic pressure distribution over the airfoil. So, the solution of the aeroelastic equation have to be carried out iteratively by integrating the structural terms and aerodynamic terms simultaneously in time. This type of solution needs a large amount of computer time, since at every time step, a complete flow field calculation has to be performed.

But when the amplitude of the motion is small, such that the perturbation of the flow parameters at any time can be assumed to be a linear function of the flow parameters at that instant, then the superposition principle of the aerodynamic load may be applied. The assumption of the load superposition makes it possible to transform the aeroelastic equation , Eq. [2.1.7] , into an eigenvalue type of equation in frequency domain, such as given by Eq. [2.1.8] . As will be described later in the following section, the solution of this equation is easier and faster to obtain as compared to a time marching solution of Eq. [2.1.7] . These type of solutions, however, have disadvantages, such as the lack of details of the response and the restriction on the amplitude of the motion. But, for preliminary calculation purposes, where detailed response characteristics are not needed, the eigenvalue type of solution may still be of considerable value.

In the next two sections, both of the solution methods, i.e. the time marching type of solution and the eigevalue type of solution, are described.

## 5.2 Time marching solutions

Because of the large amount of CPU time and computer storage needed to perform this calculation, only the problems dealing with the two-dimensional typical section model, as represented by Eqs. [2.1.7] and [4.4.4] , are solved with the time marching approach. In this approach, the aeroelastic responses are computed by integrating the structure and aerodynamic terms in Eqs. [2.1.7] and [4.4.4] simultaneously. It was shown, Ref. 94 , that this step - by - step time integration solution, in

general, requires a time-step which is based on the accuracy needs for the the computation of the unsteady aerodynamic load coefficients. Since this required time-step is usually much smaller than the requirement for stable integration of the structural response, there is no need to use a complicated time integration scheme in this solution. Two direct integration methods were used in this study, namely : the Newmark - $\beta$ and the Wilson - $\theta$ methods, Ref. 55 . The advantage of these methods is that these are both simple and easy to code.

Before we proceed to derive the solution of Eq. [2.1.7] , we rewrite this equation into the form

$$[M]\{u''\} + [C]\{u'\} + [K]\{u\} = \{R\} \qquad [5.2.1]$$

where { u } is the generalized displacement vector which consists of $\xi$ and $\alpha$ and { R } is the generalized aerodynamic forces vector which is defined as the right hand side of Eq. [2.1.7] .

In the Wilson - $\theta$ method, it is assumed that the variation of acceleration from time t to time $(t + \theta\Delta t)$ , where $\theta \geq 1.0$ , is linear. At time $(t + \theta\Delta t)$ , then we have

$$u'_{t+\theta\Delta t} = u'_t + \left(\frac{\theta\Delta t}{2}\right)(u''_{t+\theta\Delta t} + u''_t)$$

$$u_{t+\theta\Delta t} = u_t + (\theta\Delta t)u'_t + \left(\frac{\theta^2\Delta t^2}{6}\right)(u''_{t+\theta\Delta t} + 2u''_t) \qquad [5.2.2]$$

Writing the aeroelastic equation at time $t + \theta\Delta t$ as,

$$[M]\, u''_{t+\theta\Delta t} + [C]\, u'_{t+\theta\Delta t} + [K]\, u_{t+\theta\Delta t} = \{R_{t+\theta\Delta t}\}$$

and substituting $u'_{t+\theta\Delta t}$ and $u_{t+\theta\Delta t}$ expressions from Eq. [5.2.2] into this equation, yields to equation,

$$[A]\, u''_{t+\theta\Delta t} = \{\bar{R}_{t+\theta\Delta t}\} \qquad [5.2.3]$$

where

$$[A] = [M] + a_0 [C] + a_1 [K]$$

$$\{\bar{R}\} = \{\bar{R}_{t+\theta\Delta t}\} - [C]\{a_0 u''_t + u'_t\} - [K]\{u_t + 2a_0 u'_t + 2a_1 u''_t\}$$

with $a_0 = \dfrac{\theta\Delta t}{2}$ and $a_1 = \dfrac{\theta^2\Delta t^2}{6}$

The solution is started with the computation of the unsteady aerodynamic load vector, { R } , at time t = 0 , in which the surface flow tangency condition is derived from the initial position of the wing surface. Having the aerodynamic load calculated, the vector $u''_{t+\theta\Delta t}$ is then computed from Eq. [5.2.3] . The next step is to solve Eq. [5.2.2] for $u'_{t+\theta\Delta t}$ and $u_{t+\theta\Delta t}$ using all quantities previously computed. Using the new values of $u'_{t+\theta\Delta t}$ and $u_{t+\theta\Delta t}$ , the unsteady aerodynamic load vector is updated ( in which case a new surface boundary conditions are applied in the flow computation ) and then the integration can be proceeded to the next time level. The value of $\theta$ used in the integration was 1.39.

The solution procedure in Newmark - $\beta$ method is similar to the Wilson - $\theta$ method with the only difference is that the value of $\theta = 1$ is used in the Newmark - $\beta$ method. The time step $\Delta t$ for these two methods is chosen based on the maximum time step allowed for accurate flow field solutions, which is equal to 0.1 . Within this time step value, it was observed in this study that these direct integration schemes are nu-

merically stable. This was verified by repeating a response calculation for different time steps.

In the case where one of the spring is nonlinear, integration is performed on Eq. [4.4.4] , which include the stiffness variation with respect to the motion amplitude, instead of Eq. [2.1.7] . The integration procedure is similar to the one applied to Eq. [2.1.7] as explained above, with one additional step, i.e. at every time step a new stiffness coefficient is used in the integration The effective stiffness coefficients are computed from Eq. [4.4.1] based on the new spring displacements , $u_{t+\theta\Delta t}$ . As long as the amplitude of the displacement is not excessively large, this simple integration procedure still gives stable solution for maximum time step of 0.1 .

For certain combination of values of Mach number, M , reduced frequency, k , and airfoil to air mass density ratio , $\mu$ , the flutter boundary can be defined as a point where the system has a neutrally stable response.

## 5.3 Solutions in frequency domain

As stated earlier, the solution in the frequency domain is much easier and faster to obtain. But several assumptions have to be made regarding the motion of the structure and the unsteady aerodynamic force calculations, as described in Section 2.2 and Section 3.6 , which will be restated here for clarity. The first important assumption that had been made is that the amplitude of the motion is small so that both

modal superposition and unsteady aerodynamic load superposition principle are valid . The second assumption is related to the flow modeling. It is assumed that the transonic flow pattern is not complex, i.e. there is no strong shock or strong shock wave boundary-layer interaction which can induce flow separation in the flow field. As a result, the transonic small disturbance theory can be used to represent flow phenomena involved.

Applying the first assumption, the aeroelastic equation of motion can be transformed into matrix eigenvalue form as given by Eqs. [2.1.8] and [2.2.3] for system with linear structure , and by Eqs. [4.4.4] and [4.4.6] for system with structural nonlinearities. Two methods are used to solve these equations : (i) the U-g method and (ii) the root - locus method . The U-g method, Ref. 1 , is applied to obtained the flutter solution of two-dimensional typical section wing model , represented by Eqs. [2.1.8] and [4.4.4] . For the three-dimensional finite-state wing model, the equation of motion , Eqs. [2.2.3] and [4.4.6] , are transformed further into the Laplace plane, as expressed by Eqs. [2.2.5] and [4.4.7] , and solved using the root - locus method . The purpose of this transformation, as mentioned earlier, is to avoid working with complex matrices of the aerodynamic load terms . And also this representation of the problem makes it easier to incorporate a control law into the problem, since the control laws are often represented in the Laplace plane.

### *5.3.1 The U - g method*

In the U-g method, a new parameter g , called the artificial damping coefficient, is introduced , and is regarded as one of the unknowns. The values of this artificial damping coefficient are assumed to be proportional to the values of the stiffness coefficient but has a phase shift of 90° with respect to the displacement vector. With the introduction of this parameter, the variable $\lambda$ in Eqs. [2.1.8] and [4.4.4] mentioned earlier, is redefined as

$$\lambda = \mu k^2 (1 + ig) \qquad [5.3.1]$$

For a particular value of reduced frequency , k , a certain value of Mach number, M , and mass density ratio $\mu$ the flutter equation , Eq. [2.1.8] , is solved for the complex eigenvalues, $\lambda$ . From the values of $\lambda$ , then the values of g are computed using the relation given by Eq. [5.3.1] ,

$$g = \frac{\text{real part of } \lambda}{\text{imaginary part of } \lambda}$$

Following these computational steps for several different values of k , in the range where flutter is suspected to occur, a plot of artificial damping , g , versus reduced frequency , k , is obtained. Using this curve, the flutter reduced frequency is defined as the value of the reduced frequency for which the value of the artificial damping is equal to zero. A similar plot of $\overline{U}$ , the normalized free-stream velocity, versus artificial damping coefficient can also be generated. The normalized free-stream velocity, $\overline{U} = U/\omega c$ , is obtained from the following relation which is derived from the definition of k ,

$$\overline{U} = \frac{1}{k} = \frac{1}{\mu}\sqrt{\frac{1}{\text{real part of } \lambda}} \qquad [5.3.2]$$

Similarly, the flutter speed is defined as the value of $\overline{U}$ at which the artificial damping coefficient vanishes. The flutter computations are carried out for several combination of the Mach number and the mass density ratio.

In a case when structural nonlinearity exists in either one of the springs, Eq. [4.4.4] , the flutter equation now has $\delta$ as a parameter, which in it self is a function of the motion amplitude. The flutter speed or flutter reduced frequency is first evaluated numerically as a function of the effective stiffness coefficient, $\delta$ . Then, from the relation of $\delta$ with the motion amplitude, as given by Eq. [4.4.1] , the flutter speed was evaluated as a function of the motion amplitude.

### *5.3.2 The root - locus method*

The finite state aeroelastic equation, Eqs. [2.2.5] and [4.4.7] are solved using the root locus analysis which is very similar to the U-g method. In the U-g method, we deal with complex matrices ( since the generalized aerodynamic matrix is a complex matrix ). In finite state aerodynamic modeling ( see Appendices A and B ), the generalized aerodynamic forces are transformed into the Laplace plane ( so are the structural terms ) which make it possible to write the whole equation in terms of real matrices , Eq. [2.2.5] . For a fixed value of Mach number, dynamic pressure, $\overline{q}$ , and flight velocity, $U$ , the eigenvalues of Eq. [2.2.5] are the roots of the characteristic

flutter equation of the system. Since the elements of matrix [ H ] varies with dynamic pressure ( for a constant Mach number ), a root locus illustrating the variation of the eigenvalues with dynamic pressure can be constructed for each Mach number. This has to be noted that since for a given Mach number, the flight velocity varies somewhat because of the change in the speed of sound with altitude, it is assumed in this calculation that the Mach number fixes the value of U .

The flutter point is defined as a point where the root crosses from the stable region ( the eigenvalue has a negative real part ) into the unstable region ( eigenvalue has a positive real part ). Since the modal damping is proportional to

$$g = \tan\left(\frac{\text{real part of the root}}{\text{imaginary part of the root}}\right)$$

the same analytical results presented as root locus plots can be presented in the similar form of damping versus dynamic pressure as in the U-g method. The flutter dynamic pressure , $\bar{q}_f$ , at certain value of free-stream Mach number and mass density ratio, is defined as the dynamic pressure at which the damping coefficients is equal to zero.

For the case where one of the attachment spring at the wing root is nonlinear, the root locus solution is applied to solve Eq. [4.4.7] . For specific values of equivalent stiffness coefficients , $\bar{K}_\theta$ and $\bar{K}_\phi$ the standard root locus may be used to solve the flutter equation. From the solution of the linearized equation, the flutter dynamic pressure for varying values of root - spring equivalent stiffness or equivalent uncoupled frequency in rolling motion, $\bar{\omega}_\theta$ and $\bar{\omega}_\phi$ are obtained. And also the relative root displacements at flutter are defined from the eigenvector of the system. Curve of the

dynamic pressure versus equivalent stiffness and motion amplitude versus equivalent stiffness are obtained.

For nonlinear springs, the initial step is to select the magnitude of the root displacement ( either root - roll , $a_l$ , or root - pitch , $a_p$ ) and the equivalent spring stiffness associated with that displacement. Assuming that we have nonlinearity only in rolling spring, we select $a_l$ and $\overline{K}_\phi$ . For a given magnitude of $a_l$ , the values of $\delta_\phi$ is calculated from the Eq. [4.4.1] . This is followed by obtaining the spring stiffness using the relation

$$K_\phi = \overline{K}_\phi / \delta_\phi$$

For selected $\overline{K}_\phi$ values, the flutter dynamic pressures is obtained from the $\overline{K}_\phi$ versus dynamic pressure curve. This procedure leads to the result of flutter dynamic pressure as function of the spring stiffness coefficient. By using the relation between the equivalent stiffness coefficients and the motion amplitude, the flutter dynamic pressure-displacement amplitude relation can be generated. Calculations can also be performed in term of equivalent natural frequencies of the spring, $\overline{\omega}_\phi$ , by using the relationships

$$\omega_\phi = [K_\phi / I_\phi]^{\frac{1}{2}} \qquad \text{and} \quad \overline{\omega}_\phi = \sqrt{\delta_\phi}\, \omega_\phi$$

## 5.4 Results for two-dimensional airfoil section wing model

The two - dimensional typical section wing model for flutter calculation is illustrated in Fig. 2.1.1 . The airfoil has a NACA64A006 cross section, with radius of gyration about elastic axis , $r_\alpha$ , equal to 0.5 . The airfoil is assumed to pitch about one-quarter chord axis , a = -0.5 , and the mass center was assumed be at $x_\alpha b$ aft the elastic ( pitch ) axis where $x_\alpha = 0.25$ . The generalized aerodynamic coefficients are calculated following the procedure described in Section 3.6.1 and are plotted in Fig. 3.6.4 .

### *5.4.1 Airfoil with linear spring*

The curves of flutter speed and corresponding reduced frequency versus the airfoil - mass density ratio, $\mu$ , were obtained for the spring frequency ratios , $\omega_h / \omega_\alpha$ equal to 0.1 and 0.15 using U-g method. The curves are shown in Figs. 5.4.1 and 5.4.2 for free-stream Mach number M = 0.85 . Similar curves were also obtained for M = 0.80, but are not shown here. At both Mach numbers, the same general trend is observed. The flutter speed increases steadily with $\mu$ . The curves become less steep for a higher frequency ratio. For a given value of $\mu$ , the flutter speed is lower at a higher frequency ratio. From Fig. 5.4.2 it can be observed that the flutter reduced frequency increases as $\mu$ decreases and the curves are higher for higher frequency ratios.

Comparison with the results obtained by Yang, et. al. , ref. 94 , which used LTRAN2 Code to calculate the aerodynamic forces, are generally in good agreement. In the solution given in that reference, the generalized aerodynamic coefficients are calculated using the indicial method based on the low frequency TSD equation. The results are in less agreement for lower values of $\mu$ and higher values of frequency ratio. The main reason for this is that at lower values of $\mu$ , flutter occur at a higher value of reduced frequency which is out of the range of validity for the low frequency approximation ( around $k < 0.2$ ) used. Another reason is, as mentioned in Section 3.4 , the differences in the position and the strength of the shocks predicted by the two solutions and some other differences, such as the mesh distribution, numerical procedures etc.

Time marching solutions are performed to assess the accuracy of the frequency domain, i. e. U-g method , solutions. Before the integration is performed, the aerodynamic equation was integrated in time for three or four cycles by forcing a sinusoidal pitching displacement with amplitude of 0.01 rad. in order to avoid the aerodynamic transient response in the flow field. The free motion was started at the end of the fourth cycle, after the aerodynamic force response became periodic, by simultaneously integrating the structural and aerodynamic equation. The initial conditions, at $t=0$ , used for the free motion $\alpha(0)=0$ , $\alpha'(0) = 0.01$ , $\xi(0) = 0$ and $\xi'(0) = 0$ . The responses were computed for free-stream Mach numbers equal to 0.80 and 0.85. By varying the airfoil - air mass density ratio, we could get a stable, neutrally stable or an unstable response. Figure 5.4.3 shows the response at $k = 0.10$ , $M = 0.85$ and $\mu = 70$ , in which the response grows very rapidly ( unstable response ) . As the value of the mass density ratio is increased, the aerodynamic damping become higher which leads to a neutrally stable or converged

response , as shown in Fig. 5.4.4 . At $\mu = 220$ , the response is highly damped in which case the motion amplitude decreases very quickly. The values of aeroelastic parameters for the neutrally stable condition at M = 0.80 were selected from the point on the flutter speed curve in Fig. 5.4.1 for a value of k = 0.1 . The corresponding values of $\mu$ and $\overline{U}$ , the free-stream velocity , were equal to 97.5 and 6.15 , respectively. The system response for this aeroelastic parameter combination is shown in Fig. 5.4.5 . The value of $\mu$ that gives the neutrally stable response is obtained by interpolating the values from two response, i.e. at $\mu = 90$ , where the response was slightly divergent and at $\mu = 110$ , where the response was convergent . From this interpolation, the neutrally stable response was found to be associated with the value of $\mu = 94.5$ , which is about 3 % lower than the result obtained using the U-g method. These two results show that the frequency domain solution for this specific problem , is as good as the more expensive time domain solution in predicting the flutter boundary of the system.

### 5.4.2 *Airfoil with nonlinear spring*

Flutter calculations were performed for the same model as described above but with nonlinear torsional spring. Two types of concentrated nonlinearities are investigated in this study : (i) preload and (ii) freeplay nonlinearity. The effective stiffness coefficients of this spring as function of motion amplitude are computed in Section 4.2 using both the first and second order approximations. Flutter calculations were carried out in the frequency domain using U-g method. In all cases the mass density ratio , $\mu$ , is chosen to be equal to 100. Flutter reduced frequency variations with

respect to the pitching motion amplitude for each type of the nonlinearity were generated.

Figure 5.4.6 shows the normalized flutter reduced frequency variation, for the torsional spring with preload nonlinearity, at three different free-stream Mach numbers, M = 0.70 , 0.80 and 0.85 ; for $\omega_h / \omega_\alpha = 0.1$ and $\delta s / \delta p = 4$ . The region below the curve is unstable and above is stable. The flutter reduced frequency is normalized with respect to the flutter reduced frequency of linear system , ( i.e. $\delta s = 0$ ) . For small initial pitching displacement, $a/\delta p < 1$ , the system oscillated on the linear arm of the spring and, at reduced frequency above $k_{linear}$ , was stable. For slightly larger displacements, the oscillation entered the region of the dead-band ( the region of width $\delta s$ where the slope of the load - displacement curve is equal to zero ) so that the effective torsional stiffness was reduced. In this case, a decrease in torsional stiffness was destabilizing and limited amplitude flutter occurred. This should correspond to the so-called 'mild-flutter' in the experimental investigation of nonlinear flutter of an airfoil section model by Woolston, et. al. , as reported in Ref. 51 . As the initial pitching displacements were increased still further, the oscillations covered more and more of the dead-band region. A further destabilizing reduction in stiffness occurred, and the oscillation should be stable but with rapidly increasing amplitudes, corresponding to the 'violent flutter' . It can be observed that for each value of Mach number, there is a maximum flutter reduced frequency ( i.e. a minimum flutter speed , see relation in Eq. [5.3.2] ) , above which the system is stable with regard to all pitching amplitudes, a . This minimum flutter speed corresponds to the weakest torsional stiffness, which occurs at $a = \delta p + \delta s$ . It can be seen that the maximum flutter reduced frequency decreases as the Mach number increases, i.e. the minimum flutter speed increases as the Mach number increases. This result

indicates good agreement, qualitatively, with both the experimental and analog results given in Refs. 51,53 .

Comparison is also made between the flutter results obtained from the calculation using the first and second order approximations for the effective stiffness coefficients of the torsional spring for M = 0.70 and are shown in Fig. 5.4.7 . The first order approximation gives a smaller stiffness reduction ( see Fig. 4.2.1 ) which leads to a smaller flutter reduced frequency increase and a smaller flutter speed decrease. The difference in the maximum value of the flutter reduced frequency between the two solutions is about 25 % , a number that can not be ignored.

Next, the effects of the freeplay nonlinearity was investigated. The aeroelastic parameters of the model used in the calculations are the same as the ones used in the previous example. The torsional spring is considered to have a freeplay nonlinearity of amplitude $\delta s = 0.5°$ . The effective stiffness coefficients for this spring are given in Fig. 4.2.3 . As shown in Fig. 5.4.8 , the region below the curve is unstable and that above the curve is stable. The flutter speeds are normalized with respect to the flutter speed of the corresponding linear system , $\delta s = 0$ and $\omega_h / \omega_\alpha = 0.5$ . For small amplitudes, the airfoil is initially floating in the region of freeplay, and the oscillations are confined within this region where the effective stiffness value of $\omega_\alpha = 0$ ( $\overline{K}_\alpha = 0$ ) . With $\overline{K}_\alpha$ equal to zero, airfoil system is essentially modeled by a one degree of freedom system in plunging. As the amplitude of the pitching displacement is increased, the oscillations extend beyond the region of freeplay to a proportionate amount, and the effective values of both $\overline{K}_\alpha$ and $\overline{\omega}_\alpha$ increase. In the linear system, an increase in $\omega_\alpha$ ( which means a decrease in ratio value, $\omega_h / \omega_\alpha$ , for a constant value of $\omega_h$ ) , means a decrease in flutter reduced frequency and in-

crease in flutter speed , see Figs. 5.4.1 and 5.4.2 , so that in this case the flutter boundary shifts to a lower flutter reduced frequency. If sufficiently high initial pitching displacements could be attained, the flutter boundaries would become asymptotic to the linear flutter reduced frequency.

Further study of the nonlinearity effects on the flutter boundary is performed by investigating the variation of the airfoil to air mass density ratio , $\mu$ , that gives a neutrally stable response ( flutter boundary ) with respect to the motion amplitude. The aeroelastic model is the same as the one used in previous calculations, with the torsional spring having preload or freeplay nonlinearity. The flutter solution was carried out in the time domain by integrating the aeroelastic equation, Eq. [4.4.4] , using the time integration scheme described in Section 5.2 .

Figure 5.4.9 shows the response of the linear system and system with torsional spring having a preload nonlinearity, $\delta s / \delta p = 1$ and $\delta p = 0.0275$ rad . At M = 0.85 , $\mu = 94.5$ ( where the linear calculation gives a neutrally stable response ) , the linear system, as expected , exhibits a neutrally stable response. Meanwhile, in the nonlinear system , the decrease in the torsional stiffness increases the amplitude of the displacement and also increases the aerodynamic damping and thus leading to a slightly converged response. The variation of the mass density ratio with respect to the amplitude ratio of pitching motion , ( $a/\delta p$ ) in the preload spring and ( $\delta s/a$ ) in the freeplay spring, are given in Fig. 5.4.10 .

In preload cases, the mass density ratio is normalized with the value of the linear system , $\delta s = 0$ . The flutter mass density ratio steadily increases as the amplitude of the pitching motion increases, i.e. flutter occurs at a higher values of $\mu$ . For a

larger value of $\delta s/\delta p$ ratio, the increase is steeper, because of a larger reduction in the torsional spring stiffness coefficient.

For a spring with freeplay nonlinearity, as the amplitude ratio increases ( for a constant $\delta s$ and increasing a ) , the effective values of $K_*$ and $\omega_*$ also increase and shift the flutter boundary to a lower value of $\mu$ . This can be explained using the result given in Fig. 5.4.1 . In a linear system, an increase in $\omega_*$ means a decrease in the value of $\omega_h/\omega_*$ for a constant value of ( $\omega_h$ ) , leading to the flutter at a lower value of the mass density ratio for an assumed flutter speed. For a nonlinear system, this analogy translates as a shifts of the flutter boundary towards a lower value of $\mu$ .

## 5.5 Results for three-dimensional wing model

Three-dimensional flutter calculations are performed on a 45° swept wing which is an AGARD standard aeroelastic configuration, Ref. 86 . The geometry of the wing configuration was described in Section 3.6.2 . A plan view of the wing is shown in Fig. 5.5.1 and the oblique projections of the four natural mode shapes and its displacement contours used in the flutter calculation are illustrated in Fig. 5.5.2 . This wing series was tested in the Transonic Dynamic Tunnel at NASA Langley Research Center and the results are presented in Ref. 13 .

The unsteady generalized aerodynamic forces ( GAF ) for the flutter calculation are computed using the pulse transfer function analysis ( Section 3.6.2 ). To assess the accuracy of this method for transonic application, unsteady GAF's were obtained for the wing with thickness included, at free-stream Mach number 0.9 and mean angle

of attack 0° . The accuracy of these forces is determined by making comparisons with similar results computed using harmonic oscillation method ( Section 3.6.1 ). Comparison of the $A_{12}$ and $A_{22}$ of the GAF are given in Figs. 3.6.8 and 3.6.9 , respectively. The two sets of results are in very good agreement, which validates the pulse transfer function method for application to transonic flow problems.

The flutter calculations were carried out using the root - locus method. The aeroelastic equations of motion are transformed into the Laplace plane , yielding the equation of the form given by Eqs. [2.2.5] and [4.4.7]. The GAF, at finite number of values of reduced frequency, k , are approximated by a rational function as defined by Eq. [A.5], see Appendix A , before it was transformed into Laplace plane . The accuracy of the approximation may be observed from several results presented in Figs. 5.5.3 (a-d), for Mach number 0.9 . It is noted that $A_{i,j}$ is defined as the generalized unsteady aerodynamic forces coefficient from the pressure induced by mode j acting through the displacement of mode i . The real and imaginary parts of $A_{i,j}$ at each value of k are plotted. The continuous lines represent the continuous values obtained from the interpolation function. The parameters $\beta_1$ , $\beta_2$ , $\beta_3$ and $\beta_4$ in the interpolation function are chosen such that the interpolation error is minimum. It was found that the best possible values for these parameters are 0.80 , 0.40, 0.20 and 0.025 , respectively. It can be seen that this interpolation function gives very good approximation for each $A_{i,j}$ shown. Results for other $A_{i,j}$ elements show similarly good agreement between the data points and interpolation function and are not shown. It was also found that the interpolation is not very sensitive to the small changes in values of the parameter $\beta_i$ . For some $A_{i,j}$ , 5 % changes in the $\beta_i$ values do not change the overall interpolation error. Similar conclusions are also given by Roger in Ref. 65 .

### 5.5.1 *System with linear springs*

Aeroelastic stability and flutter results are presented to investigate the aeroelastic characteristic of the wing in transonic speeds. Calculations were performed for several values of free-stream Mach number and mass density ratio , $\mu$ . These values are chosen following the values that were obtained in the wind - tunnel experiment given in Ref. 13 , so that the comparison of the results can be made. Four flutter calculations were performed, for Mach number M = 0.499 , 0.80 , 0.90 and 0.954 with the corresponding values of mass density ratio $\mu$ = 33.465 , 143.92 , 143.92 and 225.82 , respectively. Root - loci plot for M = 0.8 and $\mu$ = 143.92 are presented in Fig. 5.5.4. In this figure only two dominant roots are plotted, which represent the roots associated with the first bending and first torsion modes. Each point represent the root for certain value of dynamic pressure , $\bar{q} = [U/(b\omega_\alpha\sqrt{\mu})]^{1/2}$ , where $\omega_\alpha$ is the first torsion natural frequency. The increment in dynamic pressure shown in the figure is $\Delta\bar{q} = 0.3$ . At this Mach number value, the curve indicates a classical bending - torsion type of flutter behavior. Here the first torsion branch moves to the left in the stable left-half plane, with increasing dynamic pressure. Meanwhile, the bending dominated branch moves slowly into the unstable plane and become the flutter mode. The nondimensional flutter speed, $\bar{U} = U/b\omega_\alpha\sqrt{\mu}$ , is found equal to 0.39495 . The experimental value for the flutter speed at this Mach number given in Ref. 13 , is 0.38375 . This value is about 3% lower as compared to

the value obtained from the present calculation. At the other three Mach numbers, similar behavior was observed.

The plot of damping coefficients versus dynamic pressure is given in Fig. 5.5.5 . The bending dominated flutter is found to occur at dynamic pressure equal to $\bar{q} = 0.26211$ . The variation of the nondimensional flutter speed, $\bar{U}$ , with free-stream Mach number is shown in Fig. 5.5.6 . The present results are compared with the wind - tunnel data. The experimental data are all for WEAK3 wing model tested in air. It can be observed from this plot, that the experimental data defines a typical transonic flutter 'dip' , with the bottom of the dip occurs near M = 1.072 . The flutter speed at this bottom can not be predicted in present study, since the flow solution developed in this study is limited only for free-stream Mach number less than one. In the subsonic Mach number range, M = 0.499 , present calculation predict a slightly unconservative flutter speed with about 3.5% difference compared to the experimental data. The comparison at three Mach numbers in transonic range still shows a good agreement. A large decrease was observed in the flutter speed between the free-stream Mach number 0.9 and 0.954 . Between these two values, the flutter speed decreases by 20% . This large reduction is due to the nonlinear flow effects, since a weak shock already appears in the wing tip region at M = 0.954 . The involvement of the shock in the flow field cause a lifting pressure jump due to the change in the overall pressure distribution over the wing surface. As the free-stream Mach number increases, the corresponding flutter reduced frequency decreases from k = 0.3 at M = 0.499 to the value of k = 0.08 at M = 0.954 .

Bennett, et al., Refs. 96,97 , presented aeroelastic results for the same wing configuration. These results were obtained using the CAP-TSD aeroelastic code developed

at NASA Langley. The computation in CAP-TSD is based on the transonic small disturbance flow equation, and the aeroelastic solutions are obtained by time integration procedure. A good agreement was reported in the flutter boundary obtained from CAP-TSD calculation and the experimental data. Good agreement between the numerical results ( i.e. from the present study and the ones obtained using CAP-TSD ) with the experimental data may be due to the fact that for the wing geometry considered, no strong shock and flow separation are involved. When a strong shock is present in the flow field or when the physical situation is known to involve a separated flow, this level of agreement can be sustained only if the analyses are extended to account for these unmodeled effects.

### 5.5.2 *System with distributed nonlinearity*

The structural distributed nonlinearity effects on the flutter characteristic of the wing configuration are investigated following the procedure described in Section 4.3 . Because of these nonlinearities, wing natural frequencies and damping coefficients are assumed to have a variation with respect to the amplitude of the motion as given in Figs. 4.3.1 and 4.3.2 , respectively. The flutter calculations are performed for several values of amplitude, ranging from 2 mm to 20 mm, which are related to the amplitude of the vibrator used in the ground vibration test of the aircraft structure. The inclusion of the natural frequency and damping coefficient variations leads to the variation of the flutter speed / flutter dynamic pressure with the motion amplitude, as shown in Fig. 5.5.7 . In this plot, the flutter dynamic pressure is normalized with its linear value, $\overline{q}_{linear}$ ( the flutter dynamic pressure for system without structural nonlin-

earity, vibration amplitude = 2 mm ). The calculations were performed for 3 free-stream Mach numbers , M = 0.8 , 0.9 and 0.954 with corresponding values of mass density ratio as given in the previous calculation.

It can be observed that the combined effects of natural frequency and damping coefficients variations, shift the flutter boundary into a lower value of dynamic pressure. The strongest effect was found at M = 0.954, in which case the flutter dynamic pressure decreased by approximately 11% as the amplitude increases to 18mm. Meanwhile, at M = 0.80 and 0.90 this decrease is only about 6 % and 3 % , respectively. Since the dynamic pressure decrease involved the variation of 8 parameters ( 4 for natural frequency and 4 for damping coefficients ) and also the effect of nonlinear aerodynamic damping, it is quite difficult to find a single dominant factor that cause the difference in the decrease of this value for different Mach numbers. In ref. 56 , it was pointed out that the effects of the natural frequency variation on the wing flutter behavior can be regarded as negligible. Hence, the most probable factor that brings different variations of flutter dynamic pressure is the interaction between the structural damping and aerodynamic damping. At M = 0.954 , the aerodynamic force drops significantly ( compared to the value for M = 0.8 or M = 0.9 ) , which is reflected by a lower value of the flutter speed, and aeroelastic solution become more sensitive with the change in the values of the damping and stiffness coefficients.

The variation of the flutter speed / dynamic pressure has an important consideration when the aeroelastic calculation for flutter clearance have to be performed using the structural data ( natural frequencies, mode shapes, generalized mass ) obtained from the ground vibration test. Since the data are usually collected from several tests and the fact that it is impossible to repeat an exactly the same test twice, some variation

in the test parameters ( the most common one is the amplitude of the oscillation given by exciter ) can be expected. If these data, then, are used for flutter calculations, some variation of the kind previously described has to be expected.

### *5.5.3 System with concentrated nonlinearity*

The effects of the concentrated structural nonlinearity are investigated using the wing model shown in Fig. 4.4.1 . This model is similar to the one used by Laurenson in Ref. 55 to investigate the nonlinearity effects on the flutter characteristic of missile control surface. At the root, the wing surface is attached by two springs : a rolling and a torsion spring. In this study, the torsion spring is assumed to have a preload nonlinearity, as illustrated in Fig. 4.1.2 . The aeroelastic equation of motion of the system is given by Eq. [4.4.7]. The effective stiffness coefficients of the torsional spring are computed using second order asymptotic expansion method, and the aeroelastic solutions are obtained by applying the root - locus procedure.

Shown in Fig. 5.5.8 are linearized system results of flutter dynamic pressure, which is normalized with respect to the flutter dynamic pressure of system without spring attachment ( rigid attachment ) , $\bar{q}_o$ , as a function of effective root pitch uncoupled frequency, $\bar{\omega}_\theta$ . The results are for free-stream Mach number of 0.9 , damping coefficients equal to zero and for the following inertia properties of the surface , Ref. 91 :

$I_\theta = 0.0188$ kg.m$^2$ $\quad I_\phi = 0.0080$ kg.m$^2$ $\quad I_{\theta\phi} = 0.0065$ kg.m$^2$

$I_{\theta 1} = -0.0321$ kg.m $\quad I_{\phi 1} = -0.0143$ kg.m

$I_{\theta 2} = -0.0045$ kg.m $\quad I_{\phi 2} = 0.0095$ kg.m

$I_{\theta 3} = -0.0401$ kg.m $\quad I_{\phi 3} = -0.0212$ kg.m

$I_{\theta 4} = -0.0090$ kg.m $\quad I_{\phi 4} = 0.0030$ kg.m

Results presented here are computed for three different effective values of the uncoupled roll frequency, $\overline{\omega}_\phi$ = 60 Hz , 100 Hz and 150 Hz . The flutter boundary for the system is shown in Fig. 5.5.9 . These results are for preload , $\delta p = 0.25°$ , $\delta p/\delta s = 0.5$ , $\overline{\omega}_\phi = 100$ Hz and $\overline{\omega}_\theta = 100$ Hz and 200 Hz . The flutter dynamic pressure is normalized with the value for linear system, $\delta s = 0$ , which are about $0.49\,\overline{q}_o$ and $0.44\,\overline{q}_o$ for $\overline{\omega}_\theta = 100$ Hz and 200 Hz , respectively ( obtained from the result in Fig. 5.5.8 ) . The characteristic of this boundary is similar to the flutter boundary obtained in the two-dimensional typical section model, see Fig. 5.4.6 .

At all pitching amplitudes, the system acts exactly as it would if it were a linear system. A drop in flutter dynamic pressure was observed as the pitch amplitude increases. This type of behavior is indicative of an amplitude - sensitive instability in which an initial disturbance of prescribed amplitude is necessary to produce an unstable system. At amplitude of approximately 0.75° , a distinct change occurs with the boundary, reversing its downward movement. The flutter dynamic pressure continues to increase thereafter and approaches the linear boundary. At that point, the pitch displacement exceeds the deadband region and the beneficial effect of increasing torsional stiffness is immediately evident. For this configuration, three stability region exist, Ref. 98 . Unconditionally stable behavior is present at normalized dynamic pressure below 0.85 ( for $\overline{\omega}_\theta$ value of 200 Hz ). Between this level and the linear value of 1 , an amplitude - sensitive region of stable limit cycle oscillation exists. This can be illustrated by considering the normalized dynamic pressure of 0.9 .

An initial disturbance of amplitude less than 0.48° will allow the system to remain stable. Exceeding this value will cause a limit cycle oscillation to occur with an amplitude of about 1.2° . The region above the curve is the unstable region of divergent flutter. It also can be observed from this figure that for a lower value of effective uncoupled pitch frequency, the unconditionally stable region occurs at higher normalized dynamic pressures and the region of limit cycle oscillation becomes smaller.

The effect of the preload amplitude, $\delta p$ , to the stability boundary is illustrated in Fig. 5.5.10 . The results in this figure were obtained for the values of both $\overline{\omega}_\theta$ and $\overline{\omega}_\phi$ equal to 100 Hz and the $\delta p/\delta s$ ratio of 0.5 and 1 . It is shown that the decrease in flutter dynamic pressure and the width of the limit cycle region become smaller as the amplitude of the preload increases, i.e. the $\delta p/\delta s$ ratio increases. This is due to the increase of the effective stiffness of the torsional spring.

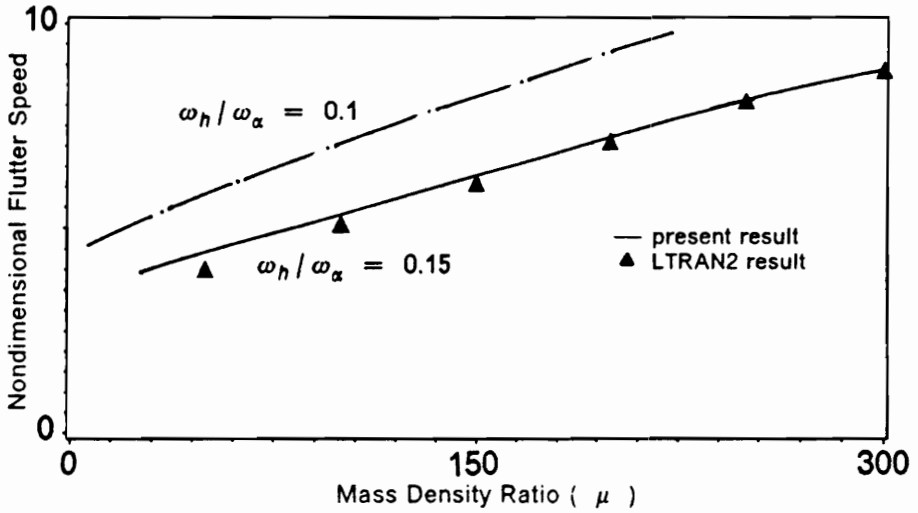


Figure 5.4.1 Effect of mass density ratio on flutter speed of two degree-of-freedom system for various frequency ratio and M = 0.85 .

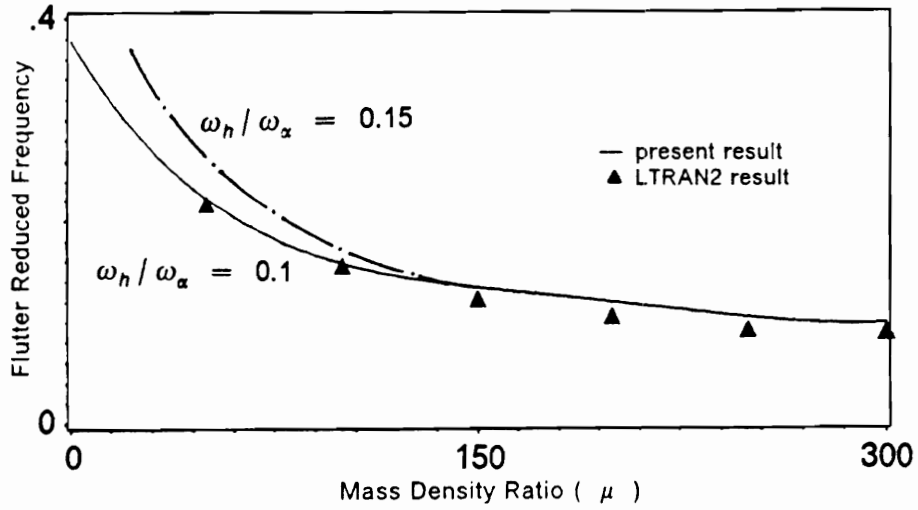


Figure 5.4.2 Effects of mass density ratio on flutter reduced frequency of two degree-of-freedom system for various frequency ratio and M = 0.85

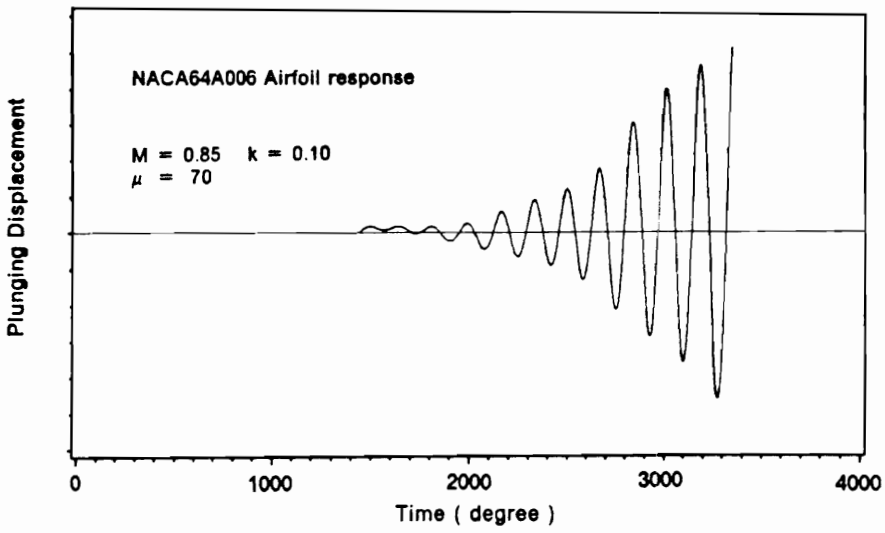


Figure 5.4.3 Unstable pitching response of NACA64A006 airfoil obtained from time integration of aeroelastic equation using Newmark- $\beta$ method.

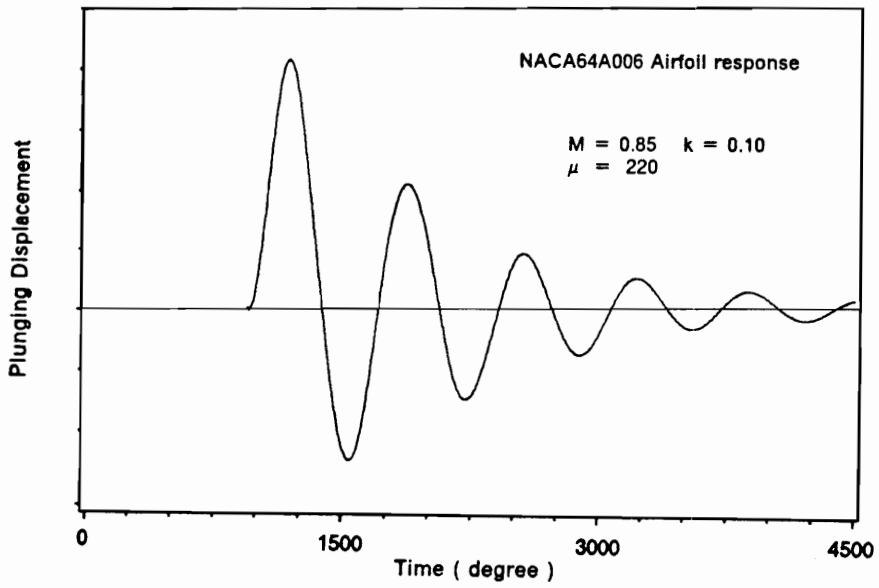


Figure 5.4.4 Stable pitching response of NACA64A006 airfoil obtained from time integration of aeroelastic equation using Newmark- $\beta$ method.

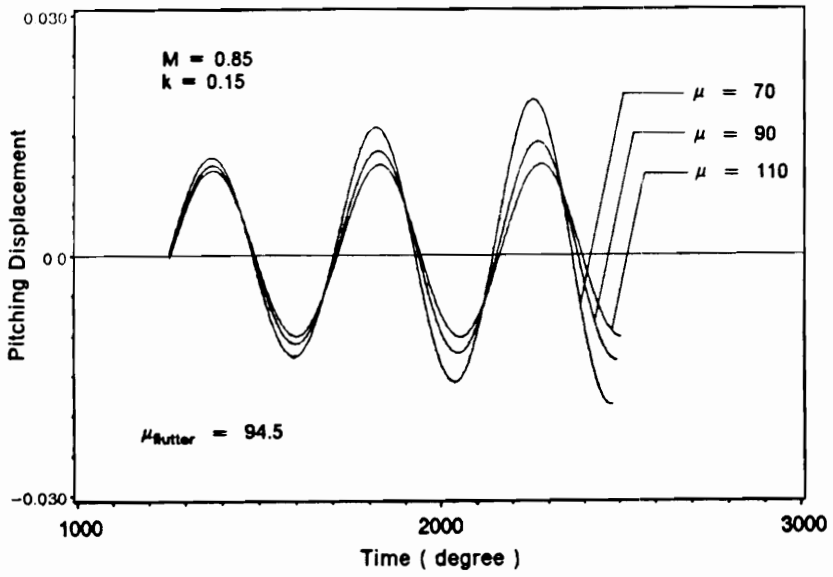


Figure 5.4.5 Neutrally stable pitching response ( flutter boundary ) of NACA64A006 airfoil at mass density ratio , $\mu = 94.5$

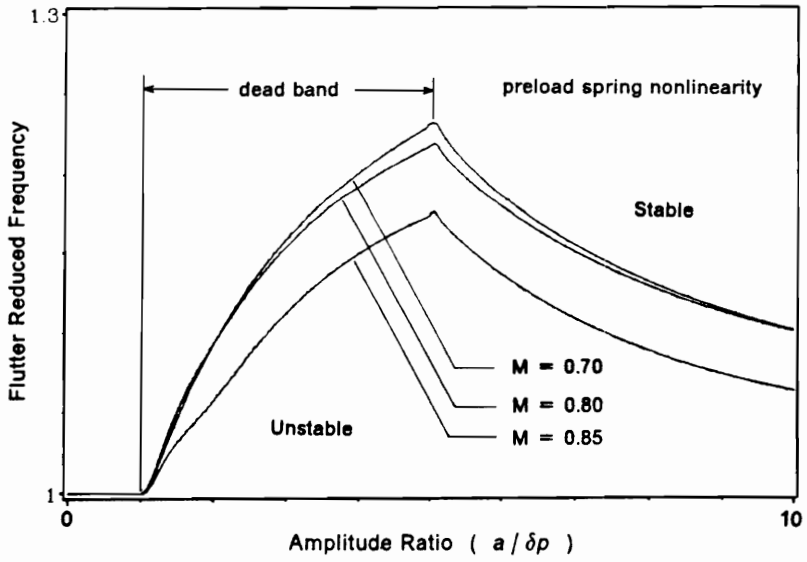


Figure 5.4.6 Effect of oscillation amplitude on the flutter reduced frequency of two degree-of-freedom airfoil system with torsional spring having preload nonlinearity, at various free-stream Mach number.

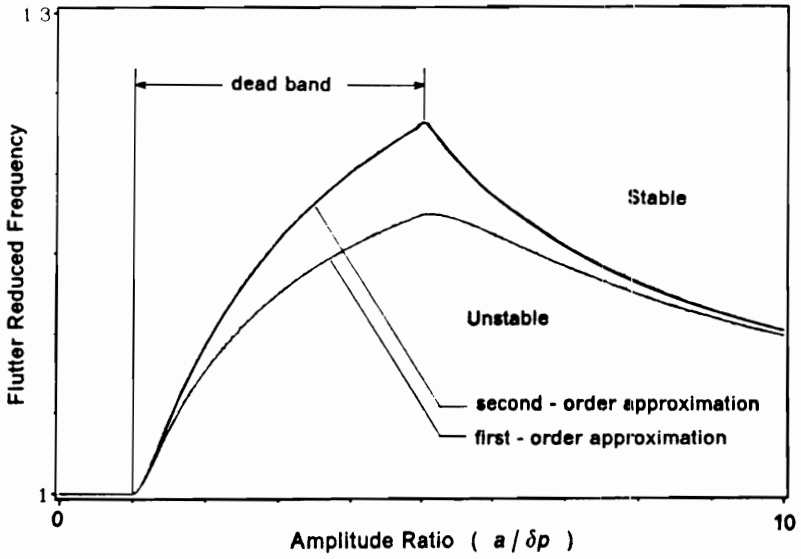


Figure 5.4.7 Comparison of the flutter reduced frequency obtained using first and second order approximation of the spring effective stiffness coefficient.

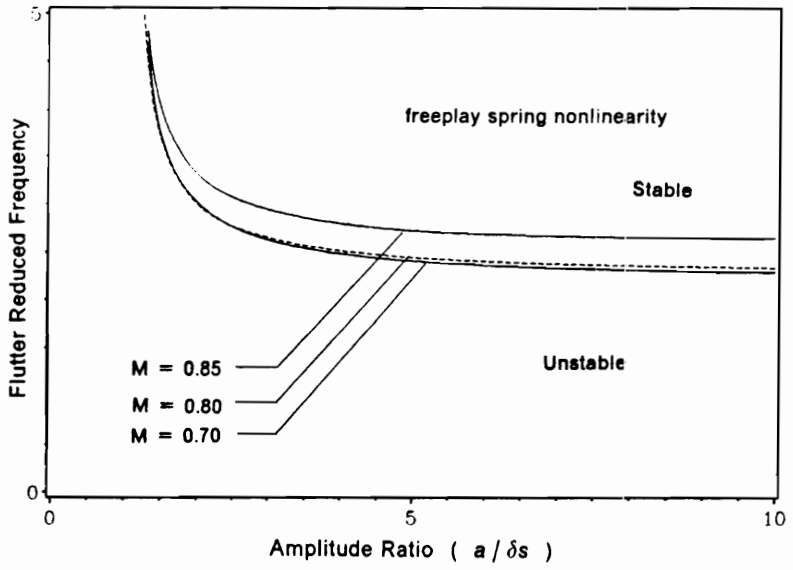


Figure 5.4.8 Effect of freeplay nonlinearity in the torsional spring of two degree-of-freedom system on the flutter reduced frequency of the system, at various free-stream Mach number.

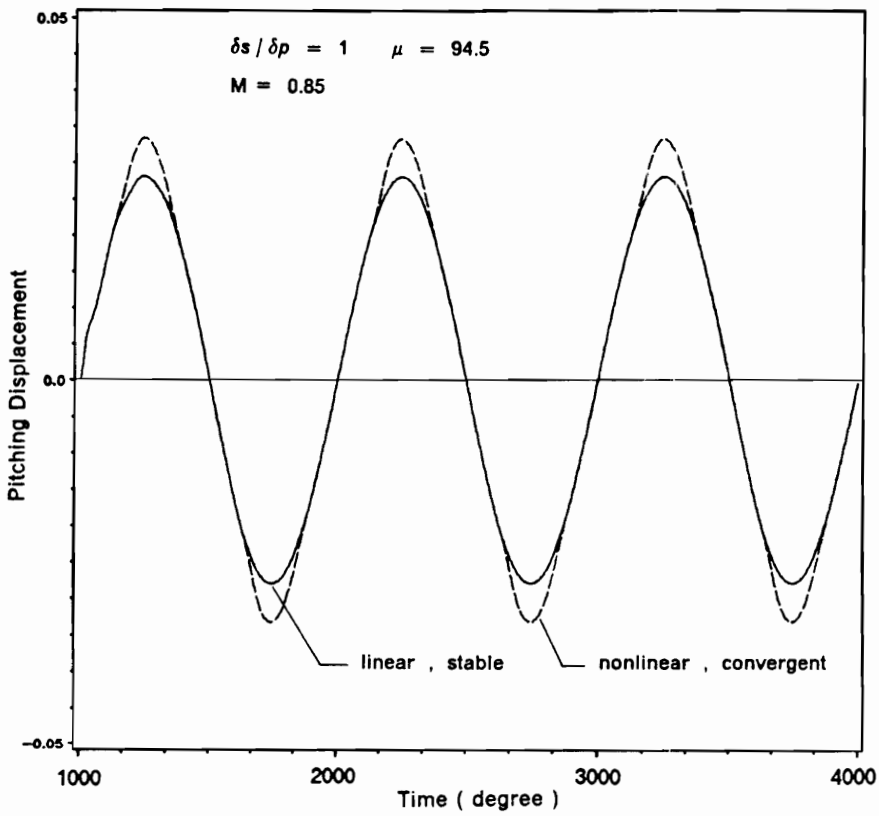


Figure 5.4.9 Comparison of the pitching displacement of two degree-of-freedom system with and without preload nonlinearity exist in the torsional spring.

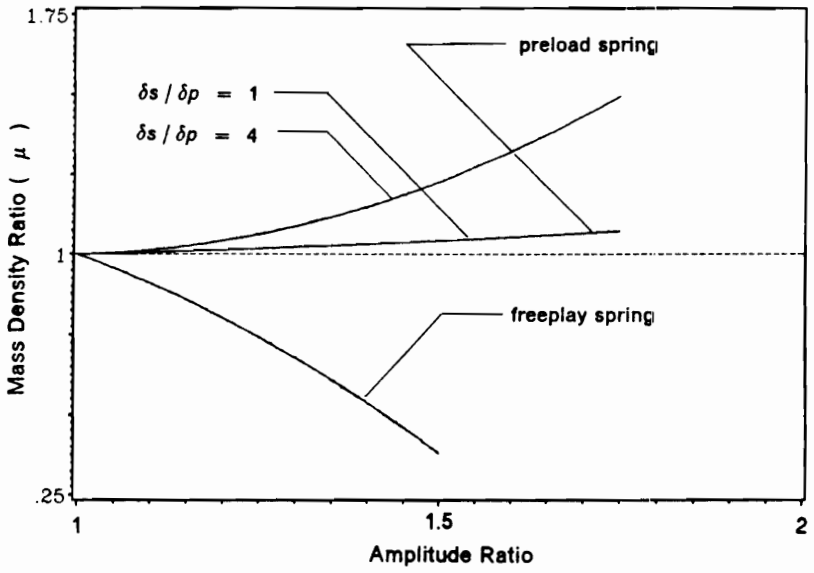


Figure 5.4.10 Effects of preload and freeplay nonlinearity on the mass density flutter boundary of two degree-of-freedom system , M = 0.85.

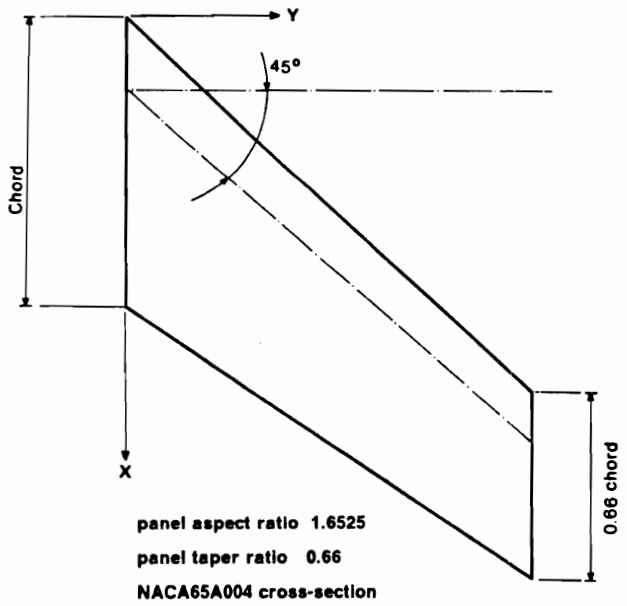


Figure 5.5.1 Plan view of 45° swept WEAK3 wing model geometry.

a) first bending mode

b) first torsion mode

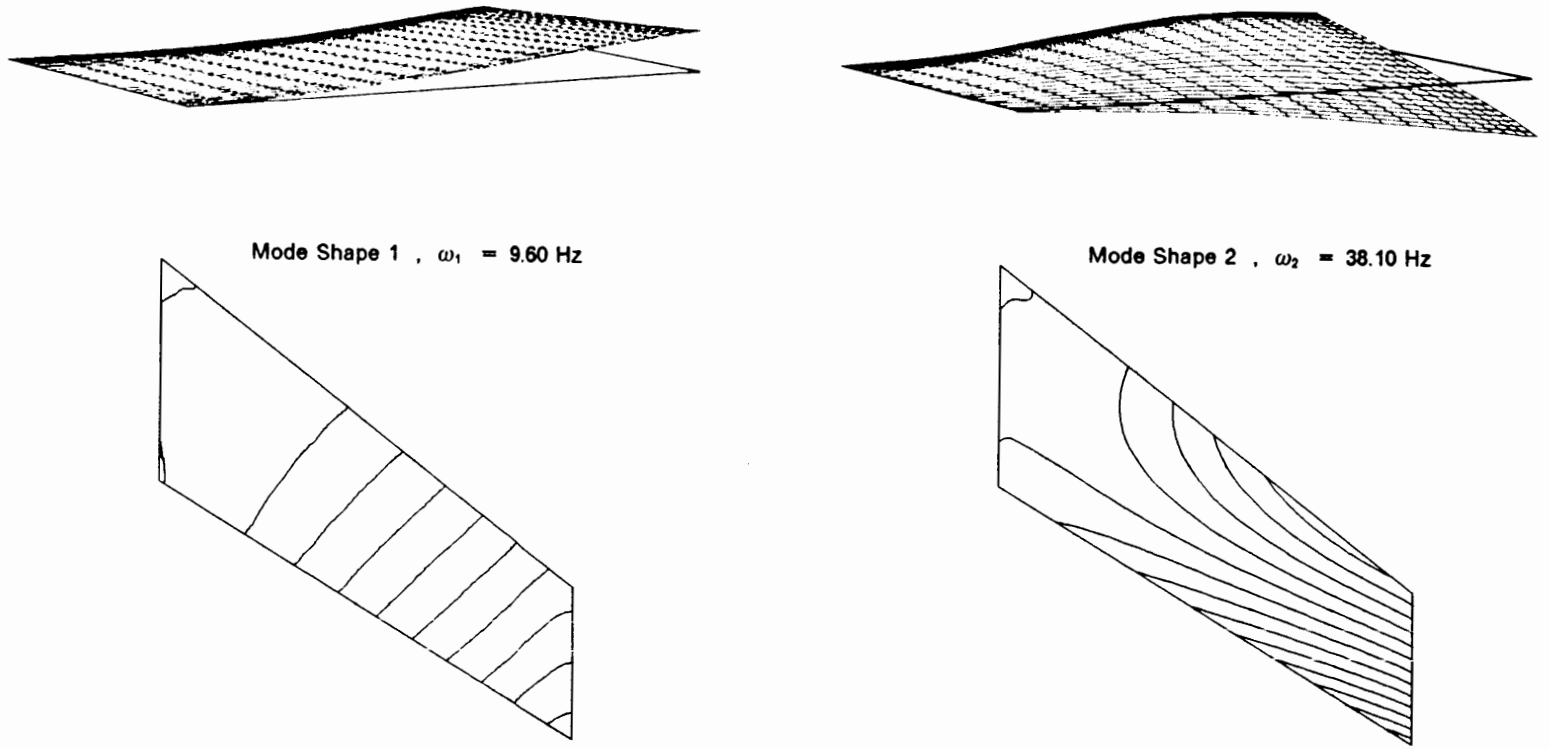


Figure 5.5.2 Oblique projections of four mode shapes and its displacement contour of 45° swept wing.

c) second bending mode

Mode Shape 3 , $\omega_3$ = 50.71 Hz

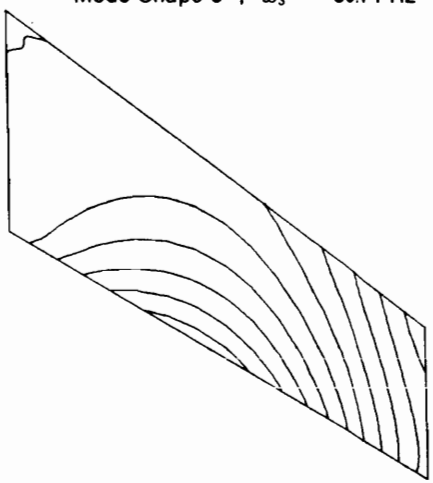

d) second torsion mode

Mode Shape 4 , $\omega_2$ = 98.50 Hz

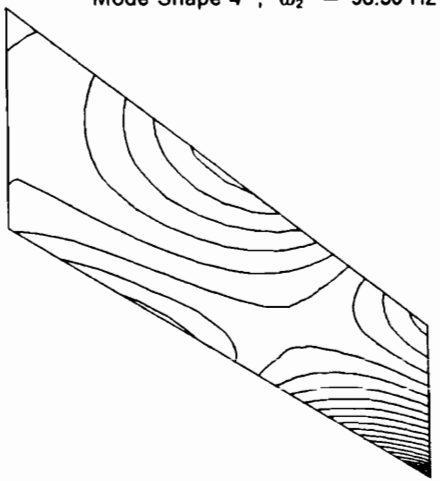

Figure 5.5.2 Concluded

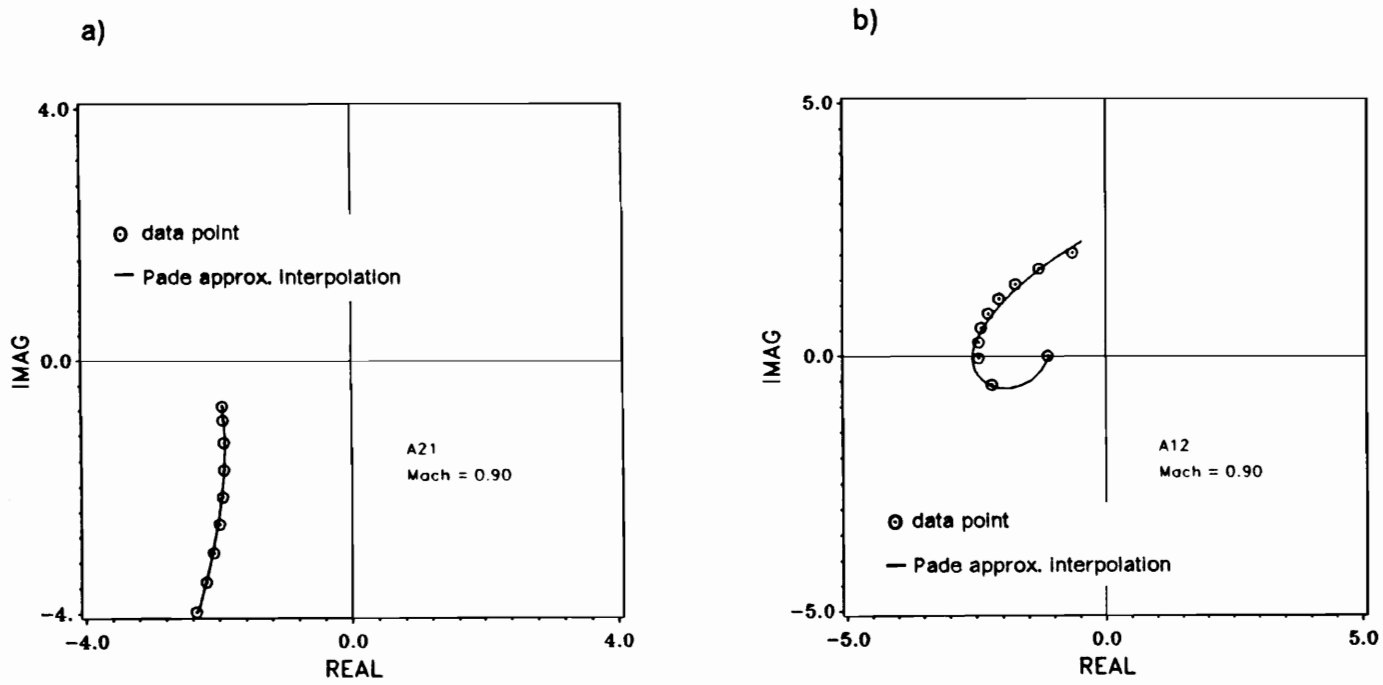


Figure 5.5.3 Comparison of the generalized unsteady aerodynamic forces , $A_{ij}$ , calculated from pulse transfer function method and its Pade approximation at various values of reduced frequency, a) $A_{12}$ b) $A_{21}$ c) $A_{14}$ d) $A_{41}$ .

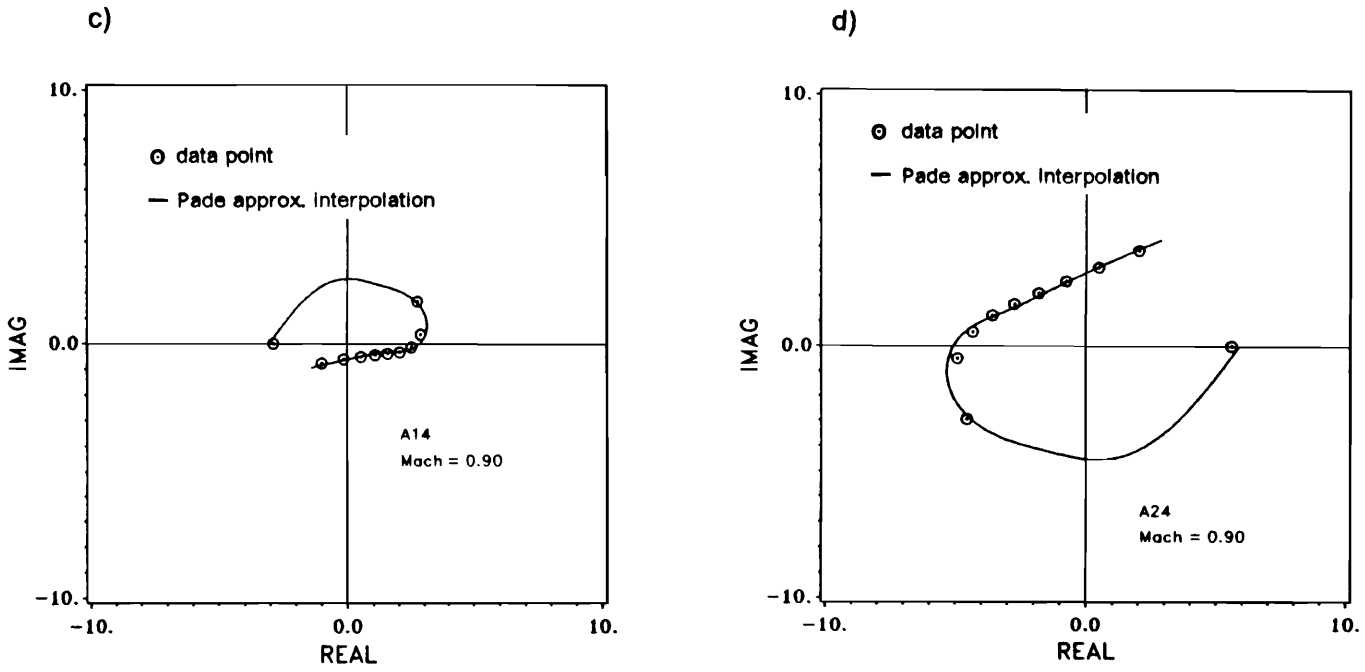


Figure 5.5.3 Concluded

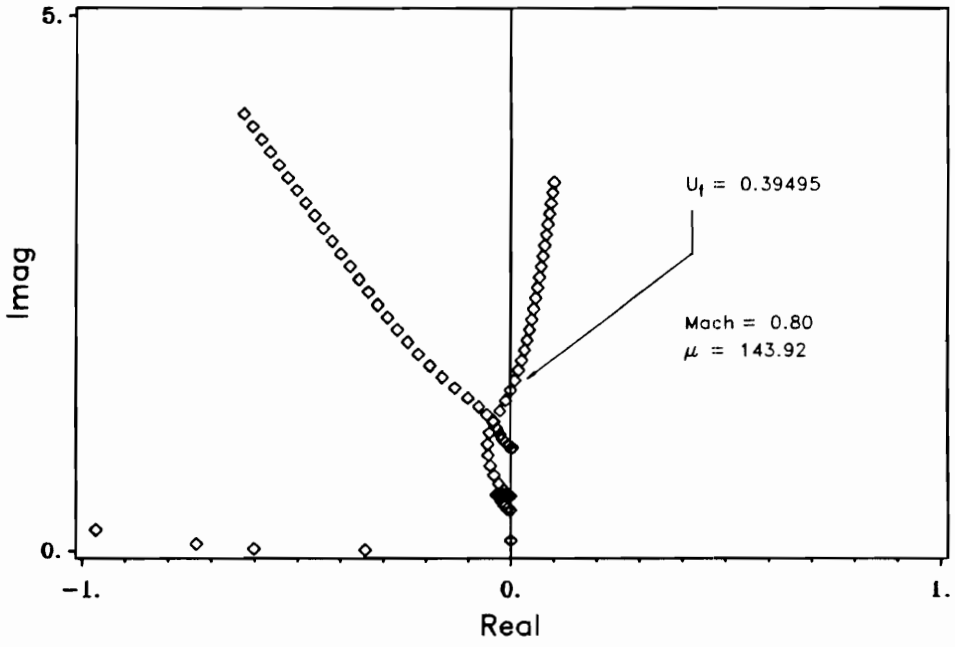


Figure 5.5.4 Nondimensional dynamic pressure root-loci for free-stream Mach number 0.80 at $\mu = 143.92$ , $\alpha_\beta = 0°$ and $\Delta\bar{q} = 0.3$ .

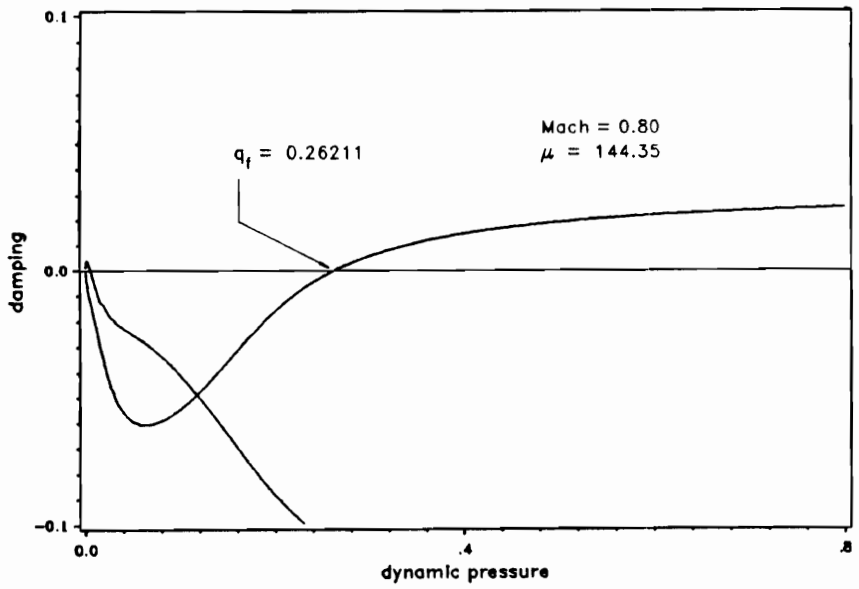


Figure 5.5.5 Structural damping coefficient versus nondimensional dynamic pressure, for the first torsion and bending mode.

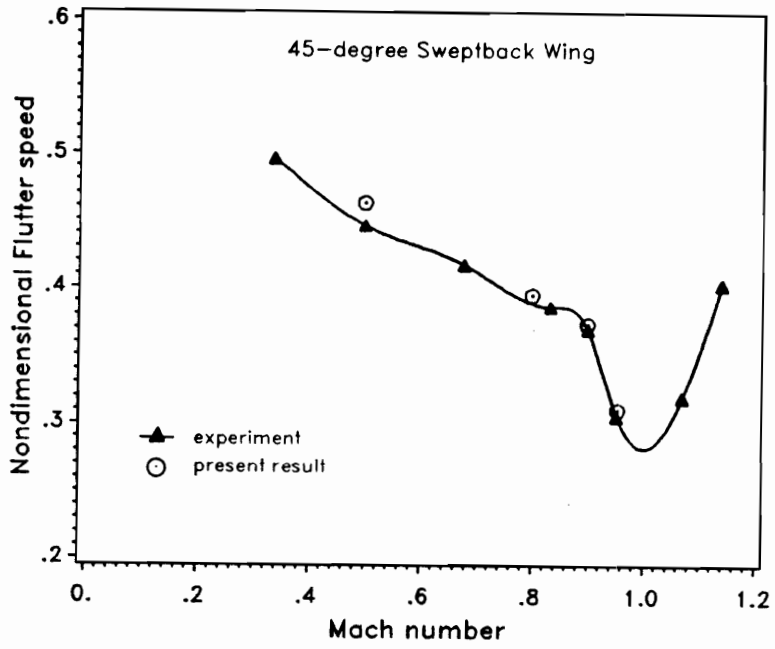


Figure 5.5.6 Comparison between present flutter calculations with experimental data for 45° swept WEAK3 wing in air, nondimensional flutter speed versus Mach number.

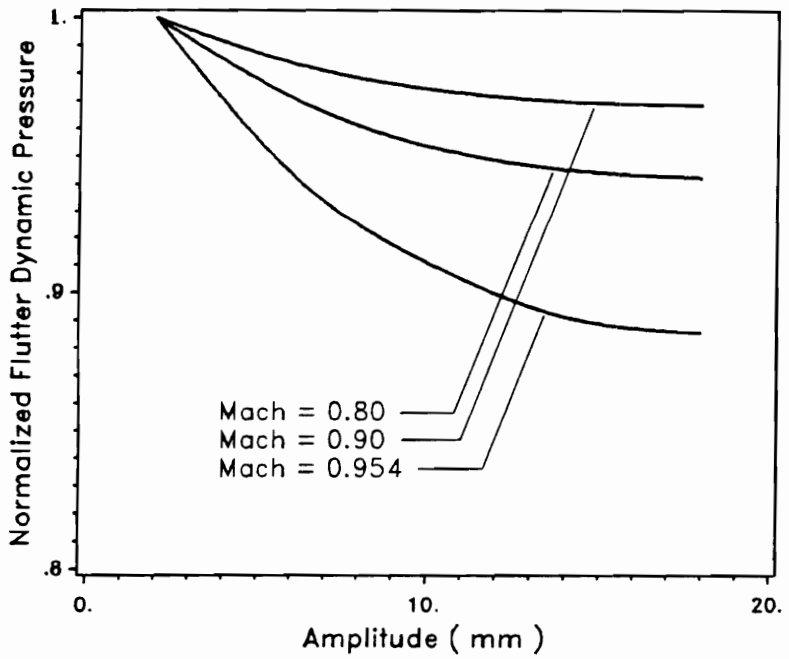


Figure 5.5.7 Variations of nondimensional flutter for 45° swept wing with respect to the oscillation amplitude due to distributed structural nonlinearity at various free-stream Mach number.

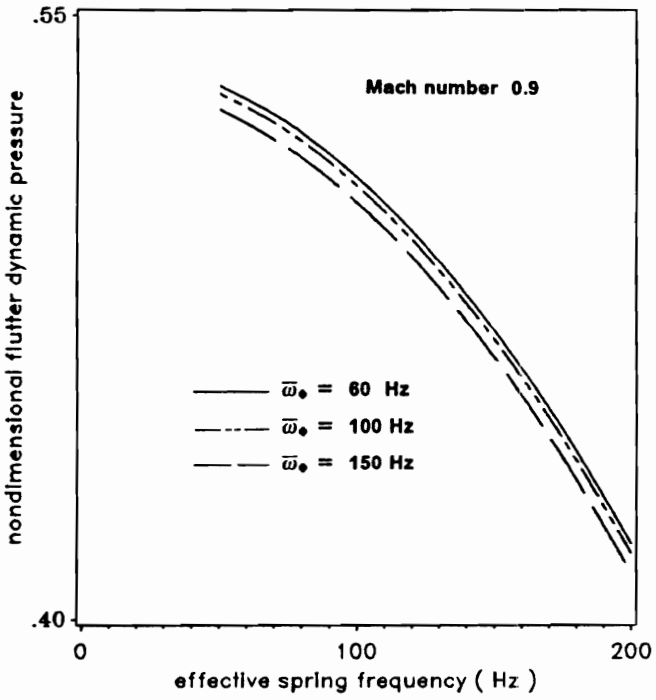


Figure 5.5.8 Variations of nondimensional flutter dynamic pressure with respect to the effective uncoupled torsional spring frequency, $\omega_\theta$ , at M = 0.90 for various values of uncoupled roll spring frequency , $\omega_\phi$ .

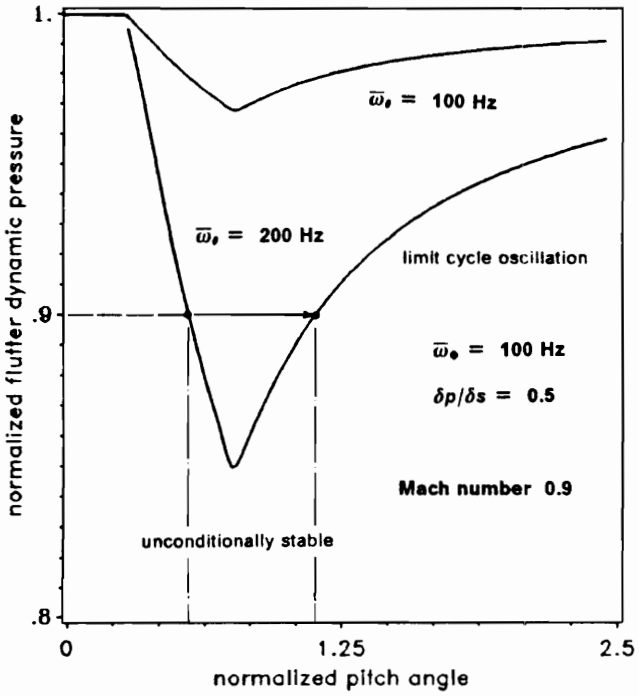


Figure 5.5.9 Flutter boundary of system with nonlinear torsional spring for various values of effective uncoupled torsional spring frequency

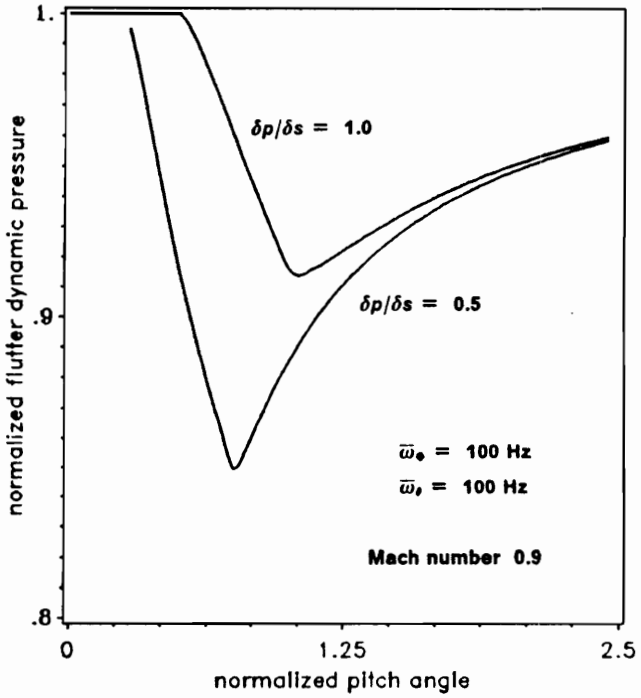


Figure 5.5.10 Flutter boundary of system with nonlinear torsional spring for various values of preload amplitude.

# Chapter 6

# Conclusions

This study has examined the flutter characteristic of two-dimensional airfoil section and three-dimensional 45° swept wing model in transonic flow. General finite-difference solutions for predicting the unsteady aerodynamic loads for two and three-dimensional configurations have been developed and presented. Comparisons of the steady and unsteady pressure coefficients calculated using present solutions with results from other methods and with experimental data have been found to be favorable.

An efficient method called the pulse transfer function analysis of calculating transonic unsteady generalized aerodynamic forces ( GAF ) previously developed for a two-dimensional airfoil section model was extended to treat more general flexible modes of a wing. The GAF calculations based on the harmonic oscillation method is also presented. Comparison of calculated GAFs from both methods showed good agree-

ment, which verified the pulse transfer function analysis for application to three-dimensional transonic flows. It was shown that computational resources required by the pulse analysis were an order of magnitude less than those required by the harmonic method.

For the two-dimensional airfoil section model, the flutter solutions obtained using time marching and eigenvalue solution were in agreement. The linear flutter boundary for three-dimensional wing model compared well with the experimental data, which is the first step toward validating the solution procedure for more general aeroelastic applications.

The effects of structural nonlinearities ( concentrated and distributed nonlinearity ) on flutter boundary of lifting surface was also investigated. It was shown that the presence of structural nonlinearity can adversely affect the flutter characteristic of the lifting surfaces. Of particular concern is the occurrence of the limit cycle oscillation observed in the three-dimensional wing model, which may lead to structural failure due to material fatigue. The results obtained in this study show that lifting surface with structural nonlinearity are susceptible to limit cycle behavior at dynamic pressure lower than the linear flutter value. It was also shown that the flutter solutions using second-order asymptotic expansion for the spring stiffness predict a lower flutter dynamic pressure as compared to the first-order solution ( the so-called describing function method ).

Further research in this area could include the time marching aeroelastic solution of three-dimensional wing model to verify the accuracy of the frequency-domain solutions. It also would be useful to extend the method developed in this study for system with multiple nonlinearities. This may be accomplished by using an iterative

procedure similar to the one given in Ref. 98. The prediction of the unsteady aerodynamic force could also be improved by taking into account the vorticity and entropy corrections in the flow field calculations.

# References


1. Bisplinghoff, R. L., *Aeroelasticity* , Addison Wesley Pub. Co., Cambridge, Mass., 1955.
2. Bisplinghoff, R. L. and Ashley, H., *Principles of Aeroelasticity* , John Wiley & Sons, New York, N.Y., 1969.
3. Dowell, Earl H. ( Editor ), *A Modern Course in Aeroelasticity* , Sijthoff & Noordhoff, Alphen aan den Rijn, The Netherland, 1980.
4. Fung, Y. C., *Introduction to the Theory of Aeroelasticity* , Dover Pub., New York, N.Y., 1969.
5. Hassig, H. J., " An Approximate True Damping Solution of the Flutter Equation by Determinant Iteration, " *Journal of Aircraft* , vol. 8, no. 11, November 1971, pp. 885-889.
6. Richardson, J. R., " A More Realistic Method for Routine Flutter Calculation, " *AIAA Symposium on Structural Dynamics and Aeroelasticity* , Boston, Mass., August 1965.

7. Landahl, M. T., " Graphical Technique for Analyzing Marginally Stable Dynamic Systems, " *Journal of Aircraft* , vol. 1, no. 5, September 1964, pp. 293-299.

8. Frueh, F. J. and Miller, J. M., " Prediction of Dynamic Response from Flutter Analysis Solutions, " Rept. 65-0952, Air Force Office of Scientific Research, Arlington, Va., June 1965.

9. Erickson, A. L. and Stephenson, J. D., " A Suggested Method of Analyzing for Transonic Flutter of Control Surface Based on Available Experimental Evidence, " NACA A7E30, December 1947.

10. Theodorsen, T., " General Theory of Aerodynamic Instability and the Mechanism of Flutter, " NACA Rep. 496, 1935.

11. Albano, E. and Rodden, W. P., " A Doublet-Lattice Method for Calculating Lift Distribution on Oscillating Surfaces in Subsonic Flows," *AIAA Journal* , vol. 7, no. 2, February 1969, pp. 279-285.

12. Cunningham, A. M. Jr., " Unsteady Subsonic Collocation Method for Wing With and Without Control Surface, " *Journal of Aircraft* , vol. 9, no. 6, June 1972.

13. Yates, Carson E. Jr., Land, Norman S. and Foughner, Jerome T., " Measured and Calculated Subsonic and Transonic Flutter Characteristics of A 45-degree Sweptback Wing Planform in Air and in Freon-12 in the Langley Transonic Dynamic Tunnel, " NASA TN D-1616, March 1963.

14. Sanford, M. C., Ruhlin, C. L. and Abel, I., " Transonic Flutter Study of A 50.5-degree Cropped-Delta Wing with Two Rearward-Mounted Nacelles, " NASA TN D-7544, June 1974.

15. Goetz, R. C. and Dogget, R. V. Jr., " Some Effects of Tipfins on Wing Flutter Characteristic, " NASA TN D-7702, 1974.

16. Ashley, H., " Role of Shocks in the Subtransonic Flutter Phenomena, " AIAA Paper 79-0765, April 1979.

17. Farmer, M. G., Hanson, P. W. and Wynne, E. C., " Comparison of Supercritical and Conventional Wing Flutter Characteristic, " NASA TM X-72837, May 1976.

18. Landahl, M. T., *Unsteady Transonic Flow* , Cambridge University Press, Cambridge, Mass., 1989.

19. Forsching, H., " Introductory Survey of Aeroelastic Problems in Separated and Transonic Flow, " VKI Lecture Series, Rhode Saint Genese, Belgium, March 1981.

20. Ehlers, F. E., " A Finite Difference Method for the Solution of the Transonic Flow Around Harmonically Oscillating Wings, " NASA CR-2257, 1974.

21. Traci, R. M., Albano, E. D. and Farr, T. L., " Small Disturbance Transonic Flow About Oscillating Airfoil and Planar Wing, " AFFDL TR-100, August 1975.

22. Cunningham, A. M., " Further Development in Prediction of Steady Nonlinear Transonic Flows, " AIAA Paper 75-099, January 1979.

23. Isogai, K., " Calculation of the Unsteady Transonic Flow over Oscillating Airfoils Using the Full Potential Equation, " AIAA Paper 77-448, Dynamic Specialist Conference, San Diego, Ca., March 1977.

24. Magnus, R. and Yoshihara, H., " Inviscid Transonic Flow over Airfoils, " *AIAA Journal* , vol. 8, no. 12, December 1970, pp. 2157-2162.

25. Ballhaus, W. F. and Goorjian, P. M., " Implicit Finite Difference Computations of Unsteady Transonic Flow about Airfoils, " *AIAA Journal* , vol. 15, no. 12, December 1977, pp. 1728-1735.

26. Ballhaus, W. F. and Lomax, H., " The Numerical Simulation of Low Frequency Unsteady Transonic Flow Fields, " Proceeding 4th International Conference on Numerical Methods in Fluid Dynamics, Boulder, Co., June 1974.

27. Ballhaus, W. F. and Steger, J. L., " Implicit Approximate Factorization Schemes for the Low Frequency Transonic Equation, " NASA TM X-73082, 1975.

28. Ballhaus, W. F. and Bridgemen, J. O., " Numerical Solution Techniques for Unsteady Transonic Aerodynamic Problems, " AGARD Special Course on Unsteady Aerodynamics, VKI, Rhode Saint Genese, Belgium, 1980.

29. Rizzetta, D. P. and Chin, W. C., " Effect of Frequency in Unsteady Transonic Flow, " *AIAA Journal* , vol. 17, no. 7, July 1979, pp. 779-781.

30. Houwink, R. and van der Vooren, J., " Results of an Improved Version of LTRAN2 for Computing Unsteady Airloads on Airfoil Oscillating in Transonic Flow, " AIAA Paper 79-1552, 1979.

31. Yang, T. Y., Guruswamy, G. P. and Striz, A. G., " Flutter Analysis of A NACA64A006 Airfoil in Small Disturbance Transonic Flow," *Journal of Aircraft* , vol. 17, no. 4, April 1980, pp. 225-231.

32. Murman, E. M. and Cole, J. D., " Calculations of Plane Steady Transonic Flow " *AIAA Journal* , vol. 9, no. 2, 1971, pp. 98-116.

33. Jameson, A., " Transonic Potential Flow Calculations in Conservation Form, " Proceeding AIAA 2nd Computational Fluid Dynamic Conference, Hartford, Conn., 1975.

34. Goorjian, P. M., " Implicit Computation of Usteady Transonic Flow Governed by the Full Potential Equation in Conservation Form, " AIAA Paper 80-0150, 1980.

35. Steger, J. L. and Carradonna, F. X., " A Conservative Implicit Finite Difference Algorithm for the Unsteady Full Potential Equation," AIAA Paper 80-1368, 1980.

36. Chipman, R. and Jameson, A., " Altenating Direction Implicit Algorithm for Unsteady Transonic Flow, " AIAA Paper 81-0329, 1981.

37. Steger, J. L. and Bailey, H. E., " Calculation of Transonic Aileron Buzz, " *AIAA Journal* , vol. 18, no. 3, March 1980, pp. 249-255.

38. Lerat, A. and Sides, J., " Calcul Numerique d'ecoulements Transsoniques Instationnaires " ONERA TP no. 1977-19E, 1977.

39. Grossman, B. and Moretti , " Time-Dependent Computation of Transonic Flows " AIAA Paper 70-1322, Oct 1970.

40. Tijdeman, H., " Investigation of the Transonic Flow Around Oscillating Airfoils, " National Aerospace Laboratory, NLR TR 77090U , The Netherland, 1978.

41. Borland, C. J. and Rizzetta, D. P., " Transonic Unsteady Aerodynamics for Aeroelastic Application, vol. 1 - Technical Development Summary for XTRAN3S, " AFWAL-TR-80-3107, June 1982.

42. Batina, J. T., Seidel, D. A., Bland, S. R. and Bennett, R. M., " Unsteady Transonic Flow Calculations for Realistic Aircraft Configuratuons, " AIAA Paper 87-0850, April 1987.

43. Sankar, L. N., Malone, J. B. and Schuster, D., " Full Potential and Euler Solution for the Unsteady Transonic Flow Past a Fighter Wing," AIAA Paper 85-0511, 1985.

44. Whitlow, W. Jr., Hafez, M. H. and Osher, S. J., " Entropy Correction Method for Unsteady Full Potential Flows with Strong Shocks," AIAA Paper 86-1768 CP, 1986.

45. Shankar, V., Ide, H. and Gorski, J., " A Fast, Time - Accurate Unsteady Full Potential Scheme, " AIAA Paper 85-1512 CP, 1985.

46. Stone, H. L., " Iterative Solution of Imlicit Approximation of Multi-Dimensional Partial Differential Equations, " *SIAM Journal of Numerical Analysis* , vol. 5, no. 3, 1968, pp. 530-550.

47. Steinhoff, J. and Jameson, A., " Multiple Solutions of the Transonic Potential Flow Equation, " AIAA Paper 81-1019, 1981.

48. Guruswamy, G. P., " ENSAERO - A Multidisciplinary Program for Fluid/Structural Interaction Studies of Aerospace Vehicles, " *Computing System in Engineering* , vol. 1, Nos. 2-4, September 1990, pp. 229-236.

49. Batina, J. T., " Unsteady Euler Algorithm with Unstructured Dynamic Mesh for Complex-Aircraft Aeroelastic Analysis, " AIAA Paper 89-1189, April 1989.

50. Rizzetta, D. P., " Procedures for the Computation of Unsteady Transonic Flows Including Viscous Effects, " NASA CR-166249, January 1982.

51. Woolston, D. S., Runyan, H. L. and Andrews, R. E., " An Investigation of Effects of Certain Types of Structural Nonlinearities on Wing and Control Surface Flutter, " *Journal of the Aeronautical Sciences* , January 1957, pp. 57-63.

52. Shen, S. F. and Hsu, C. C., " Analytical Results of Certain Nonlinear Flutter Problems, " *Journal of the Aeronautical Sciences* , February 1958, pp. 136-137.

53. Shen, S. F., " An Approximate Analysis of Nonlinear Flutter Problems, " *Journal of the Aeronautical Sciences* , January 1959, pp. 25-45.

54. Desmarais, R. N. and Reed, W. H., " Wing/Store Flutter With Nonlinear Pylon Stiffness, " *Journal of Aircraft* , vol. 18, no. 11, November 1981, pp. 984-987.

55. Laurenson, R. M. and Trn, R. M., " Flutter Analysis of Missile Control Surfaces Containing Structural Nonlinearities, " *AIAA Journal* , vol. 18, no. 10, October 1981, pp. 1245-1251.

56. Breitbach, E., " Effects of Structural Nonlinearities on Aircraft Vibration and Flutter, " AGARD R-665, January 1978.

57. Breitbach, E., " Flutter Analysis of an Airplane With Multiple Structural Nonlinearities in the Control Systems, " NASA TP-1620, 1980.

58. Woodcock, D. L., " The Determination of Critical Flutter Conditions of Nonlinear Systems, " RAE Technical Memorandum Structures 986, 1981.

59. Kousen, K. A. and Bendiksen, O. O., " Limit Cycle Phenomena in Computational Transonic Aeroelasticity, " AIAA Paper 89-1185 Cp, 1989.

60. McIntosh, S. C. Jr., Reed, R. E. Jr. and Rodden, W. P., "Experimental and Theoretical Study of Nonlinear Flutter, " *Journal of Aircraft* , vol. 18, no. 12, December 1981, pp. 1057-1063.

61. Theodorsen, T. and Garrick, I. E., " Flutter Calculations in Three Degree of Freedom, " NACA Report 741, 1942.

62. Meirovitch, Leonard, *Elements of Vibration Analysis* , McGraw-Hill, Inc., New York, N. Y., 1975.

63. Flannelly, W. G., " Research on Structural Dynamic Listing by Impedance Methods, " USAAMRDL-TR-72-63, November 1972.

64. Vepa, R., " Finite State Modeling of Aeroelastic Systems, " NASA CR-2779, February 1977.

65. Roger, K. L., Hodges, G. E. and Felt, L., " Active Flutter Suppression - A Flight Test Demonstration, " *Journal of Aircraft* , vol. 12, no. 7, June 1975, pp. 551-556.

66. Vepa, R., " On the Used of PAde Approximants to Represent Unsteady Aerodynamic Loads for Arbitrarily Small Motions of Wing, " AIAA Paper 76-17, 1976.

67. Miles, J. W., " Transient Loading of Wide Delta Airfoils at Supersonic Speed, " *Journal of Aeronautical Sciences* , vol. 18, no. 8, August 1951, pp. 543-554.

68. Baker, G. A. Jr., *Essential of Pade Approximants* , Academic Press, New York, N. Y., 1974.

69. Ferrari, C. and Tricomi, F., *Transonic Aerodynamics* , Academic Press, 1968.

70. van der Vooren, J., et al., " Remark on the Suitability of Various Transonic Perturbation equation to Describe Three-Dimensional Transonic Flow - Examples of Computation Using a Fully - Conservative Rotated Difference Scheme, " *Symposium Transonicum II* , Springer-Verlag, Berlin, 1976.

71. Ballhaus, W. F., " Some recent Progress in Transonic Flow Computation, " in *Numerical Method of Fluid Dynamic* ( H. J. Wirz, Editor ), 1976.

72. Kwak, D., " Non-reflecting Farfield Boundary Conditions for Unsteady Transonic Flow Computation, " AIAA Paper 80-1393, 1980.

73. Whitlow, W. Jr., " Characteristic Boundary Conditions for Three-Dimensional Transonic Unsteady Aerodynamic, " NASA TM 86292, October 1984.

74. Guruswamy, G. P. and Goorjian, P. M., " Efficient Algorithm for Unsteady Transonic Aerodynamics of Low-Aspect-Ratio Wings, " *Journal of Aircraft* , vol. 22, no. 3, March 1985, pp. 193-199.

75. Seidel, D. A., Bennett, R. M. and Ricketts, R. H., " Some Applications of XTRAN3S, " NASA TM-85641, May 1983.

76. Lighthill, M. J., " On Boundary Layers and Upstream Influence, Supersonic Flow Without Separation, " Proc. Royal Soc. A217 no. 1131, 1953.

77. Inger, G. R. and Mason, W. H., " Analytical Theory of Transonic Normal Shock Boundary Layer Interaction, " *AIAA Journal* , vol. 14, no. 9, 1976, pp. 1266-1272.

78. Green, J. E., " Application of Head's Entrainment Method to the Prediction of Turbulent Boundary Layers and Wakes in Compressible Flow," RAE Reports and Memoranda no. 3788, April 1972.

79. Melnik, R., " Turbulent Interaction on Airfoils at Transonic Speed - Recent Development, " AGARD CP-291, 1981.

80. Murman, E. M., " Analysis of Embedded Shock Waves Calculated by Relaxation Method, " *AIAA Journal* , vol. 12, no. 5, May 1974, pp. 628-630.

81. van Leer, B., " On the Relation Between the Upwind - Differencing Schemes of Gudonov, Engquist-Osher and Roe, " ICASE Report no. 81-11, March 1981.

82. Batina, J. T., " An Efficient Algorithm for Solution of the Unsteady Transonic Small - Disturbance Equation, " NASA TM 89014, December 1986.

83. Engquist, B. E. and Osher, S. J., " Stable and Entropy satisfying Approximations for Transonic Flow Calculations, " *Mathematics of Computation* , vol. 34, no. 149, January 1980.

84. Ballhaus, W. F. and Goorjian, P. M., " Computation of Unsteady Transonic Flows by the Indicial Method, " AIAA Paper 77-447, March 1977.

85. Seidel, D. A., Bennett, R. M. and Whitlow, W., Jr., " An Exploratory Study of Finite Difference Grids for Transonic Unsteady Aerodynamic, " AIAA Paper 83-1811, July 1983.

86. Bland, S. R., " AGARD 3-Dimensional Aeroelastic Configurations," AGARD AR 167, 1982.

87. Bland, S. R. and Edwards, J. W., " Airfoil Shape and Thickness Effects on Transonic Airload and Flutter, " *Journal of Aircraft* , vol. 21, no. 3, March 1984, pp. 209-217.

88. Breitbach, E., " Die Bedeutung Struktureller Nicthtlinearitaten aus der Sicht der Strukturdynamik und Aeroelastik, " DLR-FB 77-34, 1977.

89. Haidl, G., " Nonlinear Effects in Aircraft Ground and Flight Vibration Tests, " AGARD Report no. 652, 1976.

90. Breitbach, E., " Strukturelle Nicthtlinearitaten and Schwingenden Flugzeugen, insbesondene am 'Starfighter' F104G, " AVA-Bericht 67J04, 1967.

91. Kussner, H. G., " A Comparison of Methods Used in Flutter Research , " AGARD Report no. 592, August 1972.

92. Bogoliubov, N. N. and Mitropolsky, Y. A., *Asymptotic Methods in the Theory of Non-Linear Oscillations* , Gordon and Breach Science Pub., New York, N.Y., 1985.

93. Lotze, A., Sensburg, O. and Kuhn, M., " Flutter Investigation of a Combat Aircraft With a Command and Stability Augmentation System, ' *Journal of Aircraft* , vol. 14, no. 4, 1977, pp. 368-374.

94. Guruswamy, P. and Yang, T. Y., " Aeroelastic Time Response Analysis of Thin Airfoil by Transonic Code LTRAN2, " *Computer and Fluids* , vol. 9, no. 4, 1981, pp. 409-425.

95. Bathe, K. J. and Wilson, E. L., *Numerical Methods in Finite - Element Analysis* , Prentice-Hall, Englewood Cliffs, NJ., 1976.

96. Bennett, R. M. and Batina, J. T., " Application of the CAP-TSD Unsteady Transonic Small Disturbance Program to Wing Flutter, " AIAA Paper 89-003, April 1989.

97. Bennett, R. M., Batina, J. T. and Cunningham, H. J., " Wing Flutter Calculation With the CAP-TSD Unsteady Transonic Small Disturbance Program, " AIAA Paper 88-2347, 1988.

98. Lee, Craig L., " An Iterative Procedure for Nonlinear Flutter Analysis " *AIAA Journal* , vol. 24, no. 5, May 1986, pp. 833-840.

99. LeBalleur, J. C., Peyret, R. and Viviand, H., " Numerical Studies in High Reynolds Aerodynamics, " *Computer and Fluids* , Vol. 8, 1980.

100. Melnik, R. E. and Grossman, B., " Analysis of the Interaction of a Weak Normal Shock Wave with a Turbulent Boundary Layer, " AIAA Paper 74-598, June 1974.

101. Adamson, T. C. Jr. and Messiter, A. F., " Normal Shock Wave Turbulent Boundary Layer Interactions in Transonic Flow near Separation," in *Transonic Flow Problems in Turbomachinery* , Hemisphere Publ. Co., 1977, pp. 392-414.

# Appendix A

## Aerodynamic Transfer Coefficients

The unsteady aerodynamic forces usually are computed at a given Mach number, M , for only a finite values of the reduced frequency, k . The variation of the aerodynamic forces with reduced frequency in s-plane can be approximated by a rational polynomial of the form

$$\tilde{A}(k) = A_0 + A_1(ik) + A_2(ik)^2 + \sum_{m=3}^{6} \frac{A_m(ik)}{(ik + \beta_{m-2})} \qquad [A.1]$$

The real and imaginary parts of the forces, $\tilde{A}$ , are

$$Re(\tilde{A}) \equiv \tilde{A}_R = A_0 - A_2 k^2 + \frac{A_3 k^2}{(k^2 + \beta_1^2)} + \frac{A_4 k^2}{(k^2 + \beta_2^2)} + \frac{A_5 k^2}{(k^2 + \beta_3^2)} + \frac{A_6 k^2}{(k^2 + \beta_4^2)} \qquad [A.2]$$

$$Im(\tilde{A}) \equiv \tilde{A}_I = A_1 k + \frac{A_3 k \beta_1}{(k^2 + \beta_1^2)} + \frac{A_4 k \beta_2}{(k^2 + \beta_2^2)} + \frac{A_5 k \beta_3}{(k^2 + \beta_3^2)} + \frac{A_6 k \beta_4}{(k^2 + \beta_4^2)} \qquad [A.3]$$

in which $\tilde{A}$ are calculated at a discrete values of k .

From Eqs. [A.2] and [A.3] , for each value of k, the real and imaginary error function of $\tilde{A}$ may be determined , that is

$$Real\,(error_j) \equiv E_{Rj} = \tilde{A}_{Rj} - \{B_{Rj}\}^T \{c\}$$

$$Imag\,(error_j) \equiv E_{Ij} = \tilde{A}_{Ij} - \{B_{Ij}\}^T \{c\}$$

where

$$\{B_{Rj}\}^T = \left(1 \quad 0 \quad -k_j^2 \quad \frac{k_j^2}{k_j^2+\beta_1^2} \quad \frac{k_j^2}{k_j^2+\beta_2^2} \quad \frac{k_j^2}{k_j^2+\beta_3^2} \quad \frac{k_j^2}{k_j^2+\beta_4^2}\right)$$

$$\{B_{Ij}\}^T = \left(0 \quad k_j^2 \quad 0 \quad \frac{k_j\beta_1}{k_j^2+\beta_1^2} \quad \frac{k_j\beta_2}{k_j^2+\beta_2^2} \quad \frac{k_j\beta_3}{k_j^2+\beta_3^2} \quad \frac{k_j\beta_4}{k_j^2+\beta_4^2}\right)$$

$$\{c\}^T = (A_0 \; A_1 \; A_2 \; A_3 \; A_4 \; A_5 \; A_6)$$

and index j refers to a particular reduced frequency $k_j$ at which A is calculated.

The complex error function of the approximation can be written as

$$E_j = E_{Rj} + i E_{Ij}$$

For N data points, the least - square fit are determined by requiring

$$\frac{\partial}{\partial A_l}\left[\sum_{j=1}^{N}(E_j \times \bar{E}_j)\right] = 0$$

where $\bar{E}_j$ is the complex conjugate of $E_j$.

Differentiation of this equation yields the following set of normal equations

$$\sum_{j=1}^{N}\left[(\tilde{A}_{Rj} - \{B_{Rj}\}^T\{c\})\{B_{Rj}\} + (\tilde{A}_{Ij} - \{B_{Ij}\}^T\{c\})\{B_{Ij}\}\right] = 0$$

from which the vector of the coefficients of the fit, { c } , can be computed.

$$\{c\} = \left[\sum_{j=1}^{N} - \{B_{Rj}\}^T\{B_{Rj}\} - \{B_{Ij}\}^T\{B_{Ij}\}\right]^{-1}\left[\sum_{j=1}^{N}(Q_{Rj}\{B_{Rj}\} + Q_{Ij}\{B_{Ij}\})\right] \quad [A.4]$$

Let s , the Laplace variable, is equal to $i\omega$ , from the definition of reduced frequency $k = \omega b/U$ then ik = s b / U = $\bar{s}$ .

Substituting this relationship into Eq. [A.1] yields

$$\tilde{A}(\bar{s}) = A_0 + A_1(\bar{s}) + A_2(\bar{s})^2 + \sum_{m=3}^{6}\frac{A_m(\bar{s})}{(\bar{s} + \beta_{m-2})} \quad [A.5]$$

where coefficients $A_0, \ldots, A_6$ are determined from Eq. [A.4] . The values of $\beta_{m-2}$ are non - critical and arbitrarily choosen from the range of reduced frequencies for which the transonic aerodynamic data have been calculated.

# Appendix B

## Aeroelastic Equations of Motion Using Finite State Aerodynamic Model

The transonic aeroelastic stability analyses and flutter calculations in frequency domain for a three - dimensional wing model are performed using finite state aeroelastic modeling. The equation of motion of the system are cast in the Laplace - domain, i.e. the s - plane, instead of the usual k - plane, in order to avoid working with complex matrices. The finite state generalized aerodynamic forces are approximated by interpolating the aerodynamic forces calculated from the solution of the transonic small disturbance flow equation using Pade's approximating functions ( see Appendix A ). This approximation function when coupled to the equations of motion and Laplace transformed leads to a linear first-order matrix equation.

Assume that the displacement of the system may be described by separation of time and space variables as

$$z(x,y,t) = f(t)\,Z(x,y)$$

and this displacement can be approximated using a finite modal series as

$$z(x,y,t) = \sum_{j=1}^{n} q_j(t)\,h_j(x,y)$$

where $q_j(t)$ is the generalized modal displacement and $h_j(x,y)$ is the j-th mode shape of the wing structure.

The equation of motion, derived using the Lagrange's equations, can be written as

$$[M]\{\ddot{q}\} + [C]\{\dot{q}\} + [K]\{q\} = \{Q\} \qquad [B.1]$$

where [ M ] , [ C ] , [ K ] are the mass, damping and stiffness matrices , respectively , and { Q } is the vector of generalized forces. The elements of these matrices are defined as follow :

$$M_{i,j} = \int_s m(x,y)\,h_i^2(x,y)\,dS \quad , \quad for \quad i=j$$
$$= 0 \quad , \quad for \quad i \neq j$$
$$C_{i,j} = 2\zeta_i M_{i,j}\,\omega_{n,i} \quad , \quad for \quad i=j$$
$$= 0 \quad , \quad for \quad i \neq j$$
$$K_{i,j} = M_{i,j}\,\omega_{n,i}^2 \quad , \quad for \quad i=j$$
$$= 0 \quad , \quad for \quad i \neq j$$

$$Q_i(t) = \bar{q}\,c^2 \int_S \frac{\Delta p(x,y,t)}{\bar{q}}\,h_i(x,y)\,\frac{dS}{c^2}$$

with $\bar{q}$ is the dynamic pressure , c is the chord length, and S is the wing surface area.

The total pressure distribution, $\Delta p$ (x,y,t) , can be expressed as the sum of the contribution due to each of the flexible mode, $q_j$ (t) . Therefore,

$$\Delta p(x,y,t) = \sum_{j=1}^{n} \Delta p_j(x,y,k)\, q_j(t)$$

$\Delta p_j$ (x,y,k) , is the lifting pressure at point (x,y) due to the wing deformation in the j-th mode shape. Substituting this equation into the previous one results in

$$\begin{aligned} Q_i(t) &= (\bar{q}c^2) \sum_{j=1}^{n} q_j(t) \left\{ \int_s \frac{\Delta p_j(x,y)}{\bar{q}}\, h_i(x,y)\, \frac{dS}{c^2} \right\} \\ &= (\bar{q}c^2) \sum_{j=1}^{n} A_{i,j}\, q_j \end{aligned}$$

Using this new force vector and taking the Laplace transform of Eq. [B.1] , the equations of motion in s variable may be written as,

$$\left( [\bar{M}]\, s^2 + [\bar{C}]\, s + (\bar{q}c^2)\, [\tilde{A}(s)] + [\bar{K}] \right) \{q\} = 0 \qquad [B.2]$$

where $\tilde{A}(s)$ represents the Laplace transform of A and $s = i\omega$ .

The finite state of the generalized aerodynamic forces , [ $\tilde{A}$ ] , are approximated in the s-plane by using an interpolating function of the form

$$[\tilde{A}(\bar{s})] = [A_0] + [A_1](\bar{s}) + [A_2](\bar{s})^2 + \sum_{m=3}^{6} \frac{[A_m](\bar{s})}{(\bar{s} + \beta_{m-2})} \qquad [B.3]$$

in which $\bar{s}$ is equal to $sb/U$. Substituting this aerodynamic approximating coefficients into Eq. [B.2] and rearranging it yields,

$$\left\{[B_1]\bar{s}^2 + [B_2]\bar{s} + [B_3] + \frac{[B_4]\bar{s}}{(\bar{s}+\beta_1)} + \frac{[B_5]\bar{s}}{(\bar{s}+\beta_2)} + \frac{[B_6]\bar{s}}{(\bar{s}+\beta_3)} + \frac{[B_7]\bar{s}}{(\bar{s}+\beta_4)}\right\}\{q\} = 0$$

where
$$[B_1] = [M] + \bar{q}c^2[A_2]$$
$$[B_2] = [C] + \bar{q}c^2[A_1]$$
$$[B_3] = [K] + \bar{q}c^2[A_0]$$
$$[B_4] = \bar{q}c^2[A_3]$$
$$[B_5] = \bar{q}c^2[A_4]$$
$$[B_6] = \bar{q}c^2[A_5]$$
$$[B_7] = \bar{q}c^2[A_6]$$

Multiply the whole equation with the denominator and grouping the terms of the same power in $\bar{s}$,

$$\begin{aligned}&([D_6]\bar{s}^6 + [D_5]\bar{s}^5 + [D_4]\bar{s}^4 + [D_3]\bar{s}^3 + \\ &[D_2]\bar{s}^2 + [D_1]\bar{s} + [D_0])\{q\} = 0\end{aligned} \qquad [B.4]$$

where
$$[D_6] = [B_1]$$
$$[D_5] = a_1[B_1] + [B_2]$$
$$[D_4] = a_2[B_1] + a_1[B_2] + [B_3] + [B_4] + [B_5] + [B_6] + [B_7]$$
$$[D_3] = a_3[B_1] + a_2[B_2] + a_1[B_3] + b_1[B_4] + c_1[B_5] + d_1[B_6] + e_1[B_7]$$
$$[D_2] = a_4[B_1] + a_3[B_2] + a_2[B_3] + b_2[B_4] + c_2[B_5] + d_2[B_6] + e_2[B_7]$$
$$[D_1] = a_4[B_2] + a_3[B_3] + b_3[B_4] + c_3[B_5] + d_3[B_6] + e_3[B_7]$$
$$[D_0] = a_4[B_3]$$

The coefficients $a_1, ..., a_4; .....; e_1, ..., e_3$ are computed from the multiplication of the terms at the denominator of Eq. [B.3] , defined as follows :

$$(\bar{s} + \beta_1)(\bar{s} + \beta_2)(\bar{s} + \beta_3)(\bar{s} + \beta_4) = \bar{s}^4 + a_1 \bar{s}^3 + a_2 \bar{s}^2 + a_3 \bar{s} + a_4$$

$$(\bar{s} + \beta_2)(\bar{s} + \beta_3)(\bar{s} + \beta_4) = \bar{s}^3 + b_1 \bar{s}^2 + b_2 \bar{s} + b_3$$

$$(\bar{s} + \beta_1)(\bar{s} + \beta_3)(\bar{s} + \beta_4) = \bar{s}^3 + c_1 \bar{s}^2 + c_2 \bar{s} + c_3$$

$$(\bar{s} + \beta_1)(\bar{s} + \beta_2)(\bar{s} + \beta_4) = \bar{s}^3 + d_1 \bar{s}^2 + d_2 \bar{s} + d_3$$

$$(\bar{s} + \beta_1)(\bar{s} + \beta_2)(\bar{s} + \beta_3) = \bar{s}^3 + e_1 \bar{s}^2 + e_2 \bar{s} + e_3$$

Define a vector $\{Z\}$ as

$$\{Z\}^T = \left( \bar{s}^5 \{q\} \quad \bar{s}^4 \{q\} \quad \bar{s}^3 \{q\} \quad \bar{s}^2 \{q\} \quad \bar{s} \{q\} \quad \{q\} \right)$$

Rewrite equation [B.4] in the form

$$\bar{s}^6 \{q\} = -[D_6]^{-1} \left\{ [D_5] \bar{s}^5 + [D_4] \bar{s}^4 + [D_3] \bar{s}^3 + [D_2] \bar{s}^2 + [D_1] \bar{s} + [D_0] \right\} \{q\}$$

the the equation of motion can be reduced into a 6n first-order equation

$$\bar{s} \{Z\} = [H] \{Z\} \qquad [B.5]$$

$$[H] = \begin{bmatrix} H_1 & H_2 & H_3 & H_4 & H_5 & H_6 \\ I & 0 & 0 & 0 & 0 & 0 \\ 0 & I & 0 & 0 & 0 & 0 \\ 0 & 0 & I & 0 & 0 & 0 \\ 0 & 0 & 0 & I & 0 & 0 \\ 0 & 0 & 0 & 0 & I & 0 \end{bmatrix}$$

where $H_1 = -[D_6]^{-1}[D_5]$ $H_2 = -[D_6]^{-1}[D_4]$

$H_3 = -[D_6]^{-1}[D_3]$ $H_4 = -[D_6]^{-1}[D_2]$

$H_5 = -[D_6]^{-1}[D_1]$ $H_6 = -[D_6]^{-1}[D_0]$

The eigenvalues of equation [B.5], for a specific values of Mach number, dynamic pressure and freestream velocity, are the roots of the flutter characteristic equation of the system.

Since the matrix [ H ] varies with dynamic pressure, a root locus plot illustrating the variation of the eigenvalues with dynamic pressure can be constructed. And, since the modal damping is proportional to

$$\tan\left(\frac{\text{real part of the root}}{\text{imag part of the root}}\right)$$

similar plot of damping coefficient and frequency versus dynamic pressure can be made, just as in the U-g method.

# Vita

The author was born in Amsterdam, The Netherlands , on June 6, 1964. He received his elementary and secondary education in Leiden, Paris and New Delhi. Subsequently he completed his Bachelor of Arts in Graphic Design at Rotterdam School of Arts (1983) , Diploma of Engineering at Delft University (1985) and Master of Science in Civil Engineering through a sandwich program between Bandung Institute of Technology and University of Munich (1986). He worked briefly for CASA (Spain) - Indonesian Aircraft Company joint-project before entering the graduate program in Aerospace Engineering Department at Virginia Tech. After graduation, he plans to continue his arts study at Yale University .